The environmentally-regulated interplay between local three-dimensional chromatin architecture and gene expression

Rashid, F.Z.M.

Chapter 3:
Regulation of *proVWX* transcription by local chromatin re-modelling

Rashid F-Z.M., Chaurasiya, K.R., Crémazy, F.G.E., Prins, N., Herdtfelder, A., Brocken, D.J.W., and Dame, R.T. Regulation of *proVWX* transcription by local chromatin re-modelling. *In preparation for publication.*

Contributions statement:
F.M.R. and F.G.E.C. optimized the Chromosome conformation capture-based studies and prepared Hi-C libraries. F.M.R. performed the 3C-qPCR and RT-qPCR experiments. K.R.C. set-up the TIRF microscope. K.R.C., A.H., and D.J.W.B. performed the live-cell imaging experiments. K.R.C. and N.P. performed the smFRET studies. A.H. and F.M.R. engineered the strains.

Abstract

Nucleoid associated proteins maintain the architecture of the bacterial chromosome and regulate gene expression, hinting that their role as transcription factors may involve local three-dimensional chromosome re-modelling. Here, we provide the first evidence to support this hypothesis. We use ensemble RT-qPCR and 3C-qPCR, in addition to *in vivo* and *in vitro* single molecule fluorescence microscopy to show that the expression of the H-NS-regulated, osmosensitive *proVWX* operon of *Escherichia coli* involves structural re-modelling of the operon. The formation of a loop anchored between the P2 promoter of *proVWX* and the terminus of the operon represses its expression. Destabilization of the loop activates transcription. The model presented here provides clues for how H-NS and H-NS-like proteins may regulate the expression of other operons and genes within their regulons.

Introduction

Nucleoid Associated Proteins (NAPs) are architectural proteins that bind along the bacterial chromosome driving its compaction and organization. They do so by DNA bending, lateral filament formation along the DNA, or DNA bridging, the latter of which results in the formation of long- and short-range DNA loops that determine the global and local structural organization of the genome (1–10). NAP binding is sensitive to environmental changes such as fluctuations in temperature, pH, and osmolarity. Hence, NAPs organize the bacterial chromosome into a dynamic structure that is re-modelled in response to changes in the cell environment. NAPs also function as transcription factors that coordinate global gene regulation in response to environmental stimuli. Collectively, these characteristics consolidate a model proposing that NAPs regulate gene expression by reorganizing the local structure of individual operons in response to stimuli that modulate their architectural properties.

Histone-like Nucleoid Structing protein (H-NS) of *Escherichia coli* is a 137 amino acid long NAP that functions as a global regulator of gene expression (11) and as a xenogeneic silencer, repressing transcription from horizontally transferred DNA (12). It exists as a dimer in solution (13), formed via interaction between a pair of N-terminal dimerization domains (14–16). The H-NS dimer binds to AT-rich double stranded DNA by means of a C-terminal DNA binding domain (17). The interaction serves as a nucleation point for the co-operative multimerization of H-NS along the DNA to form a protein-DNA filament. Structurally, the H-NS dimers are held together via interactions between central dimer-dimer interaction domains (18, 19). The structural conformation of H-NS and, effectively, its global gene regulation is sensitive to environmental stimuli. Its osmo-sensitivity, in particular, is modulated by a K^+- and Mg^{2+}-sensitive α-helix, helix α3 (20, 21), that extends between the N-terminal dimerization domain and central dimer-dimer interaction domain (18). *In vitro* and *in silico* studies indicate that the stabilization of the helix α3 by Mg^{2+} 'opens' the H-NS dimer exposing a pair of C-terminal DNA-binding domains to promote the formation of DNA bridges (1, 20, 22, 23) – structures that impede transcription elongation *in vitro* (24). Destabilization of the helix α3 by K^+ 'closes' the H-NS molecule by folding one DNA-binding domain per dimer onto the body of the protein (20). The availability of only one DNA-binding domain per dimer favors the formation of an H-NS-DNA filament (20), a structure conducive to transcription (24). In contrast to eukaryotic systems where a causal link between chromatin architecture and transcription has been established (25), *in vivo* evidence highlighting an interplay between local

three-dimensional chromatin organization and gene expression in prokaryotes is lacking. The dual role of H-NS as a transcription factor and an architectural protein makes it an attractive target for addressing this challenge. To that end, we examined the structural regulation of the *proVWX* operon.

proVWX (*proU*) (26, 27) is an H-NS-regulated, osmo-sensitive operon activated by the rapid cytoplasmic accumulation of K^+ (counter-ion: glutamate) that ensues as a primary response to hyper-osmotic stress (28–34). The acute increase in cytoplasmic K^+ prevents cell dehydration by drawing water back from the environment (35). This, however, occurs at the expense of protein stability and function, hence, cellular processes (28). K^+ also behaves as a second messenger that activates the cell's secondary 'long-term' responses to osmotic stress, such as, the activation of the *proU* operon. *ProU* activation upregulates the expression of three structural proteins – *proV*, *proW*, and *proX* – that assemble into a transmembrane protein complex of the ATP-binding cassette (ABC) superfamily of transporters (36). The proU transporter imports osmoprotectants such as glycine-betaine, proline-betaine, and proline, among others, into the cell with high affinity (27, 29, 30, 37, 38). The osmoprotectants maintain a low osmotic potential in the cytoplasm without an adverse effect on cellular physiology, allowing K^+ to be expelled from the cell (28, 39).

The osmosensitivity of the *E. coli proU* operon is inherent in the sequences of its σ^{70}-dependent promoter (P2), and cryptic (40, 41) σ^S-dependent promoter (P1), positioned 60 and 250 bp upstream of the *proV* open reading frame (ORF), respectively (32, 42, 43) (Supplementary file 3.1; Figure 3.1). The osmosensitivity is also inherent in the *cis* regulatory elements, P1R and P2R, extending across the promoters (43). Indeed, *proU* is activated by K^+ in the absence of trans-acting factor. The addition of increasing concentrations of K-glutamate, but not of L-proline and glycine betaine, to a purified *in vitro* transcription system of RNA polymerase and nucleotides stimulates the transcription of *proU* cloned on a plasmid DNA template from both, the P1 and P2 promoters (32, 44, 45). Non-osmoregulated genes such as *bla*, *lac*, and *pepN* are repressed under identical conditions (45). The -10 sequence of P2 is a non-consensus sequence carrying three GC base pairs that interfere with dsDNA melting and open complex formation. Increasing concentrations of K-glutamate may cause microstructure changes to the promoter that either increase its accessibility to RNAP or favour the isomerisation of the RNAP-bound promoter to form the open promoter complex (45).

Owing to Rho-dependent termination of transcription from P1 under ordinary growth conditions, *proVWX* expression is primarily driven by P2 (40, 41). Expression therefrom is regulated by the negative regulatory element (NRE) — a region extending from ~300 bp upstream of the *proV* ORF to ~1100 bp into the *proV* ORF (43) (Supplementary file 3.1; Figure 3.1). As a gene spanning 1203 bp in length, truncates of *proV* double as truncates of the NRE. β-galactosidase assays performed by generating in-frame *lacZ* fusions to the 5' end of *proV* truncates indicate that the osmoresponse of *proVWX* weakens as the NRE is shortened from its downstream end (43). The NRE exerts its role by means of H-NS (Figure 3.1), and, as of yet, has been shown to confer osmosensitivity only to *proU* P2. Heterologous promoters cloned in place of *proU* P2 do not exhibit osmoresponsivity (42, 43, 46, 47). A pair of *cis* regulatory elements occurs within the broad region designated as NRE: the upstream regulatory element (URE) positioned at -229 to -47 of the P2 transcription start site (TSS), and the downstream regulatory element (DRE) that stretches across P2 from -40 to +177 (32, 42, 43, 48, 49) (Supplementary file 3.1; Figure 3.1). An intrinsic curvature in the structure of the URE (Supplementary file 3.1; Figure 3.1) contributes to the osmotic inducibility of P2. The insertion of spacer sequences between P2 and the upstream curved DNA sequence show that the two elements must be 'positioned stereospecifically', that is, the inserted spacer must comprise (multiples of) a full turn of DNA for the promoter to be fully activated at high osmolarity (50). The URE exerts its role by means of H-NS — a NAP that preferentially binds curved DNA (51–54) (Figure 3.1). The URE acts cooperatively with the DRE in an hns^{WT} strain to strengthen the repression of *proU* in low osmolarity and enhance its activation at higher osmolarity (42). Correspondingly, the DRE consists of a pair of high-affinity H-NS binding sites that function as nucleation sites for the formation of an H-NS—DNA nucleoprotein complex (48, 55) (Supplementary file 3.1; Figure 3.1). *In vitro* studies support a hypothesis according to which at low osmolarity (i.e. low intracellular K^+), the H-NS—DNA complex organises into a transcriptionally-repressive bridged conformation to silence *proVWX* (20, 24, 42, 48, 49), reminiscent of the role of H-NS at the *rrnB* P1, and *hdeAB* promoters (56, 57). Cellular influx of K^+ upon a switch to a higher osmolarity may drive a K^+-mediated reorganisation of the H-NS—DNA complex into a transcriptionally-conducive unbridged structure to relieve *proVWX* repression (20, 24, 32, 44).

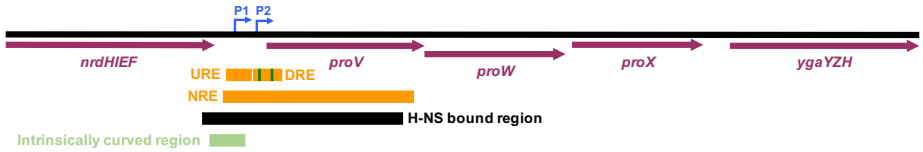

Figure 3.1: The regulatory elements of the *proVWX* operon. The *proVWX* operon comprises three ORFs: *proV*, *proW*, and *proX* (purple arrows), and is positioned between the *nrdHIEF* and *ygaGZH* operons (purple arrows) in the chromosome. The transcription of *proVWX* initates from the P1 and P2 (right angle arrows, blue) promoters recognised by σ^S and σ^{70}, respectively. The expression of the operon is regulated by the negative regulatory element (NRE, orange bar) that extends from ~300 bp upstream to ~1100 bp into the *proV* ORF. The NRE carries the upstream regulatory element (URE, orange bar) that forms part of the intrinsically curved region (light green bar), and the downstream regulatory element (DRE, orange bar). The green bars within the DRE illustrate the positions of high-affinity H-NS binding sites at which H-NS is predicted to bind and nucleate the formation of an H-NS—DNA nucleoprotein structure that spans the NRE (black bar).

In addition to H-NS, the NAPs IHF and HU also regulate *proU* (58–61). Genetic screening for mutants with decreased *proVWX* expression identified IHF and HU as positive regulators of *proVWX* expression (58, 59). IHF increases the expression of *proU* but does not affect the osmo-inducibility of the operon (58). IHF mediates its effect via a putative binding site positioned ~450 bp upstream of P2 (58), and the specific binding site of the protein in the -33 to +25 region around the P2 TSS (62). Due to limited study, it is unclear whether *proVWX* activation as a result of upstream IHF binding is affected through P1 or P2 (58, 59), however, the specific binding of IHF at P2 structurally modifies the promoter to partially relieve H-NS-mediated repression at low osmolarity (62). The precise molecular mechanism of the structural changes induced are unclear. The effect of *ihf* deletion on the expression of the *proVWX* operon was not observed in genome-wide studies (60), likely due to the modest decrease in the expression of the operon at low-osmolarity conditions in the absence of IHF (58). HU regulates expression from, and the osmoinducibilty of the proU P2 promoter (59). Δ*hupA*, Δ*hupB*, and Δ*hupAhupB* mutants show reduced proU-lac expression compared to the corresponding wild-type strain, and a reduced fold-change in expression from P2 between low and high osmolarity conditions (59). HU plays its role independently of H-NS as evidenced from Δ*hupB* Δ*hns* double mutants, where expression from P2 is realised as sum of the individual mutations rather than an epistatic output (59). The *proU*-lac expression results presented for Δ*hupA*, Δ*hupB*, and Δ*hupAhupB* in (59) are in conflict with genome-wide transcriptome data gathered in (61) which indicate that a Δ*hupA* mutation derepresses *proU* during the exponential phase of growth, Δ*hupB* derepresses the operon during transition-to-stationary phase, and Δ*hupAhupB* in stationary phase (61). However, the detection of *proU* expression at the transcriptional level from its native locus in the chromosome in (61) and

post-translationally from a plasmid-localised *proU-lacZ* gene in (59) may account for the discrepancy. The ectopic placement of a non-native *proU-lacZ* construct eliminates the effects of relevant regulatory elements and perturbs local topological states that impact *proU* expression either directly, or indirectly by affecting the binding of regulatory NAPs. StpA, an H-NS paralogue (58% sequence identity) (63, 64) that has been proposed to function as a 'molecular back-up' for H-NS (65) represses proV-lac 9-fold when expressed from multi-copy plasmids in *E. coli* Δ*hns* (66). Chromatin Immunoprecipitation (ChIP) of FLAG-tagged StpA shows that in wild-type *E. coli* and in *E. coli* Δ*hns*, StpA binds the *proVWX* regulatory region and its occupancy spans over P1 and P2 (67). StpA also binds the *proV* ORF, however, only as a hetero-oligomeric complex with H-NS (67). A ChIP signal of FLAG-tagged StpA is not observed at *proV* in *E. coli* Δ*hns* (67). Conversely, FLAG-tagged H-NS is detected at *proV* in *E. coli* Δ*stpA* (67).

The transcription of the *proVWX* operon is also regulated by genetic and chemical factors that modify the supercoiling density of the genome (43, 44, 68, 69). Mutations to DNA gyrase, and growth in media supplemented with non-lethal concentrations of novobiocin, a DNA gyrase inhibitor, reduce the levels of negative supercoiling in the cell and the expression of *proVWX* (68, 70). Mutations in *topA*, and growth in high osmolarity media increase negative supercoiling density and *proVWX* expression (68). However, extremely high levels of negative supercoiling observed in Δ*topA* mutants repress the operon (68). Furthermore, in a purified *in vitro* transcription system of RNA polymerase and nucleotides, transcription from the P2 promoter increases with increasing negative supercoiling density of the template (44). Increased negative supercoiling may favour transcription by facilitating the melting of the relatively GC-rich P2 promoter and promoting a structural reorganisation of the H-NS—NRE nucleoprotein complex (39).

Collectively, the coordinated role of an inherently osmo-sensitive promoter (32, 42, 43), supercoiling density, and architectural proteins – HU (59), IHF (58, 59, 62), StpA (66, 71), and the osmosensitive H-NS (20, 32, 42, 48, 49) – in the activation and repression of the *proU* operon from the P2 promoter implies that the regulation of *proVWX* may involve local three-dimensional reorganization of chromatin structure, analogous to eukaryotic chromatin remodelling. Here, we use 3C-qPCR and single-molecule TIRF microscopy to visualize the structural dynamics of *proVWX* in low- and high-salt conditions, and in response to a hyper-osmotic shock.

Materials and methods

Strains and plasmids

Bacterial strains used in this study were derived from *Escherichia coli* MG1655 using a one/two-step genome editing method based on the λ-red recombinase system (72) as described in (73). Chemocompetent bacteria were transformed with pKD46 (72), a temperature-sensitive plasmid encoding the λ-red proteins under an arabinose-inducible promoter. Electrocompetent pKD46+ cells were prepared from a culture grown at 30 °C in LB medium (1.0% bactotryptone (BD), 0.5% yeast extract (Alfa Aesar), 170 mM NaCl, pH 7.5) supplemented with 10 mM arabinose, for plasmid maintenance and to induce the expression of the λ-red proteins, respectively. The cells were transformed with a kanR-ccdB cassette (73) encoding kanamycin resistance and the ccdB toxin under a rhamnose-inducible promoter (72). The cassette was designed to carry ~1.5 kb extensions on either side homologous to the flanks of the genomic region to be edited. kanRccdB was amplified from plasmid pKD45 (72) and the homology regions from genomic DNA. The complete construct was assembled using overlap extension PCR (oePCR). Recombinants were selected for on LB agar (1.0% bactotryptone (BD), 0.5% yeast extract (Alfa Aesar), 170 mM NaCl, 1.5% bacteriological agar (Oxoid), pH 7.5) supplemented with 40 µg/mL kanamycin at 37 °C and verified using colony PCR and Sanger sequencing (BaseClear B.V.). The mutant allele construct with ~1.5kb homology regions was assembled into a plasmid using Gibson assembly (74). The allele was amplified and used to replace the genomic kanRccdB cassette via the λ-red recombinase system. Recombinants were selected for on M9 agar plates (42 mM Na_2HPO_4, 22 mM KH_2PO_4, 19 mM NH_4Cl, 8.5 mM NaCl, 2 mM $MgSO_4$, 0.1 mM $CaCl_2$, 1.5% bacteriological agar (Oxoid)) supplemented with 1% rhamnose and verified with colony PCR and Sanger sequencing (BaseClear B.V.). The lac::CamR mutation was performed in a single step using a chloramphenicol resistance cassette carrying ends homologous to the left and right flanks of the *lac* operon. Selection was carried out on LB agar with 12.5 µg/mL chloramphenicol. All bacterial strains and intermediates were stored at -80 °C as glycerol stocks. Strains and plasmids used in this study are listed in Tables 3.1 and 3.2. Detailed protocols are available upon request.

Table 3.1: List of strains

Strain ID	Description	Reference
MG1655	*Escherichia coli* K-12	
NT331	MG1655 ΔendA	This chapter
NT453	MG1655 ΔendA ProU_terminus::lacO pProU::tetO-pProU	This chapter
NT455	MG1655 ΔendA ProU_terminus::lacO pProU::tetO-pProU pRD183	This chapter
NT606	MG1655 ΔendA; pKD46 (AmpR)	This chapter

NT607	MG1655 ΔendA lac::CamR	This chapter
NT617	MG1655 ΔendA lac::CamR; pKD46 (AmpR)	This chapter
NT618	MG1655 ΔendA lac::CamR ProU::kanRccdB	This chapter
NT620	MG1655 ΔendA lac::CamR ProU::tetO-proU-lacO	This chapter
NT623	MG1655 ΔendA lac::CamR ProU::kanRccdB; pRD418 (SpnR)	This chapter
NT624	MG1655 ΔendA lac::CamR ProU::kanRccdB; pRD419 (SpnR)	This chapter
NT625	MG1655 ΔendA lac::CamR ProU::tetO-pProU_GC-proU-lacO	This chapter
NT626	MG1655 ΔendA lac::CamR ProU::kanRccdB; pRD418 (SpnR) pRD310 (AmpR)	This chapter
NT627	MG1655 ΔendA lac::CamR ProU::kanRccdB; pRD418 (SpnR) pRD373 (AmpR)	This chapter
NT629	MG1655 ΔendA lac::CamR ProU::kanRccdB; pRD419 (SpnR) pRD310 (AmpR)	This chapter
NT630	MG1655 ΔendA lac::CamR ProU::kanRccdB; pRD419 (SpnR) pRD373 (AmpR)	This chapter
NT632	MG1655 ΔendA rnc::kanRccdB	This chapter
NT633	MG1655 ΔendA stpA::kanRccdB	This chapter
NT638	MG1655 ΔendA lac::CamR ProU_terminus::kanRccdB	This chapter
NT639	MG1655 ΔendA lac::CamR ProU_terminus::kanRccdB; pKD46 (AmpR)	This chapter
NT640	MG1655 ΔendA lac::CamR ProU_terminus::lacO	This chapter
NT641	MG1655 ΔendA lac::CamR ProU_terminus::lacO; pKD46 (AmpR)	This chapter
NT642	MG1655 ΔendA pProU::kanRccdB; pKD46 (AmpR)	This chapter
NT643	MG1655 ΔendA lac::CamR ProU_terminus::lacO pProU::kanRccdB; pKD46 (AmpR)	This chapter
NT644	MG1655 ΔendA pProU::pProU_GC	This chapter
NT645	MG1655 ΔendA lac::CamR ProU_terminus::lacO pProU::tetO-pProU	This chapter
NT646	MG1655 ΔendA lac::CamR ProU_terminus::lacO pProU::tetO-pProU_GC	This chapter
NT647	MG1655 ΔendA lac::CamR ProU_terminus::lacO pProU::tetO-pProU; pRD310 (AmpR)	This chapter
NT648	MG1655 ΔendA lac::CamR ProU_terminus::lacO pProU::tetO-pProU; pRD373 (AmpR)	This chapter
NT658	MG1655 ΔendA; pRD310 (AmpR)	This chapter
NT659	MG1655 ΔendA; pRD373 (AmpR)	This chapter
NT660	MG1655 ΔendA pProU::pProU_GC; pRD310 (AmpR)	This chapter
NT661	MG1655 ΔendA pProU::pProU_GC; pRD373 (AmpR)	This chapter
NT662	MG1655 ΔendA lac::CamR ProU_terminus::lacO pProU::tetO-pProU_GC; pRD310 (AmpR)	This chapter
NT663	MG1655 ΔendA lac::CamR ProU_terminus::lacO pProU::tetO-pProU_GC; pRD373 (AmpR)	This chapter

Table 3.2: List of plasmids

Plasmid ID/ Strain ID	Backbone	Insert	Resistance	Storage strain	Reference
pKD45/ XT198	pKD45	kanR P_{rhaB}-ccdB	Kanamycin	HCB1666	(72)
pKD46/ XT146	pKD46	araC P_{araB}-λ Red	Ampicillin	MG1655 ΔthyA	(72)
pTargetF/ XT205	pTarget	sgRNA (cadA)	Streptomycin, Spectinomycin	DH5α	Addgene #62226 (75)
pRD178/ NT279	pMK	6TetO hybrid array (tetO)	Kanamycin	KA797	This chapter

pRD179/ NT280	pMK	6LacO hybrid array (lacO)	Kanamycin	KA797	This chapter
pRD183/ NT304	pBAD24	LacI-mCherry-tetR-YFP	Ampicillin	DH5α	This chapter
pRD258/ NT397	pTarget	ProU_terminus-lacO	Streptomycin, Spectinomycin	DH5α	This chapter
pRD259/ NT398	pTarget	tetO-pProU	Streptomycin, Spectinomycin	DH5α	This chapter
pRD310/ NT477	pBAD24	J23101_promoter-LacI_mCherry-TetR_eYFP-rrnB_T1_terminator	Ampicillin	DH5α	This chapter
pRD359/ NT547	pTarget	pProU_GC	Streptomycin, Spectinomycin	DH5α	This chapter
pRD373/ NT574	pBAD24	J23101_promoter-LacI_mCherry-λtL3_terminator-J23101_promoter-TetR_eYFP-rrnB_T1_terminator	Ampicillin	DH5α	This chapter
pRD391/ NT591	pTarget	lac::CamR	Streptomycin, Spectinomycin, Chloramphenicol	DH5α	This chapter
pRD417/ XT235	pHA2	eGFP	Kanamycin, Chloramphenicol	DH5α	This chapter
pRD418/ NT621	pHA2	tetO-ProU-lacO	Streptomycin, Spectinomycin	KA797	This chapter
pRD419/ NT622	pHA2	tetO-pProU_GC-ProU-lacO	Streptomycin, Spectinomycin	KA797	This chapter

Media and growth conditions

For low-salt and hyper-osmotic shock conditions, a single bacterial colony from a freshly streaked plate was grown overnight at 37 ºC in low-salt LB medium (LS-LB: 1.0% bactotryptone (BD), 0.5% yeast extract (Alfa Aesar), 80 mM NaCl, pH 7.5) or low-salt M9 medium (LS-M9: 42 mM Na_2HPO_4, 22 mM KH_2PO_4, 19 mM NH_4Cl, 2.0 mM $MgSO_4$, 0.1 mM $CaCl_2$, 80 mM NaCl, 1X trace elements, 1% Bacto™ casamino acids (BD), 10 µg/mL Thiamine (Sigma-Aldrich), 0.4% glycerol (PanReac Applichem)). The overnight culture was used to inoculate fresh low-salt LB or M9 medium to a starting OD_{600} of 0.05 for up to four biological replicates and grown at 37 ºC to an OD_{600} of ~1.0. The culture was split into two aliquots. For hyper-osmotic shock, 5.0 M NaCl was added to one of the aliquots at a ratio of 46 µL per mL of culture. An equivalent volume of milliQ water was added to the second aliquot for the low salt condition. The cultures were grown for 10 minutes at 37 ºC, and then immediately harvested for RNA isolation, cell fixation for 3C-based experiments, and microscopy. For high-salt studies, a single bacterial colony was grown overnight in high-salt LB medium (LS-LB: 1.0% bactotryptone

(BD), 0.5% yeast extract (Alfa Aesar), 300 mM NaCl, pH 7.5) or high-salt M9 medium (HS-M9: 42 mM Na_2HPO_4, 22 mM KH_2PO_4, 19 mM NH_4Cl, 2.0 mM $MgSO_4$, 0.1 mM $CaCl_2$, 300 mM NaCl, 1X trace elements, 1% Bacto™ casamino acids (BD), 10 µg/mL Thiamine (Sigma-Aldrich), 0.4% glycerol (PanReac Applichem)). The overnight culture was used to inoculate fresh high-salt LB or M9 medium to an OD_{600} of 0.05 for up to four biological replicates. The cells were cultured at 37 °C to an OD_{600} of ~1.0, and for an additional 10 minutes. The cells were immediately harvested for RNA isolation, cell fixation, and microscopy.

Trace elements were prepared as a 100X stock solution of the following composition per 100 mL: 0.1 g $FeSO_4 \cdot 7H_2O$, 0.6 g $CaCl_2 \cdot 2H_2O$, 0.12 g $MnCl_2 \cdot 4H_2O$, 0.08 g $CoCl_2 \cdot 6H_2O$, 0.07 g $ZnSO_4 \cdot 7H_2O$, 0.03 g $CuCl_2 \cdot 2H_2O$, 2 mg H_3BO_3, and 0.5 g EDTA·Na_2.

RNA isolation and handling

Bacterial cells in 1 mL of culture (Media and growth conditions, Materials and methods) were collected by centrifugation at 13,000 xg for 2 minutes. The supernatant was removed and the pellet was resuspended in 200 µL of Max Bacterial Enhancement Reagent (TRIzol® Max™ Bacterial RNA Isolation Kit, Ambion®, life Technologies™) pre-heated to 95 °C. The lysate was incubated at 95 °C for 5 minutes. The preparation was treated with 1 mL of TRIzol® reagent (Ambion®, life Technologies™) and incubated at room temperature for 5 minutes. RNA isolation was paused at this step to accommodate cell fixation for 3C and Hi-C library preparation by flash-freezing the TRIzol®-lysate mix in liquid nitrogen and storing at -80 °C for up to 2 weeks. The TRIzol®-lysate mix was thawed at room temperature and RNA isolation was continued using the TRIzol® Max™ Bacterial RNA Isolation Kit (Ambion®, life Technologies™) according to the manufacturer's instructions. The concentration and purity (A_{260}/A_{280}) of RNA was measured with a NanoDrop™ 2000 spectrophotometer (Thermo Scientific™), and accordingly, RNA samples were diluted to a final concentration of 20 ng/µL with RNase-free water (Gibco®, life Technologies™). DNA contamination in the RNA samples was checked with RNase A (Qiagen) treatment and agarose gel electrophoresis. 50 µL of the RNA samples were transferred into wells of a 96-well RNase/DNase-free plate in triplicate to facilitate multi-channel pipetting for RT-qPCR experiments. RNA samples in the multi-well plate were stored at 4 °C and placed on ice during reaction set-up to avoid freeze-thaw cycles. Stock RNA samples were stored at -20 °C.

RT-qPCR

Primer design

Primers for RT-qPCR experiments were designed using the *Escherichia coli* K-12 MG1655 sequence (Accession number: NC_000913.3). *In silico* specificity screening was performed on SnapGene® Viewer 5.2. RT-qPCR primers were ordered as dried pellets from Sigma-Aldrich. The oligonucleotides were dissolved in 1X TE pH 8.0 to a final concentration of 100 µM and stored at 4 °C. The list of primers used for the RT-qPCR assay and corresponding amplicon details are provided in Supplementary file 3.2. Primer annealing sites and amplicon positions in the *proVWX* operon are provided in Supplementary files 3.1 and 3.2. The specificity of primer pairs was experimentally determined with Sanger sequencing (BaseClear B.V.) of the amplified PCR product, and melting curves.

Reaction set-up

RT-qPCR experiments were performed with the Luna® Universal One-Step RT-qPCR Kit (NEB, #E3005E) with a final reaction volume of 10 µL per well. The reaction composition is provided in Table 3.3. The reactions were set-up manually in Hard-Shell® 96-well PCR plates (Bio-Rad, #HSP9635) and run on a C1000 Touch™ thermal cycler heating block (Bio-Rad) with a CFX96™ Real-time system (Bio-Rad). The thermocycling parameters are provided in Table 3.4. NT331 genomic DNA (Supplementary methods) serially diluted in triplicate to 10X, 100X, 1000X, and 10000X dilution factors was used for the standard samples. Standard samples, test samples, and No Template Controls were processed in the same manner.

Table 3.3: RT-qPCR reaction composition per well. Modified from the manufacturer's protocol provided with the Luna® Universal One-Step RT-qPCR Kit.

Component	Volume in a 10.0 µL reaction	Final concentration
‡2X Luna Universal One-Step Reaction Mix (NEB)	5.0 µL	1X
‡20X Luna WarmStart® RT Enzyme Mix (NEB)	0.5 µL	1X
‡100 µM forward primer (Supplementary files 3.1 and 3.2)	0.04 µL	0.4 µM
‡100 µM reverse primer (Supplementary files 3.1 and 3.2)	0.04 µL	0.4 µM
‡Nuclease free water (Gibco®, life Technologies™)	3.92 µL	N/A
~20 ng/µL RNA sample	0.5 µL	~10 ng

‡ These components were added to each reaction as a master mix.

Table 3.4: RT-qPCR thermal cycling parameters. As per the manufacturer's instructions provided with the Luna® Universal One-Step RT-qPCR Kit.

No.	Step	Temperature	Duration (mm:ss)	Cycles
1	Reverse transcription	55 °C	10:00	1

2	Initial denaturation	95 °C	01:00	1
3	Denaturation	95 °C	00:10	45
4	Annealing/extension	60 °C	00:30	
5	Plate read (SYBR/FAM channel)	N/A	N/A	
6	Melt	60 °C	0:31	1
7	Ramp	60 °C	0:01	70
		+ 0.5 °C/cycle	+ 0:01/0.5 °C	
8	Plate read (SYBR/FAM channel)	N/A	N/A	

Cell fixation

6.0 mL of the bacterial culture in M9 medium (See media and growth conditions) was collected by centrifugation at 3000 xg for 5 minutes at 4 °C. The supernatant was discarded and the pellet was resuspended in 2 mL of LS-M9 medium for the low salt cultures or 2 mL of HS-M9 medium for the high salt and salt shock cultures. The cell suspension was treated with 8 mL of ice-cold methanol and incubated at 4 °C for 10 minutes. The cells were collected by centrifugation at 3000 xg for 5 minutes at 4 °C and washed with 20 mL of LS/HS-M9 medium. The pellet of washed, methanol-treated cells was resuspended in 3% formaldehyde in LS/HS-M9 medium. The reaction was incubated at 4 °C for 1 hour and subsequently quenched with a final concentration of 0.375 M glycine for 15 minutes at 4 °C. The fixed cells were collected by centrifugation and washed twice with 1X TE. The cell suspension was split into three aliquots and pelleted at 10000 xg at room temperature for 2 minutes. The supernatant was removed and the cell pellet was flash-frozen in liquid nitrogen for storage at -80 °C until use (up to 1 month).

Bacterial cultures grown in LB were fixed in the same manner, except that all wash steps and 3% formaldehyde preparation were performed with 1X LS-PBS (2.7 mM KCl, 10 mM Na_2HPO_4, 1.8 mM KH_2PO_4), 1X HS-PBS (280 mM NaCl, 2.7 mM KCl, 10 mM mM Na_2HPO_4, 1.8 mM KH_2PO_4), or 1X PBS (137 mM NaCl, 2.7 mM KCl, 10 mM mM Na_2HPO_4, 1.8 mM KH_2PO_4) as required.

Hi-C and 3C library preparation

Hi-C libraries were prepared as described in (76). For 3C libraries, the Hi-C library preparation section in (76) was modified by eliminating 'Fill-in with biotin-labelled nucleotides' and followed up to step 40. NlaIII (NEB) was used as the restriction enzyme.

3C library handling

The concentration of the 3C libraries was measured with the Qubit™ dsDNA HS Assay Kit (Themo Fisher Scientific™, #Q32854) using the Qubit 2.0 fluorometer

(ThermoFisher Scientific™). The A_{260}/A_{280} ratio was not determined since the presence of glycogen in the library preparation interfered with absorbance at these wavelengths. The 3C libraries were diluted to a final concentration of 2 ng/µL with nuclease-free water (Invitrogen™) and transferred into wells of a 96-well RNase/DNase-free plate in triplicate to facilitate multi-channel pipetting for 3C-qPCR set-up. 3C libraries in the multi-well plate were stored at 4 ºC and placed on ice during reaction set-up to avoid freeze-thaw cycles. Library stocks were stored at -20 ºC.

3C-qPCR

The 3C-qPCR protocol was designed according to (77).

Primer and TaqMan probe (hydrolysis probe) design

Primers and TaqMan probes for 3C-qPCR experiments were designed using the Escherichia coli K-12 MG1655 sequence (Accession number: NC_000913.3) on SnapGene® Viewer 5.2. SnapGene® Viewer was also used for *in silico* specificity screening. For the fragments of interest for 3C-qPCR test reactions and cross-linking controls, primers and TaqMan probes were designed on opposite DNA strands within 100 bp of the downstream NlaIII site, with TaqMan probes positioned closer to the restriction site than the primers. All primers were designed to anneal to the genomic DNA with the same directionality so as to ensure that the signal observed during 3C-qPCR assays arises only as a result of re-ligation between the pair of fragments being tested and not due to incomplete restriction digestion. Furthermore, the hybridisation of the TaqMan probe to the non-primed strand of a fragment ensures that the hydrolysis of the probe, and hence, the detection of a fluorescence signal in qPCR only occurs if amplification crosses the ligation junction being tested.

For 3C-qPCR loading controls, primer pairs amplifying a ~100 bp region lacking an NlaIII digestion site were designed. For these amplicons, the TaqMan probe with the lowest predicted melting temperature for its secondary structures, as determined using OligoAnalyzer (IDT), was selected.

Double-quenched TaqMan probes (HPLC purified) with a 5' 6-FAM fluorophore, 3' Iowa Black™ Fluorescence Quencher, and an internal ZEN quencher positioned 9 bases from the fluorophore were ordered as dried pellets from IDT. Primers (desalted, dry) were ordered from IDT or Sigma-Aldrich. The oligonucleotides were dissolved in 1X TE pH 8.0 to a final concentration of 100 µM and stored at

4 °C. The lists of primers and probes used for 3C-qPCR, their positions within the *proU* operon and their annealing sites on the chromosome are provided in Supplementary files 3.1 and 3.3.

Control library preparation

Three sets of control libraries were prepared for 3C-qPCR: digested and randomly re-ligated NT331 genomic DNA, digested and randomly re-ligated NT644 gDNA, and a synthetic control template where chimeric fragments of interest were separately prepared by PCR and pooled in equimolar ratios. The control libraries were serially diluted to prepare the standard samples for 3C-qPCR.

Reaction set-up

3C-qPCR (77) was performed using the PrimeTime™ Gene Expression Master Mix Kit (Integrated DNA Technologies, #10557710) using 10 ng of the 3C libraries, corresponding to ~2 x 10^6 genome equivalents, as the template. A detailed reaction composition is provided in Table 3.5. Experiments were set-up manually in Hard-Shell® 96-well PCR plates (Bio-Rad, #HSP9635) and run on a C1000 Touch™ thermal cycler heating block (Bio-Rad) with a CFX96™ Real-time system (Bio-Rad) using the program outlined in Table 3.6. Standard, Test, and No Template Control samples were processed in the same manner.

Table 3.5: 3C-qPCR reaction composition per well. Modified from the manufacturer's protocol provided with the PrimeTime® Gene Expression Master Mix.

Component	Volume per reaction	Final concentration
‡2X PrimeTime® Gene Expression Master Mix (IDT)	5.0 µL	1X
‡100 µM TaqMan probe (IDT)	0.015 µL	0.15 µM
‡100 µM Constant primer (Supplementary file 3.3)	0.05 µL	0.5 µM
‡100 µM Test primer (Supplementary file 3.3)	0.05 µL	0.5 µM
~2 ng/µL 3C library	5.0 µL	~10 ng

‡ These components were added to each reaction as a master mix.

Table 3.6: 3C-qPCR thermal cycling parameters. As per the manufacturer's instructions provided with the PrimeTime® Gene Expression Master Mix.

No.	Step	Temperature	Duration (mm:ss)	Cycles
1	Polymerase activation	95 °C	03:00	1
3	Denaturation	95 °C	00:15	45
4	Annealing/extension	60 °C	01:00	
5	Plate read (SYBR/FAM channel)	N/A	N/A	

qPCR Data Analysis

RT- and 3C-qPCR data were processed using the Bio-Rad CFX Manager 3.1 program (Bio-Rad) and analysed with Microsoft Excel. All the raw data files, and

the exported .csv files are available in Supplementary folders 3.1-3.4. For all RT-qPCR experiments, the cycle of quantification (Cq) was determined using the Single Threshold option available on Bio-Rad CFX Manager 3.1. For 3C-qPCR, Cq was determined using the Regression function. Reactions with unreliable Cq values as a result of pipetting errors owing to the manual set-up of the experiment, or evaporation from improperly sealed wells, were eliminated from analysis. For the intercalator-based RT-qPCR experiment, melt curves were used to check the specificity of amplification, and hence, the validity of the experiment. Eliminated reactions and the justifications for each are provided in the Supplementary files 3.4-3.8.

The Cq values of the standard samples were used to plot a standard curve of Cq against the logarithm of the starting quantity of the template. Standard samples with pipetting errors were eliminated from the plot. To verify that quantification was performed in the linear dynamic range, it was ensured that the standard curve was linear (R^2 >0.95) and that the range of Cq values spanned by the standard curve encompassed the Cq values of the test reactions as much as possible. The slope, y-intercept, PCR efficiency, and R^2 value were extracted from the standard plot.

The Cq values of the technical replicates for each biological sample were used to determine the average Cq value (Cq_{avg}) and standard deviation of Cq (σCq) for each amplicon. Cq_{avg} was used to determine the relative expression level of the amplicons in RT-qPCR experiments and the relative interaction frequency in 3C-qPCR. σCq was used to determine the negative and positive errors for the biological samples. The calculations were done using the formula: 10^((Cq-Intercept)/Slope). This processing was applied for all Test amplicons and Internal control candidates (Supplementary files 3.4-3.8).

The relative expression levels and relative interaction frequencies of the Test amplicons were normalised to an Internal control amplicon to allow comparisons to be drawn between biological samples. This was done by assigning an arbitrary value of 100 to the relative expression level or interaction frequency of the selected Internal control. The values corresponding to the Test amplicons for all biological samples were re-calculated accordingly. Since all amplicons were quantified from standard curves plotted from the same standard samples, inter-assay comparisons were made possible.

Live cell FROS imaging

Slide preparation

800 µL of molten 3% (w/v) low-melt agarose dissolved in HS- or LS-M9 medium, as necessary, was applied on the surface of a microscope slide thoroughly cleaned with 70% ethanol. A pair of spacer slides were placed over the top and bottom edges of the microscope slide and a clean cover-slip was placed on top to mould the molten agarose into an agarose pad with a flattened surface. The spacer slides and the coverslips were removed after the agarose solidified and 5.0 µL of an *E. coli* culture concentrated to ~1/50th of its culture volume was pipetted onto the centre of the pad. The agarose pad was covered with a clean coverslip and sealed with nail polish.

Imaging

The cells were positioned at the centre of the imaging region of the TIRF microscopy set-up described in (78) using bright-field illumination, and brought into optimal focus for fluorescence imaging using the bottom half of the cell to focus the objective. The intensities of the excitation lasers were modulated to ~200 W/cm^2 with the shutters closed to prevent initial photobleaching. After opening of the shutters a continuous series of images was recorded until the fluorescent molecules bleached. ImageJ was used to identify the position of the centroids of fluorescent spots in the image series and link the positions to individual trajectories. The distance between the pair of FROS labels was determined every 4.2 seconds (frame rate: 14.3 frames/minute) for the recorded cells.

In vitro single molecule FRET

The 250 bp AT-rich construct and the set of 7 fragments for *proU* bridging experiments were obtained with PCR. A 685 bp (32% GC) molecule described in (79), and NT331 genomic DNA were used as the templates, respectively. The primers were fluorescently labelled with Cy3 or Cy5 and one primer of each pair was functionalized at the 5' end with BiotinTEG (Sigma-Aldrich). The amplified constructs were purified using the GFX^{TM} PCR DNA and Gel Band purification kit (GE Healthcare) and eluted in 1X TE buffer (10 mM Tris-HCl pH 8.0, 1 mM EDTA). The substrates for IHF-mediated DNA bending studies were prepared by annealing a pair of complementary single stranded oligonucleotides in annealing buffer (10 mM Tris-HCl pH 8.0, 50 mM NaCl, 1 mM EDTA). For each pair one oligonucleotide was labelled with 5' Cy5 and the other with 5' Cy3 and 3' BiotinTEG. Primer

sequences are provided in Table S3.1. DNA substrates were serially diluted in annealing buffer to 25 pM for smFRET. SmFRET was performed using total internal reflection fluorescence (TIRF) microscopy using the set-up described in (78).

The fluorescent bead reference was used to calibrate the microscopy set-up prior to each experiment. The beads were excited with the 532 nm laser at 1 mW and 0 EM gain. The test sample was excited with the 532 nm laser at 20-50 mW and 700 EM gain. Movies of ~4000 frames (33 ms/frame) were recorded. A custom script written in IDL (78) was used to align the donor and acceptor images and to extract fluorescence intensities for single molecules of the test sample. A MatLab script (78) was used to validate the single-molecule traces from single-step photobleaching of the Cy3/Cy5 dyes, perform base-line corrections, and manually analyze the single-molecule traces. FRET efficiencies of selected traces were plotted in histograms using Igor Pro 7 (WaveMetrics, Inc., Lake Oswego, OR, USA), and fitted by single peak or multipeak fitting with gaussian distributions to determine the distribution of FRET states in the population.

Results

Degradation of *Escherichia coli* chromatin during 3C-based library preparation is overcome by the deletion of *endA*.

The *Escherichia coli* K-12 MG1655 strain closely resembles the genetic make-up of archetype *E. coli* and is used as a reference for genome-wide studies of NAP-binding profiles and transcription. The strain is, therefore, the optimal choice to study the interplay between three-dimensional chromatin organisation, NAP distribution, and gene expression. However, chromatin extracted from MG1655 underwent considerable degradation during the initial steps of 3-C and Hi-C library preparation. The degradation was not observed during the lysis and solubilisation steps (76, 80) that were carried out in a buffer with 1.0 mM EDTA, but occurred extensively once the cell lysate was diluted in a restriction digestion mix with a final EDTA concentration of 0.1 mM (Figure 3.2A). The dependence of chromatin degradation on the concentration of EDTA, and hence, the availability of divalent ions implied that the degradation was enzymatic.

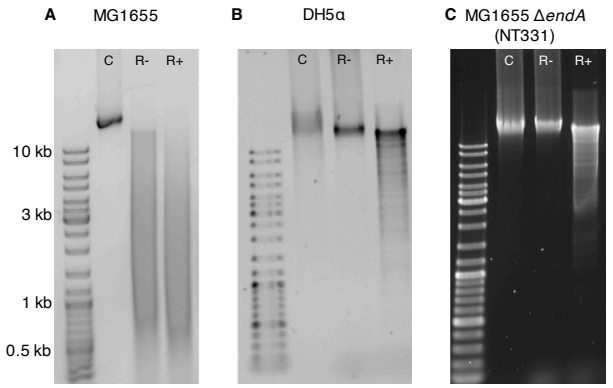

Figure 3.2: Degradation of *Escherichia coli* chromatin during 3C-based library preparation is overcome by *endA* deletion. Lane C: Chromatin preparation in 1X TE (EDTA concentration: 1.0 mM); **Lane R-:** Chromatin preparation after a 3-hour incubation in 1X restriction digestion buffer (EDTA concentration: 0.1 mM); **Lane R+:** Chromatin preparation after a 3-hour treatment with 0.4 U/µL of BglII in 1X restriction digestion buffer (EDTA concentration: 0.1 mM). **MG1655 (panel A)** chromatin undergoes extensive degradation in a restriction digestion buffer with a final EDTA concentration of 0.1 mM. The degradation is observed as a smear in lanes R- and R+ of panel A. Similar degradation is not observed in *endA* knock-out strains, **DH5α (panel B)** and **NT331 (panel C)**, where extracted chromatin (lane C) still runs as a heavy >10 kb band after a 3-hour incubation in a buffer with 0.1 mM EDTA (lane R-). Fixed chromatin extracted from the *endA*⁻ strains (panels B and C) can be digested by BglII (shown), PsuI (not shown), and NlaIII (not shown).

Endonuclease-I, a DNA-specific nuclease localised in the periplasm (81), digests dsDNA in a sequence independent manner and is responsible for the low quality of plasmid DNA preparations from *endA*$^+$ *E. coli* strains (82, 83). To investigate whether the enzyme also contributes to the degradation of chromatin in lysates of

formaldehyde-treated cells, the stability of fixed chromatin extracted from DH5α, an *endA*$^-$ strain of *E. coli* (83) during the initial steps of chromosome conformation capture was determined. Agarose gel electrophoresis showed that DH5α chromatin preparations do not degrade in the restriction digestion buffer with 0.1 mM EDTA (Figure 3.2B). Attempts to thermally denature endonuclease-I and overcome chromatin degradation were not pursued extensively since the conditions that reliably decreased degradation also promote reverse cross-linking of the chromatin and thereby interfere with proximity ligation in later steps of 3C-based protocols (Figure S3.1). Therefore, MG1655 Δ*endA* (henceforth referred to as NT331) was generated using the λ-red recombinase mediated gene replacement strategy (see: Materials and methods, Strains and plasmids) (72, 73). Chromatin preparations from fixed NT331 do not degrade when incubated in a buffer with a low concentration of EDTA (Figure 3.2C). Thus, all 3-C based experiments were carried out in a Δ*endA* background. It is noteworthy that using higher concentrations of formaldehyde for fixation, for instance, 7%, reduces chromatin degradation. *endA* deletion eliminates the requirement of using such concentrations and provides a wider window to optimize fixation conditions.

Proximity ligation with the insoluble fraction of digested, cross-linked chromatin, and methanol permeabilization of *Escherichia coli* prior to formaldehyde fixation improves the signal-to-noise ratio in chromosome contact maps.

Hi-C libraries of NT331 fixed with 3% formaldehyde have a low signal-to-noise ratio (Figure 3.3A), indicating inefficient formaldehyde-mediated cross-linking. Taking an earlier report of 3C-based studies in *E. coli* (84) into account, we raised the concentration of formaldehyde for fixation from 3% to 7%. However, the change did not contribute to a significant improvement in chromosome contact maps (Figure S3.2).

A low signal-to-noise ratio in chromosome contact maps may arise as a result of ligation between freely moving, non-crosslinked DNA molecules (85). This effect can be overcome by fractionating the digested, cross-linked chromatin into its soluble supernatant, and relatively insoluble pellet fractions by centrifugation (85, 86). The resulting enrichment of cross-linked DNA-protein complexes in the pellet and freely moving DNA molecules in the supernatant allows contact maps with a high signal-to-noise ratio to be generated when proximity ligation is carried out with only the pellet fraction (85, 86). In agreement with previous observations in E14.5 mouse embryos (86), *Saccharomyces cerevisiae* (85), and *S. pombe* (85),

incorporating fractionation and using only the pellet fraction for proximity ligation improved the signal-to-noise ratio of the *E. coli* NT331 contact map (Figure 3.3B). Fractionation was also incorporated in 3C-based studies of *Bacillus subtilis* (87).

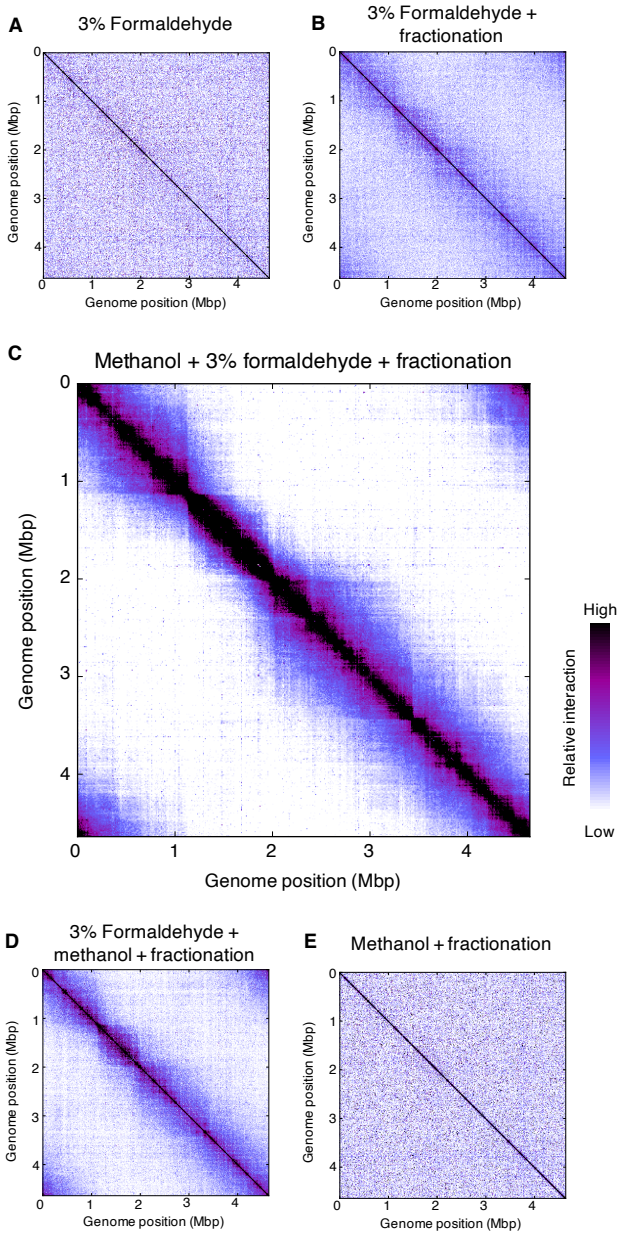

Figure 3.3: Proximity ligation with the insoluble fraction of digested, cross-linked chromatin, and methanol permeabilization of *Escherichia coli* prior to formaldehyde fixation improves the signal-to-noise ratio in chromosome contact maps. A: Hi-C libraries prepared from cells fixed with

3% formaldehyde have a low signal-to-noise ratio. **B, C:** The signal-to-noise ratio is improved by proximity ligation with the insoluble fraction of digested, cross-linked chromatin and methanol permeabilization of *E. coli* cells prior to formaldehyde fixation**. D:** Only marginal improvements in the signal-to-noise ratio are observed if methanol treatment is performed after formaldehyde fixation. **E:** *E. coli* cells permeabilised with methanol but not fixed with formaldehyde cannot be used to map chromosome structure. **Organism:** *Escherichia coli* MG1655 Δ*endA* (NT331); **3C-based study:** Hi-C; **Resolution:** 10 kb; **Growth conditions:** LB medium, 37 °C, exponential phase; **Fixation conditions: Panels A and B:** 3% formaldehyde, 1 hour, **Panel C:** 80% cold methanol for 10 minutes followed by 3% formaldehyde for 1 hour, **Panel D:** 3% formaldehyde for 1 hour followed by 80% cold methanol for 10 minutes, **Panel E:** 80% cold methanol for 10 minutes; **Restriction enzyme:** PsuI (ThermoFisher Scientific); **Fractionation: Panel A:** No, **Panels B-E:** Yes.

Formaldehyde is a commonly-used fixative in histology and (immuno–)histochemical studies where it is used either alone, or in combination with methanol (88, 89). Methanol dissolves lipids from cell membranes and coagulates proteins, thus, simultaneously permeabilizing and fixing histological preparations (89, 90). We extrapolated this to *E. coli*, and permeabilized the cells with 80% methanol prior to formaldehyde fixation. This treatment led to a significant improvement in the signal-to-noise ratio in chromosome contact maps (Figure 3.3C). Only a weak improvement was observed when methanol permeabilization followed formaldehyde fixation (Figure 3.3D). Methanol treatment alone could not be used to study chromosome conformation (Figure 3.3E).

Escherichia coli cells show global differences in the chromosome contact profiles during growth at different osmolarity conditions.

The binding of NAPs to DNA is sensitive to environmental conditions such as pH, temperature, and osmolarity. Consequently, changes to the ambient growth conditions of bacteria are reflected in an altered NAP binding profile of the chromosome, and hence, in the three-dimensional chromosome organization. We first examined the global differences in the chromosome contact profiles of NT331 during growth in a low-salt (0.08 M NaCl) medium, following a hyperosmotic shock (0.08 M -> 0.3 M NaCl), and in a high-salt (0.3 M NaCl) medium (Figures 3.4 and 3.5).

The NT331 chromosome contact maps exhibit a main diagonal of high interaction frequency that accounts for the physical proximity of chromosome regions close to each other in the primary genome sequence (black arrows, Figure 3.4). For NT331 cells growing in a low-salt medium (NT331 LS) high frequency interactions (in black) occur over distances of up to ~270 kb across the chromosome. The high frequency interactions occur over longer distances in the Ter macrodomain compared to the rest of the chromosome. This can be deduced from the width of the region of high interaction frequency around the main diagonal. This region is

thicker at the Ter macrodomain than the non-Ter regions of the chromosome. The width of this region is also indicative of local and global chromosome compaction. In NT331 LS, the chromosome is organized more compactly in the Ter macrodomain than it is in the non-Ter regions. Long-range, lower frequency interactions, observed in varying shades of purple, occur largely over distances of up to 1.1 Mb in non-Ter regions and ~670 kb in the Ter macrodomain (Figure 3.5A, left panel). Upon a hyperosmotic shock (NT331 SS), and in high salt media (NT331 HS), high frequency interactions still occur at distances of up to ~270-300 kb, however, the thickness of the diagonal indicates global decompaction of the chromosome. The changes are particularly evident in the non-structured right (NSR), non-structured left (NSL), and Ori macrodomains upon a hyperosmotic shock, and throughout the chromosome during growth in high-salt. For both conditions, long range, lower frequency interactions occur at distances of up to 1.3-1.6 Mb in non-Ter regions. In the Ter macrodomain, these interactions do not extend far beyond ~750 kb (Figures 3.5B and 3.5C, left panels).

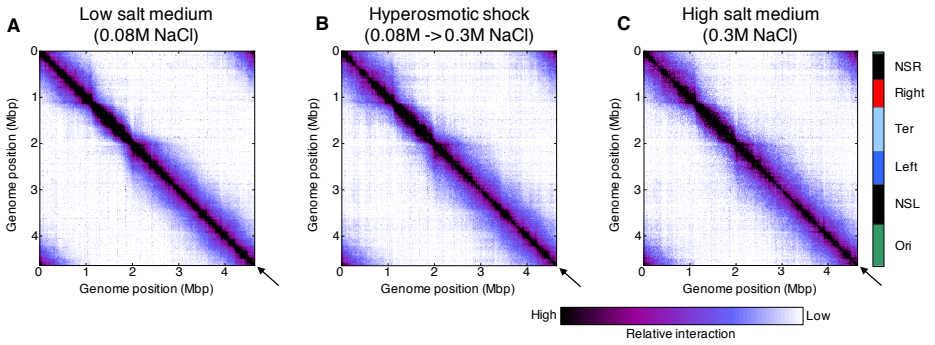

Figure 3.4: *Escherichia coli* cells show global differences in chromosome contact profiles during growth at different osmolarity conditions. Chromosome contact maps exhibit a main diagonal of high interaction frequency (black arrow). The thickness of this diagonal and the frequency of off-diagonal interactions varies with growth conditions, and along the length of the chromosome at the same growth condition. The panel on the far right illustrates the alignment of the macrodomains of the *E. coli* chromosome with the contact maps. **Organism:** *Escherichia coli* MG1655 Δ*endA* (NT331); **3C-based study:** Hi-C; **Resolution:** 10 kb; **Growth conditions: Panel A:** Low-salt LB medium (0.08 M NaCl), 37 ºC, exponential phase, **Panel B:** Low-salt LB medium (0.08 M NaCl) up to an OD_{600} of ~1.0 followed by a hyperosmotic shock with 5.0 M NaCl to a final concentration of 0.3 M for 10 minutes, 37 ºC, **Panel C:** High-salt LB medium (0.3 M NaCl), 37 ºC, exponential phase; **Fixation conditions:** 80% cold methanol for 10 minutes followed by 3% formaldehyde for 1 hour; **Restriction enzyme:** PsuI (ThermoFisher Scientific); **Fractionation:** Yes.

The structure of the chromosomal region in the vicinity of the *proVWX* operon reorganizes upon changes to the external environment. This region has been marked with a red triangle in the left panels of Figure 3.5 and is represented in the right panels of Figure 3.5. The position of *proVWX* is marked with white arrows

in the left panels, and with white '+' marks in the right panels (Figure 3.5). The chromosome around *proVWX* decompacts locally when *E. coli* cells in a low-salt medium are subjected to a hyperosmotic shock, while maintaining features of the finer chromosome organization, such as loops (marked with black arrows, Figures 3.5A and 3.5B, right panels) and the distinct 'flare' at 2.37 Mb (marked with white squares, Figures 3.5A and 3.5B, right panels). In a high salt environment, a condition that reflects the adaptation of *E. coli* to higher osmolarity following a hyperosmotic shock, chromosomal regions either decompact further such as the chromatin encompassing, and positioned locally downstream of *proVWX*, or show a stronger compaction compared to growth in a low-salt medium, for instance, the region encompassing the 'flare' at 2.37 Mb (marked with a white square, Figure 3.5C, right panel).

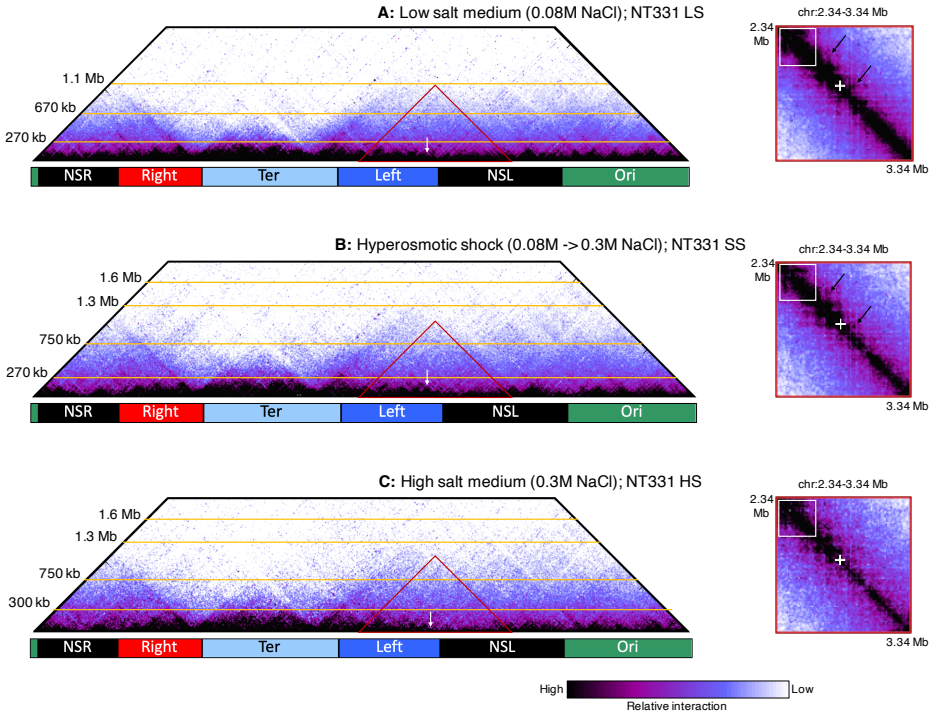

Figure 3.5: The *Escherichia coli* chromosome shows global and local changes to the chromosome contact profiles upon changes to the osmolarity of the growth medium, and during adaptation to altered osmolarity. A, left panel: High frequency interactions (black) in NT331 cells growing in low-salt LB medium occur over distances of up to ~270 kb across the chromosome. Long-range, lower frequency interactions, observed in varying shades of purple, occur largely over distances of up to 1.1 Mb in non-Ter regions and ~670 kb in the Ter macrodomain; **B & C, left panels:** Upon a hyperosmotic shock **(B)**, and in high salt media **(C)**, high frequency interactions still occur at distances of up to ~270-300 kb. Long range, lower frequency interactions occur at distances of up to 1.3-1.6 Mb in non-Ter regions. In the Ter macrodomain, these interactions do not extend far beyond ~750 kb; **A & B, right panels:** The chromosome around *proVWX* (also marked with a red triangle in the left panels; the

position of *proVWX* is marked with white arrows in the left panels and with white '+' marks in the right panels) decompacts locally when *E. coli* cells growing exponentially in a low-salt medium **(A)** are subjected to a hyperosmotic shock **(B)**. The local chromosome maintains features of the finer chromosome organization, such as loops (black arrows) and the 'flare' at 2.37 Mb (white squares). **C, right panel:** In a high salt environment, chromosomal regions are either decompacted compared to growth in a low-salt medium **(A)** such as the chromatin encompassing, and positioned locally downstream of *proVWX*, or show a stronger compaction, for example, at the region encompassing the 'flare' at 2.37 Mb (white square).

Hi-C in bacteria is limited by its resolution. Chromosomal gene density, the scarcity of intergenic DNA, and the short length of individual genes and operons means that an *E. coli* Hi-C map with, in our hands, a 10 kb resolution cannot be used to identify the underlying genetic features that encode global and finer structural changes to the chromosome, or the significance of these changes. Chromosome contact maps with a higher structural resolution assembled from 3C-Seq instead of Hi-C will be used to glean the contributing features.

The difference in local chromosome structure is associated with a change in the transcription profile of the *proVWX* operon

The global and finer structure of the chromosome is modified in response to changing osmolarity. Nucleoid associated proteins that regulate chromosome architecture also function as transcription factors, hence, the change in chromosome architecture may be reflected in transcription. We investigated the transcription profile of *proU* – an osmo-sensitive operon regulated by an osmo-sensitive NAP, H-NS – using RT-qPCR. As required by the MIQE guidelines (91), the details of RNA yield and purity (A_{260}/A_{280} measurements), and the results of RNA inhibition testing are provided in Supplementary file 3.1. Additionally, the results of a DNA contamination assessment of the RNA preparations showing no detectable contamination is provided in Figure S3.3.

Early studies examining the osmosensitivity of the *proU* operon involved the translational fusion of β-galactosidase to a truncate of ProV, and the subsequent detection of the specific activity of the enzyme in a variety of genetic backgrounds and osmolarity conditions as a measure of *proU* activation. While revolutionary, the technique is limited in that it relies on the post-translational detection of gene/operon activation, and it remains relatively ineffective in evaluating the transcriptional profile across an operon. To overcome this, we used RT-qPCR to study the osmo-sensitivity of *proU* at a transcriptional level. Eleven primer pairs were designed to evaluate the transcriptional profile across the operon and its flanking genes (Supplementary file 3.1; Figure 3.6). Primer specificity was determined with Sanger sequencing of the amplified product (Supplementary file

3.2; Supplementary folder 3.5). Identity of the amplicons was gauged with melting curves (Figure S3.4).

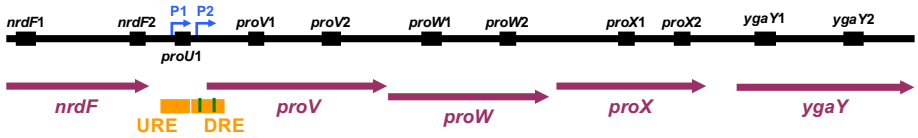

Figure 3.6: The positions of RT-qPCR amplicons (labelled, black) along *proVWX*, *nrdF*, and *ygaY* (purple arrows). P1 and P2 (right angle arrows, blue) designate the positions of the *proVWX* promoters recognised by σ^S and σ^{70}, respectively. URE and DRE (orange) mark the positions of the upstream and downstream regulatory elements of *proVWX*. The green bars within the DRE illustrate the positions of high-affinity H-NS binding sites.

Three internal controls, *rpoD*, *hcaT*, and *rrsA*, were selected for this study. *rpoD* encoding the RNA polymerase σ^{70} factor, is a house-keeping gene that has been validated as a stably-expressed mRNA suitable as an internal control in a diversity of bacterial species including *Klebsiella pneumoniae* (92), *Pseudomonas aeruginosa* (93), *Pseudomonas brassicacearum* GS20 (94), and *Gluconacetobacter diazotrophicus* (95). *hcaT* encodes a predicted 3-phenylpropionic transporter and has been validated as a suitable internal control in *Escherichia coli* (96, 97). *rrsA* codes for 16S rRNA and occurs in six copies in the *E. coli* MG1655 chromosome. It is accepted as a stably expressed house-keeping gene and was accepted as a validated internal control for *E. coli* RT-qPCR experiments (97). *rrsA* has been used to normalise relative expression levels in RT-qPCR studies of the *proU* operon (47). We tested the amplicon as a potential internal control, but, the low Cq values of *rrsA* in comparison to the Cq values of amplicons of the *proU* operon (Supplementary files 3.4 and 3.5) dissuaded the classification of *rrsA* as a reliable internal control. The ~2-fold higher expression of *rpoD* to *hcaT* motivated the use of only one internal control at a time for normalisation, since normalisation with a geometric average of the two amplicons biases the normalisation towards the higher expressed amplicon. The RT-qPCR results described here have been normalised using *rpoD* as the internal control. Equivalent data normalised with *hcaT* expression have been provided in the supplementary files for comparison.

The transcriptional profile of proU in NT331

The transcriptional profile across *proU* shows that the central *proW* gene has a lower relative expression level than the flanking *proV* and *proX* genes and that the terminal *proX* gene is expressed at a higher level than *proV*, in agreement with genome-wide RNA-seq studies (98). This trend is observed at 0.08 M NaCl, 0.3 M NaCl, and upon a hyperosmotic shock (Figures 3.7A-3.7C and S3.5A-S3.5C; Tables

S3.2 and S3.3). Mechanistically, the decline in relative expression between *proV* and *proW* may be accounted for by transcription termination at the junction of the two genes, while the sharp increase in expression between *proW* and *proX* may arise as a result of the presence of an internal promoter between the two genes. The increased transcript level in the downstream region of *proW* (amplicon *proW*2) compared to its upstream end (amplicon *proW*1) (Figures 3.7A-3.7C and S3.5A-S3.5C) implicates the presence of an additional *proX* promoter that lies within the *proW* ORF. Indeed, RNAP σ^{70} ChIP studies show an elevation in RNAP σ^{70} occupancy towards the downstream end of *proW*. However, a distinct RNAP σ^{70} peak within *proW* that may demarcate the additional internal promoter is not observed (Figure S3.6) (99). Nevertheless, a genome-wide study aimed at mapping RNA G-quadruplexes (rG4) in the *E. coli* transcriptome detected the presence of rG4 structures within the *proW* coding sequence (100), that occur between the *proW*1 and *proW*2 amplicons (Supplementary file 3.1). Using the *hemL* transcript that encodes glutamate-1-semialdehyde aminotransferase (aminomutase) as a model, rG4s were shown to play a role in the stabilisation of transcripts (100). K^+ stabilises rG4s when the ion occupies the centre of the quartet (101). Extrapolation of these findings to rG4s at *proW* hints that at higher intracellular concentrations of K^+, the increase in the relative expression level of *proX* transcripts initiated from the hypothetical internal promoter between *proW*1 and *proW*2 may be detected as a result of the stabilisation of rG4s at the 5' region of the transcript that, in turn, stabilises the transcript. The *proX* promoters are likely stringently-regulated non-canonical promoters rather than classical H-NS-repressed spurious promoters. H-NS ChIP shows no H-NS signal at *proX* (Figure S3.6) (102), and spurious transcripts have not been detected from *proX* in a Δ*hns* background (David C. Grainger, personal communication).

The *proVWX* operon is repressed in NT331 cells growing exponentially in a medium with an NaCl concentration of 0.08 M. Upon a hyper-osmotic shock that raises [NaCl] from 0.08 M to 0.3 M, *proVWX* expression increases up to ~8-fold (Figures 3.7D and S3.5D). The spike in expression may be mediated by the relief of H-NS-mediated repression as a result of the cytoplasmic influx of K^+ that occurs as an initial response to increased extracellular osmolarity (28–34). *In vitro* studies promote a model where the influx of K^+ drives a conformational change in the H-NS—DNA nucleoprotein structure at the NRE of *proVWX* from a transcriptionally-repressive DNA—H-NS—DNA bridge to a transcriptionally-conducive H-NS—DNA filament (20, 24). Exponentially-growing NT331 in a high-salt environment of 0.3 M NaCl, express *proVWX* ~1.5- to 2.5-fold higher than during exponential growth

at 0.08 M NaCl, and up to 4.5-fold lower than expression following a hyperosmotic shock (Figures 3.7E-3.7F and S3.5E-S3.5F). Exponential growth at 0.3 M NaCl reflects the adaptation of *E. coli* to increased extracellular osmolarity brought about by the import of osmoprotectants, the synthesis of trehalose, and the export of K^+ (28, 39). The export of K^+, in particular, re-instates repression. A higher expression of *proVWX* during exponential growth at 0.3 M NaCl compared to 0.08 M NaCl (Figures 3.7E and S3.5E) may account for the increased requirement of the ProU transporter at higher osmolarity.

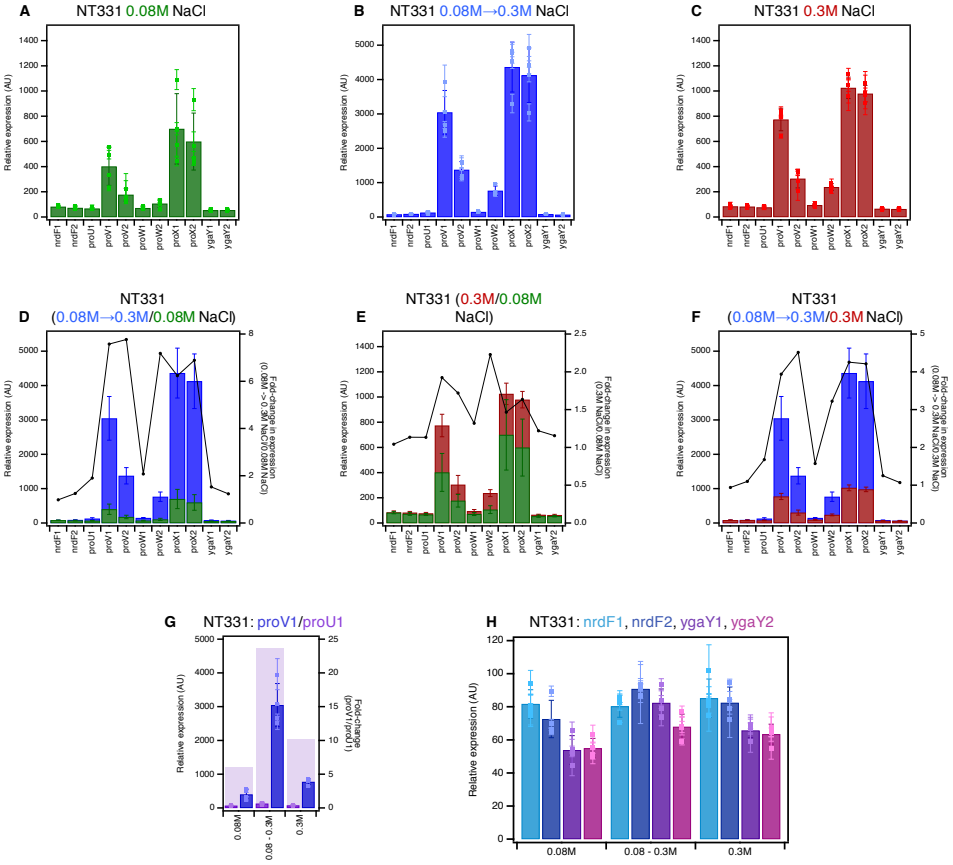

Figure 3.7: The transcriptional profile of *proVWX* and its flanking regions in NT331 during **(A)** exponential growth in M9 medium with 0.08 M NaCl, **(B)** hyperosmotic shock in M9 medium from 0.08 M to 0.3 M NaCl, and **(C)** exponential growth in M9 medium with 0.3 M NaCl. **The fold change in expression level of *proVWX* and its flanking regions** between **(D)** a hyperosmotic shock and exponential growth at 0.08 M NaCl, **(E)** exponential growth at 0.3 M NaCl and 0.08 M NaCl, and **(F)** a hyperosmotic shock and exponential growth at 0.3 M NaCl. **(G) The fold difference in expression at the *proV*1 amplicon compared to the *proU*1 amplicon** during exponential growth at 0.08 M NaCl, following a hyperosmotic shock, and during exponential growth at 0.3 M NaCl. **(H) The relative expression at amplicons flanking *proVWX*** during exponential growth at 0.08 M NaCl, following a hyperosmotic shock, and during exponential growth at 0.3 M NaCl. **Internal control: *rpoD***

The fold changes in the expression levels of the constituent genes of *proVWX* differ upon changes to ambient osmolarity. Following a hyperosmotic shock, the expression of *proV* increases ~7.5-fold, the P2 proximal amplicon of *proW* (amplicon *proW*1) increases ~2-fold, the P2 distal amplicon of *proW* (amplicon *proW*2) is expressed ~7-fold higher, and *proX* transcripts increase by a factor of ~6.5. In exponential growth at 0.3 M NaCl, in comparison to 0.08 M NaCl, the expression levels of *proV*, *proW*1, *proW*2, and *proX* increase by factors of ~1.8, ~1.3, ~2.2, and ~1.5, respectively (Figures 3.7D-3.7E, and S3.5D-S3.5E). Differences in the fold-induction or fold-repression of *proV*, *proW*, and *proX* in *E. coli* upon changes to growth conditions have also been observed in genome-wide studies (98). Collectively, the results show that *proV*, *proW*, and *proX* exhibit a degree of independent regulation despite occurring within the same operon. This provokes the hypothesis that the expression of co-regulated genes of an operon may be tweaked by additional factors that operate on individual genes. The *proU* operon encodes an ABC transporter – a member of the largest group of paralogous protein complexes (103). The components of ABC transporters are contained within operons, the earliest of which is predicted to have arisen before the divergence of bacteria and archaea (104, 105). The organization of ABC operons is evolutionarily conserved and is specific for each orthologous group (106, 107). In this light, the independent regulation of the constituent genes of *proU* suggests that other ABC transporter operons evolutionarily-related to *proVWX*, regardless of the host organism, may carry similar regulatory features.

Transcription of *proVWX* primarily initiates from its σ^{70}-dependent (P2) promoter positioned 60 bp upstream of the *proV* ORF. The *proVWX* σ^{S}-dependent (P1) promoter located at -250 bp of *proV* is cryptic and is activated by *rho* and *hns* mutations, and by cold stress (40). To record the contribution, if any, of P1 to the expression of *proVWX* in a wild-type NT331 background, the relative expression level of amplicon *proU*1 positioned between the P1 and P2 promoters was determined. At 0.08 M NaCl, *proU*1 was expressed ~6-fold lower than amplicon *proV*1 positioned 345 bp downstream of P2. Upon a hyperosmotic shock, the relative expression of *proU*1 increased ~2-fold, however, the expression was ~25-fold lower than that of *proV1*. During exponential growth at 0.3 M NaCl, the expression of *proU*1 was comparable to that at 0.08 M NaCl, and ~10-fold lower than *proV*1 (Figures 3.7G and S3.5G). This indicates that while the osmo-response of *proVWX* primarily arises from initiation at P2 (58, 59, 108), the activation of P1 contribution may ensue from the dismantling of the H-NS—DNA nucleoprotein

during the K^+ influx, to form a nucleoprotein structure that mimics an *hns* knock-down phenotype. Such a structure would alleviate Rho-dependent termination of transcripts initiated from P1 (40, 41, 98). Furthermore, P1 can contribute to the increased expression of the operon during a hyper-osmotic shock. Transcription from P1 across P2 may favour the relief of H-NS repression at the NRE (109, 110).

To detect cross-talk between the expression of *proU* and its flanking genes, the relative expression levels of *nrdF* and *ygaY* positioned upstream and downstream of *proU*, respectively, were determined. In the NT331 background, the expression of *ygaY* and *nrdF* was comparable for growth at 0.08 M NaCl, 0.3 M NaCl, and following a hyper-osmotic shock (Figures 3.7H and S3.5H; Tables S3.2 and S3.3), indicating insulation from flanking chromatin. It is important to note, however, that the expression of the *nrdF* amplicon proximal to *proU* (amplicon *nrdF*2) and both *ygaY* amplicons (amplicons *ygaY*1 and *ygaY*2) were detectably higher after a hyperosmotic shock. This may occur due to an increased local density of RNAP at this osmotic condition, or the decompaction of the local chromatin following the shock providing a more conducive environment for transcription.

The transcriptional profile of proVWX upon alleviation of H-NS-mediated repression at the DRE

H-NS-mediated *proU* repression was alleviated by introducing a series of point mutations in the AT-rich H-NS-binding regions that were experimentally detected by an *in vitro* DNase-I protection assay (49) in the *proU* DRE. This approach was chosen over *hns* deletion to prevent the pleiotropic effects associated with the latter. In this design, the -35 and -10 promoter elements of P2, the P2 TSS, and the Shine-Dalgarno sequence of *proVWX* were not edited. However, two point mutations were introduced in the high affinity H-NS binding site extending between -7 and +15 of the P2 TSS. AA>GC and TA>GC mutations were carried out at -3 to -2 and at +7 to +8 positions, respectively. AT-rich codons in H-NS binding sites in the *proV* ORF were switched out for GC-rich variants with the most similar codon usage ratio in the *E. coli* chromosome. Identical mutations, selected on the basis of the aforementioned criteria, were incorporated into both high-affinity H-NS binding sites occurring in the DRE (48). Following mutation, the AT-content of the DRE was lowered from 66.4% to 51.6% (Supplementary file 3.1, see Feature NT644_DRE). The strain was labelled NT644. The decrease in affinity of the mutated DRE for H-NS was validated *in vitro* using an electrophoretic mobility shift assay (Supplementary methods, Figure S3.8).

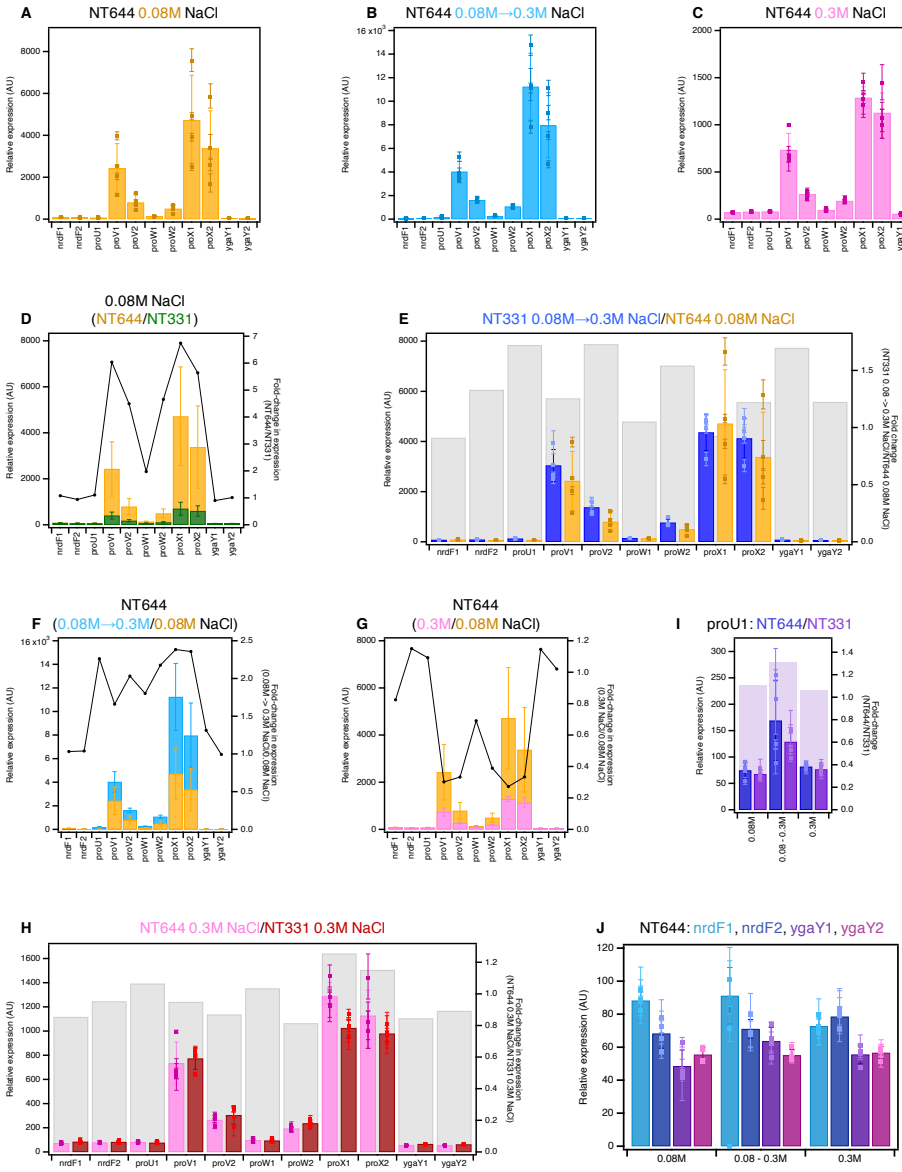

Figure 3.8: The transcriptional profile of *proVWX* and its flanking regions in NT644 during **(A)** exponential growth in M9 medium with 0.08 M NaCl, **(B)** hyperosmotic shock in M9 medium from 0.08 M to 0.3 M NaCl, and **(C)** exponential growth in M9 medium with 0.3 M NaCl. **The fold change in expression level of *proVWX* and its flanking regions** between **(D)** NT644 and NT331 during exponential growth at 0.08 M NaCl, **(E)** NT331 following a hyperosmotic shock and NT644 growing exponentially at 0.08 M NaCl, **(F)** a hyperosmotic shock and exponential growth at 0.08 M NaCl for NT644, **(G)** exponential growth at 0.3 M NaCl and 0.08 M NaCl for NT644, and **(H)** NT644 and NT331 growing exponentially at 0.3 M NaCl. **(I) The fold change in expression at the *proU*1 amplicon** between NT644 and NT331 during exponential growth at 0.08 M NaCl, following a hyperosmotic shock, and during exponential growth at 0.3 M NaCl. **(J) The relative expression level in NT644 at amplicons flanking *proVWX*** during exponential growth at 0.08 M NaCl, following a hyperosmotic shock, and during exponential growth at 0.3 M NaCl. **Internal control: *rpoD***

Alleviating H-NS binding at the *proU* operon activates the expression of its constituent genes at 0.08 M NaCl by up to ~6.5-fold (Figures 3.8A, 3.8D, S3.8A, and S3.8D; Tables S3.4 and S3.5). This is in line with observations by Nagarajavel *et al*., 2007, where, in a Δ*hns* background at 0.05 M, and 0.1 M NaCl, the β-galactosidase activity of a *proV-lacZ* fusion expressed from a construct cloned downstream of the P2 promoter, URE, and DRE on a plasmid was ~9- and ~4-fold higher than in the wild-type background (42). The relative expression of *proVWX* in NT644, a strain deficient in H-NS at the *proU* regulatory region, at 0.08 M NaCl is comparable to the relative expression in NT331, the wild-type strain, after a hyper-osmotic shock (0.08 M to 0.3 M NaCl) (Figures 3.8E and S3.8E; Tables S3.2-S3.5).

The *proVWX* osmoregulation studies performed in (42) show that the specific activity of β-galactosidase of a *proV-lacZ* fusion in a Δ*hns* background at 0.05 M, and 0.1 M NaCl is similar to the specific activity of proV-β-galactosidase in a wild-type background growing exponentially at 0.3 M NaCl, not wild-type cells during a hyperosmotic shock as in our observations. However, the post-translational detection of osmosensitivity in (42) may account for the differences between the results in (42) and those presented here. In this model, the up-shift of transcript levels following a hyper-osmotic shock rapidly establishes the required number of ProU transporters, while the decreased transcript levels in *E. coli* adapted to hyper-osmotic stress maintain the necessary levels of ProU.

We notice a disparity between our observations and those presented in (42) when examining the relative expression of *proU* in NT644. A hyper-osmotic shock to NT644, induces the expression of *proVWX* by ~2-fold (Figures 3.8B, 3.8F, S3.8B, and S3.8F), and upon adaptation to the hyperosmotic stress, represented by exponential growth at 0.3 M NaCl, *proVWX* expression levels decline to as low as up to ~25% of those at 0.08 M NaCl (Figures 3.8C, 3.8G, S3.8C, and S3.8G). Our results also show that NT644 (H-NS-deficient *proU* regulatory element) and NT331 (wild-type) have similar expression levels of *proU* at 0.3 M NaCl (Figures 3.8H and S3.8H; Tables S3.2-S3.5). This suggests that in *E. coli* cells adapted to higher osmolarities, the repression of *proU* is either mediated by factors other than H-NS occupancy at the *proU* promoter, or that H-NS occupancy at the mutated GC-rich *proU* promoter is favoured by one or more additional factors.

Expression from P1 is repressed in a Δ*hns* background (32, 43). The mutations at the *proVWX* regulatory element in NT644 are designed to disrupt H-NS binding to

the DRE (Supplementary file 3.1, see Feature NT644_DRE). H-NS occupancy at the URE, and effectively, at P1, (Figure S3.6) should remain unaffected. Indeed, the relative expression level of the *proU*1 amplicon was similar between NT331 and NT644 at the tested osmolarity conditions (Figures 3.8I and S3.8I).

Disruption of H-NS binding to the DRE did not affect the insulation of the *proVWX* operon. The relative expression levels of the flanking *nrdF* and *ygaY* genes were similar between NT331 and NT644 during growth at 0.08 M NaCl, 0.3 M NaCl, and following a hyperosmotic shock (Figures 3.7H, 3.8J, S3.5H, and S3.8J; Tables S3.2-S3.5).

The role of StpA in the regulation of the proU operon

StpA is a paralogue of H-NS that complements the protein in Δ*hns* strains (63–65). StpA stimulates the formation of DNA—H-NS—DNA bridges *in vitro* and stabilises the structure against changes in temperature and Mg^{2+} or K^{+} concentration (111). ChIP studies reveal that H-NS-bound regions of the chromosome contain StpA (67). At the *proVWX* operon, StpA occupies two sites within the NRE that overlap with H-NS-bound regions. The first site encompasses the P1 promoter and the second lies downstream of P2 and spans across the *proV* structural gene. For ease of communication, these sites are henceforth referred to as Site P1 and Site *proV* in this chapter. H-NS occupancy at *proVWX* appears to be unaffected in a Δ*stpA* background. In Δ*hns* strains, StpA only occupies Site P1 at *proVWX* – the nucleoprotein structure at Site *proV* is lost (67). This binding pattern may explain why the *proVWX* operon is only repressed by StpA when StpA is over-expressed in a Δ*hns* background (66). However, the role of StpA in *proVWX* regulation in an otherwise wild-type background is unclear. Therefore, we investigated the effect of *stpA* deletion on the osmoresponse of *proVWX* in NT331.

At 0.08 M NaCl, *stpA* deletion elevates the relative expression levels of all amplicons within the *proU* structural genes – with the exception of *proV*2 and *proW*1 – by ~4-fold (Figures 3.9A-3.9B, and S3.9A-S3.9B; Tables S3.2, S3.3, S3.6, and S3.7). *In vitro* observations of the architectural properties of StpA-deficient and StpA-supplemented H-NS—DNA structures (111) encourage the prediction that this rise in expression may be driven by an increased sensitivity of the repressive H-NS—DNA nucleoprotein at *proVWX* to intracellular K^{+} concentrations. The relative expression level of amplicon *proV*2, positioned on the *proV* ORF distal to the P1 and P2 promoters was ~7-fold higher upon *stpA* deletion, compared to the ~4-fold increase for amplicon *proV*1 that is positioned closer to the promoters (Figures 3.9A-3.9B, and S3.9A-S3.9B; Tables S3.2, S3.3,

S3.6, and S3.7). From an alternate perspective, the average relative expression level of *proV*2 at 0.08 M NaCl in NT331 was 44% of that of amplicon *proV*1; in NT331 Δ*stpA*, this value rose to 69%. This reflects an increased processivity of RNAP on the *proV* ORF in the absence of StpA, implying that StpA-deficient H-NS—DNA nucleoprotein complexes that form over the *proV* ORF, and by extension, on other sites throughout the chromosome, function as weaker transcription roadblocks than StpA-supplemented H-NS—DNA structures. The relative expression level of the *proW*1 amplicon was similar in both NT331 and NT331 Δ*stpA* (Figures 3.9A-3.9B, and S3.9A-S3.9B; Tables S3.2, S3.3, S3.6, and S3.7). This may be attributed to the strength of the terminator hypothesized to lie between *proV* and *proW*.

A hyperosmotic shock to NT331 Δ*stpA* from 0.08 M to 0.3 M NaCl increased the relative expression of *proV* and *proW* by ~14- to ~20-fold, and *proX* by ~10-fold (Figures 3.9C-3.9D, and S3.9C-S3.9D; Tables S3.6 and S3.7). In NT331, the increase stands at less than 8-fold (Figures 3.7B, 3.7D, S3.5B, and S3.5D; Tables S3.2 and S3.3). NT331 Δ*stpA* cells adapted to growth at 0.3 M NaCl express *proU* ~3- to ~4-fold higher than cells growing at 0.08 M NaCl and ~2.5- to ~4-fold lower than cells subjected to a hyperosmotic shock (Figures 3.9E-3.9G and S3.9E-S3.9G; Tables S3.6 and S3.7). These observations further support the model that StpA-deficient H-NS—DNA nucleoprotein filaments have a heightened osmosensitivity and lowered osmostability such that the structure is much more efficiently dismantled by K^+ (111).

Transcription initiation from P1 was lower in Δ*stpA* mutants compared to wild-type cells during exponential growth at 0.08 M and 0.3 M NaCl (Figures 3.9H and S3.9H; Tables S3.6 and S3.7). This is complementary to observations that expression from P1 is decreased in Δ*hns* strains (32, 43). How a generally repressive nucleoprotein complex of H-NS and StpA enhances expression from a promoter encapsulated within its structure is unclear. The puzzle is further complicated with the paradoxical observation that upon a hyperosmotic shock, a condition that dismantles H-NS—DNA complexes, expression from P1 increases and is similar between NT331, and NT331 Δ*stpA*.

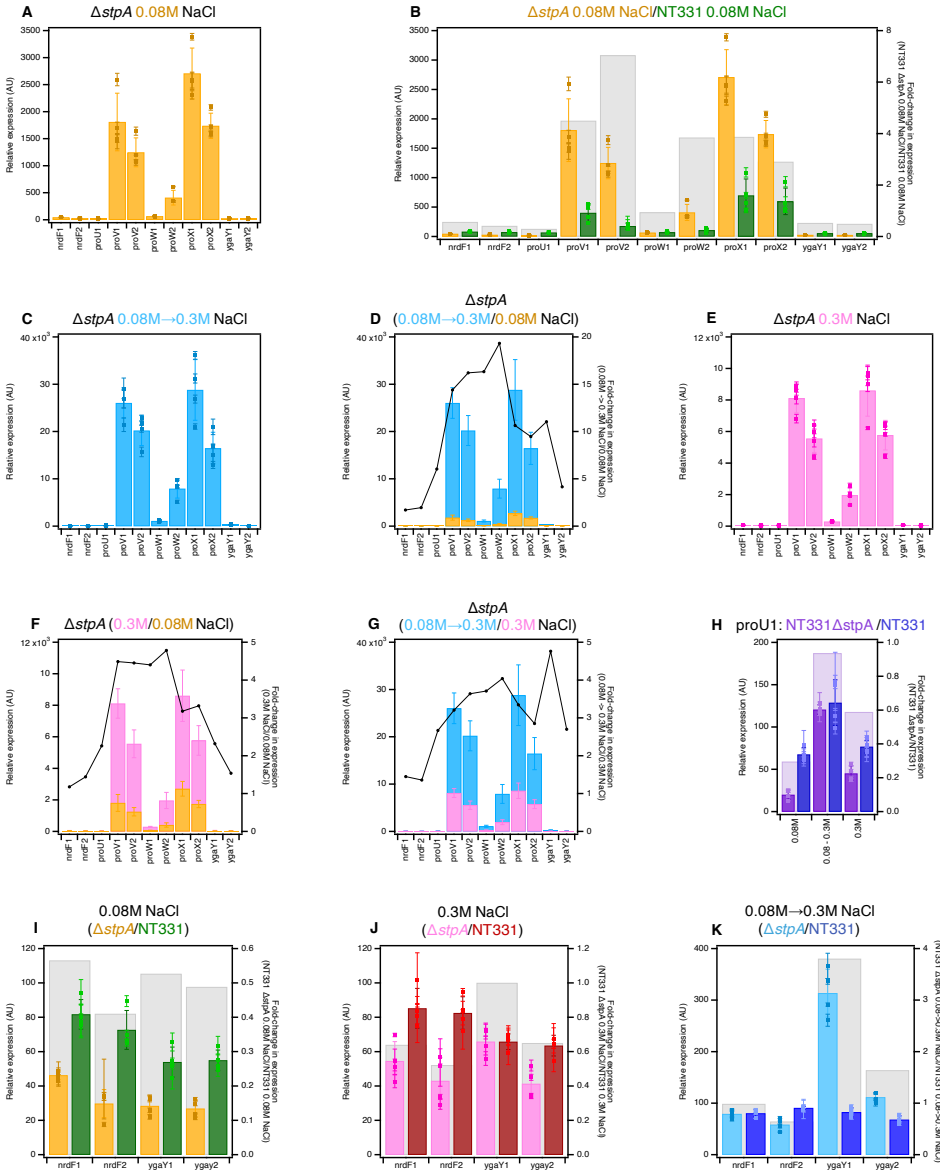

Figure 3.9: The transcriptional profile of the *proVWX* operon and its flanking regions in NT331 Δ*stpA* (A) during exponential growth at 0.08 M NaCl and **(B)** the fold-change in the expression levels of the amplicons compared to NT331, **(C)** upon a hyperosmotic shock from 0.08 M to 0.3 M NaCl, and **(D)** the fold-change in expression levels of the amplicons in comparison to exponential growth at 0.08 M NaCl, and **(E)** during exponential growth at 0.3 M NaCl, and the fold-change in expression levels of the amplicons with respect to **(F)** exponential growth at 0.08 M NaCl, and **(G)** a hyperosmotic shock. **(H) The fold-difference in expression level of amplicon *proU*1** between NT331 Δ*stpA* and NT331. **The fold-change in expression levels of the *nrdF* and *ygaY* amplicons between NT331 Δ*stpA* and NT331 (I)** during exponential growth at 0.08 M NaCl, **(J)** exponential growth at 0.3 M NaCl, and **(K)** following a hyper-osmotic shock. **Internal control: *rpoD***.

The expression of *nrdF* and *ygaY* genes in NT331 Δ*stpA* was affected by the osmotic condition. Both genes showed ~50% repression at 0.08 M NaCl (Figures 3.9I-3.9J, and S3.9I-S3.9J; Tables S3.2, S3.3, S3.6, and S3.7). A perceptible increase in expression at 0.3 M NaCl was observed, that was still maintained at ~50% of that in the wild-type background when expression was normalised relative to *rpoD* (Figures 3.9I-3.9J; Tables S3.2 and S3.6). When normalisation was performed using *hcaT* as an internal control, the expression was comparable to the wild-type background (Figures S3.9I and S3.9J; Tables S3.3 and S3.7). Upon a hyperosmotic shock to NT331 Δ*stpA*, the expression of *nrdF*, positioned upstream of *proU*, increased ~2-fold to a level comparable to that of NT331 under the same condition. Moreover, the expression of *ygaY*, positioned downstream of *proU*, increased 11-fold at the *ygaY*1 amplicon positioned proximal to the terminus of *proX* and 4-fold at the *ygaY*2 amplicon positioned further downstream, corresponding to an increase of 3.8-fold and 1.6-fold, respectively, compared to the wild-type strain (Figures 3.9K and S3.9K; Tables S3.2, S3.3, S3.6, and S3.7). This highlights that StpA insulates *proVWX* from its flanking operons, perhaps by constraining supercoils (65). Indeed, a weak ChIP signal for FLAG-tagged StpA is observed at the terminus of the *proVWX* operon (67). The decline in expression between *ygaY*1 and *ygaY*2 may be accounted for by the crypticity of *ygaY* (112, 113). Nine in-frame stop codons occur between the two amplicons.

The role of RNaseIII in regulating the expression of proU

RNaseIII, encoded by the *rnc* gene, regulates the expression of *proVWX* at a post-transcriptional level. In hypo-osmotic conditions and upon a hypo-osmotic shock, RNaseIII downregulates *proVWX* by cleaving a conserved secondary structure that forms at position +203 to +293 of the *proU* mRNA transcribed from P2. High osmolarity conditions inhibit the action of RNaseIII on the *proU* mRNA (47). The report in (47) was limited in that the regulatory role of RNaseIII on *proVWX* expression was studied using a plasmid-encoded construct of the *proU* regulatory elements and full-length *proV* in a strain carrying a chromosomal *ΔproVWX* mutation. Therefore, we built on this report and determined the effect of a Δ*rnc* mutation in an otherwise wild-type background on the regulation of chromosomal *proVWX* expression.

The *proVWX* operon was expressed perceptibly higher in NT331 Δ*rnc* compared to NT331 during exponential growth at 0.08 M NaCl (Figures 3.10A-3.10B, and S3.10A-S3.10B). The fold increase in the relative transcription level of amplicon *proV*2 – positioned distal to the P1 and P2 promoters– was higher than that of the

*proV*1 amplicon positioned closer to P1 and P2 (Figures 3.10B, and S3.10B). This indicates an increased stability in the absence of RNaseIII and highlights that in addition to the processing of the conserved hairpin located at +203 to +293 of the *proU* transcript, RNaseIII downregulates the expression of *proU* by degrading *proV* transcripts from the 3' end. Interestingly, the transcript level of *proX* in NT331 Δ*rnc* at 0.08 M NaCl was reduced to ~50% of that in NT331 (Figures 3.10B, and S3.10B). Since RNaseIII degrades RNA, the decrease in relative expression of *proX* may be triggered by decreased initiation from the predicted internal *proX* promoter. How the knock-out of an RNase could trigger such an effect is unclear.

A hyperosmotic shock from 0.08 M to 0.3 M NaCl, increased the expression of *proV* and *proX* by ~15-fold, *proW*1 by ~5-fold, and *proW*2 by ~11-fold (Figures 3.10C-3.10D, and S3.10C-S3.10D). In comparison to NT331, the relative expression levels of *proV* and *proW* were >2.4-fold higher in NT331 Δ*rnc* (Figures 3.10E, and S3.10E). In contrast, the relative expression of *proX* upon a hyperosmotic shock was similar for NT331 and the Δ*rnc* mutant (Figures 3.10E, and S3.10E). This indicates that during a hyper-osmotic shock RNaseIII specifically degrades transcripts initiating from P1 and P2, but does not interfere with transcripts expressed from the predicted internal *proX* promoter. This is in support of the inferences put forward in (47) that implicate a hairpin at the 5' end of *proU* transcripts in signalling RNaseIII-mediated processing, however, it does not explain the increased stability of 3' regions of *proU* transcripts in the Δ*rnc* mutant (Figures 3.10D-3.10E, and S3.10D-S3.10E).

During exponential growth at 0.3 M NaCl, *proV* and *proX* are induced 7.5- to 8.5-fold in comparison to growth at 0.08 M NaCl; *proW*1 is induced ~3-fold and *proW*2, ~5.5-fold (Figures 3.10F-3.10G, and S3.10F-S3.10G). The increase is in line with expectations of *proU* induction at higher osmolarities. The relative expression level of *proW* and *proX* in the Δ*rnc* mutant at 0.3 M NaCl is ~2-fold higher than in NT331. *proV*1 is ~5-fold more abundant and proV2, ~11-fold (Figures 3.10H, and S3.10H). This indicates that upon adaptation to higher osmolarity, RNaseIII contributes to downregulating the expression of *proU*. RNaseIII preferentially targets *proV* transcripts and destabilises the transcripts at the 3' end. The increase in the relative expression level of *proX* in NT331 Δ*rnc* at 0.3 M NaCl with respect to NT331 (Figures 3.10H, and S3.10H), implicates RNaseIII in *proX* processing. This is in contrast of *proX* expression at 0.08 M NaCl where RNaseIII knock-out represses the gene.

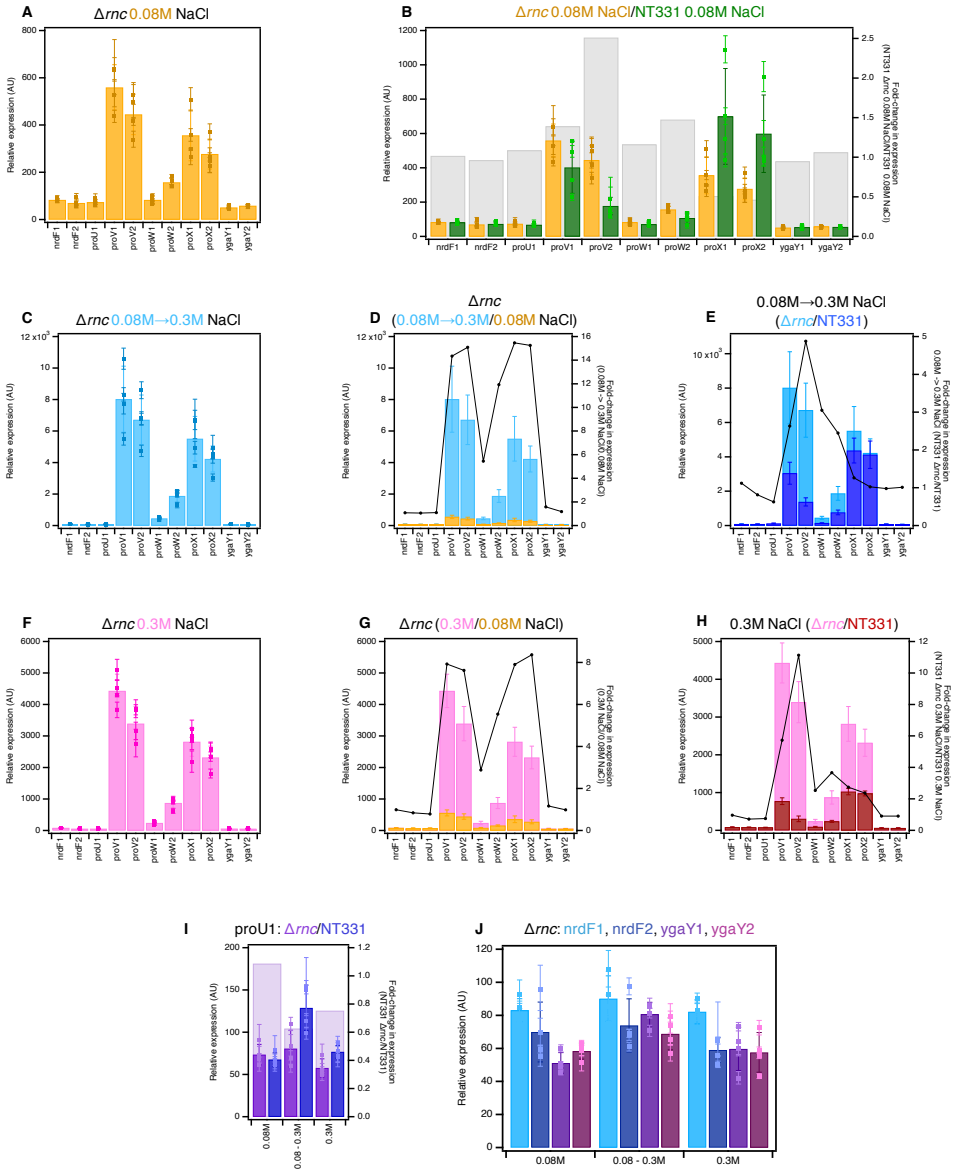

Figure 3.10: The transcriptional profile of *proVWX* and its flanking regions in NT331 Δ*rnc* during **(A)** exponential growth at 0.08 M NaCl, and **(B)** the fold-change in expression of the amplicons compared to NT331 growing exponentially at 0.08 M NaCl, upon **(C)** a hyperosmotic shock from 0.08 M NaCl to 0.3 M NaCl, and the fold-change in expression of the amplicons in comparison to **(D)** NT331 Δ*rnc* growing exponentially at 0.08 M NaCl, and **(E)** NT331 following a hyperosmotic shock. **The transcription profile of *proVWX* and its flanking regions in NT331 Δ*rnc*** during **(F)** exponential growth at 0.3 M NaCl, and the fold-change in expression of the amplicons relative to **(G)** NT331 Δ*rnc* growing exponentially at 0.08 M NaCl, and **(H)** NT331 growing exponentially at 0.3 M NaCl. **(I) The fold-difference in the relative expression of the *proU*1 amplicon** between NT331 Δ*rnc* and NT331. **(J) The relative expression level in NT331 Δ*rnc* at amplicons flanking *proVWX*** during exponential growth at 0.08 M NaCl, following a hyperosmotic shock, and during exponential growth at 0.3 M NaCl. **Internal control: *rpoD*.**

In NT331 Δ*rnc*, transcription from P1 is comparable to the wild-type background (Figures 3.10I, and S3.10I). *nrdF* and *ygaY* are insulated from *proU* and exhibit similar expression levels at high and low osmolarity that are comparable to the wild-type (Figures 3.10J, and S3.10J).

Structural analysis of the *proVWX* operon.

The expression of *proVWX* is regulated by H-NS – a NAP that responds to changes in osmolarity by modifying DNA architecture *in vitro* (20). H-NS may, therefore, regulate *proVWX* by modifying the local three-dimensional chromosome structure *in vivo*.

Live cell FROS imaging

To visualize the changes in the three-dimensional organization of *proVWX* in response to changing osmolarity, we used fluorescent-repressor operator system (FROS) labelling in live cells (114, 115). For this, the upstream and downstream ends of *proVWX* were labelled with Tet operator (TetO) and Lac operator (LacO) arrays, respectively (Supplementary file 3.1). Each array carries six repressor binding sites (Supplementary file 3.1) and accommodates a maximum of six dimers of fluorescently-labelled repressors. The arrays were flanked by terminators to account for terminator sequences (Supplementary file 3.1) that may have been disrupted by the insertion, and to ensure that transcription does not occur across the arrays to prevent interference with repressor binding. The fluorescently-labelled repressors (TetR-eYFP and LacI-mCherry) were expressed from under an arabinose-inducible promoter on a pBAD24 construct (pRD183).

A preliminary study was performed in NT455 (MG1655 *proVWX*::TetO-*proVWX*-LacO pRD183), a strain that does not carry a Δ*lac* mutation and, therefore, expresses an unlabelled variant of the Lac repressor. Furthermore, in this strain, LacI-mCherry can bind to the LacO sites in the *lac* operon. Nevertheless, the distance between the sites and the binding of a maximum of two LacI-mCherry molecules at each site means that the *lac* operon would not be detected above the background.

In NT455 growing exponentially in M9 medium with 0.08 M NaCl, the eYFP and mCherry foci that marked the ends of *proVWX* were observed in close proximity $d=94\pm1$ nm, $\sigma=9\pm1$ nm, $N=26$ cells (Figures 3.11A, and 3.11Da). The distance of ~100 nm lies at the limit of resolution of the TIRF microscopy set-up used in

this study. In this case, therefore, the foci can be considered to occur on top of each other. The observations imply that during exponential growth at 0.08 M NaCl – an osmotic condition at which *proVWX* is repressed (Figures 3.7A and S3.5A) – the operon forms a loop (Figure 3.11Db).

When an exponentially-growing culture of NT455 is subjected to a hyperosmotic shock in M9 medium that raises the concentration of NaCl from 0.08 M to 0.3 M, the eYFP and mCherry foci are detected at a distance of 436±7 nm, σ= 100±10 nm (N=45 cells) from each other (Figures 3.11B, and 3.11Ea). This indicates that the loop that forms between the ends of *proVWX* at 0.08 M NaCl disengages upon a hyperosmotic shock (Figure 3.11Eb) – a condition that is associated with a ~2- to ~8-fold increase in the expression of *proVWX* ORFs (Figures 3.7D, and S3.5D).

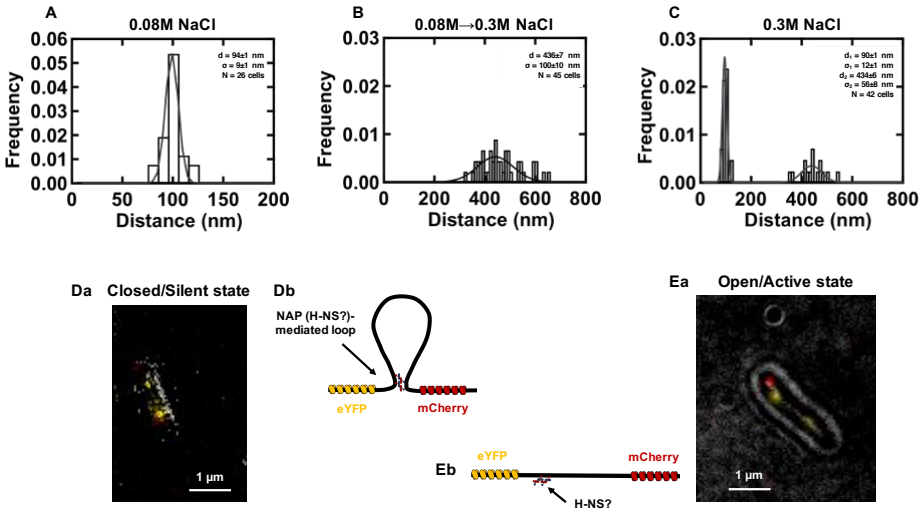

Figure 3.11: The three-dimensional organization of *proVWX* correlates with its expression state. **A:** In NT455 cells growing exponentially at osmolarity conditions where *proVWX* is repressed (0.08 M NaCl), the eYFP and mCherry foci that mark the ends of the operon lie in close proximity d=94±1 nm, σ=9±1 nm, N=26 cells. **B:** The foci diverge from each other following a hyperosmotic shock from 0.08 M to 0.3 M NaCl – an osmotic condition at which the expression of *proVWX* increases ~2- to ~8-fold; 436±7 nm, σ= 100±10 nm, N=45 cells. **C:** During exponential growth at 0.3 M NaCl, a condition at which the relative expression level of *proVWX* is between that of exponential growth at 0.08 M NaCl and that following a hyperosmotic shock, NT455 cells show two distinct populations with regards to the conformation of *proVWX*. A population in which the eYFP and mCherry foci lie in close proximity (d=90±1 nm, σ=12±1 nm, N=26), and another in which the foci diverge (434±6 nm, σ=56±8 nm, N=16). *D:* eYFP and mCherry foci occur in close proximity in cells where *proVWX* is repressed/silenced. This may arise as a result of the formation of a loop anchored between the ends of the operon. The loop may be mediated by H-NS. **E:** eYFP and mCherry foci lie ~400nm apart in cells where *proVWX* is activated. This may occur due to the destabilization of an H-NS-mediated loop between the ends of the operon.

During exponential growth at 0.3 M NaCl, an osmotic condition that signifies the adaptation of *E. coli* to a hyperosmotic shock, FROS signals in NT455 indicate the occurrence of two distinct populations of *E. coli* with regards to the conformation of *proVWX*: a population in which the operon occurs in its looped, silent conformation (d=90±1 nm, σ=12±1 nm, N=26), and another in which the operon exists in its open, active state (434±6 nm, σ=56±8 nm, N=16) (Figures 3.11C-3.11E).

The results show that the regulation of *proVWX* involves a structural aspect. To model the three-dimensional structure of *proVWX* at a higher resolution, we extended our study to ensemble chromosome conformation capture.

3C-qPCR

Hi-C probes the global conformation and contact profile of the chromosome (116). However, the Hi-C libraries prepared using PsuI as the restriction enzyme in our studies reliably afforded a resolution of only 10 kb. Since our region of interest in the chromosome that spans across the *proVWX* operon and includes its flanking regions is ~7 kb long (Supplementary file 3.1), the region is contained within a single pixel of the Hi-C maps (Figures 3.3-3.5). Hence, structural changes to the local chromatin cannot be resolved with Hi-C. Therefore, we considered 3C-qPCR (77) – a 'one-to-one' technique that probes the relative interaction frequency between only two loci at a time but affords a resolution of individual restriction digestion fragments. NlaIII was selected as the restriction enzyme for our study since the enzyme digests the regulatory region of *proVWX* in a way that separates the URE from the DRE, and the high-affinity H-NS binding sites in the DRE from each other (Figure 3.12, Supplementary file 3.1). In this experiment, fragment proU3_NlaIII (Figure 3.12, Supplementary file 3.1) that contains the *proVWX* P2 promoter and TSS was used as an anchor, and its relative interaction frequency with other restriction digestion fragments within the ~7kb region was investigated.

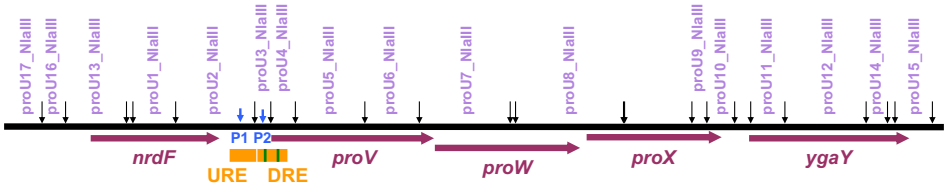

Figure 3.12: NlaIII restriction digestion sites (black arrows) and resulting chromatin fragments selected (purple labels) for the 3C-qPCR-based evaluation of local three-dimensional *proVWX*

structure. *proV*, *proW*, *proX*, *nrdF*, and *ygaY* (purple arrows) designate individual genes. P1 and P2 (blue arrows) mark the positions of the *proVWX* promoters. URE and DRE (orange) illustrate the upstream and downstream regulatory elements of *proVWX*. The green bars show the high-affinity H-NS binding sites within the DRE.

To quantify the relative interaction frequency of proU3_NlaIII with other fragments of *proVWX*, control libraries from digested and randomly re-ligated purified genomic DNA were prepared. The libraries were serially diluted and the hybrid ligation junctions were quantified at each dilution to plot a standard curve. However, only the undiluted and the 10X diluted control libraries produced a reliable fluorescent signal, thus, control libraries prepared from genomic DNA – as described in (77) – could not be used to plot standard curves. An alternative control library suggested in (77) requiring synthesis and equimolar pooling of each individual ligation junction to be probed was used instead. A preliminary test to evaluate the structure of *proVWX* in *E. coli* NT331 was performed with two biological replicates per osmotic condition. The test was carried out in LB medium.

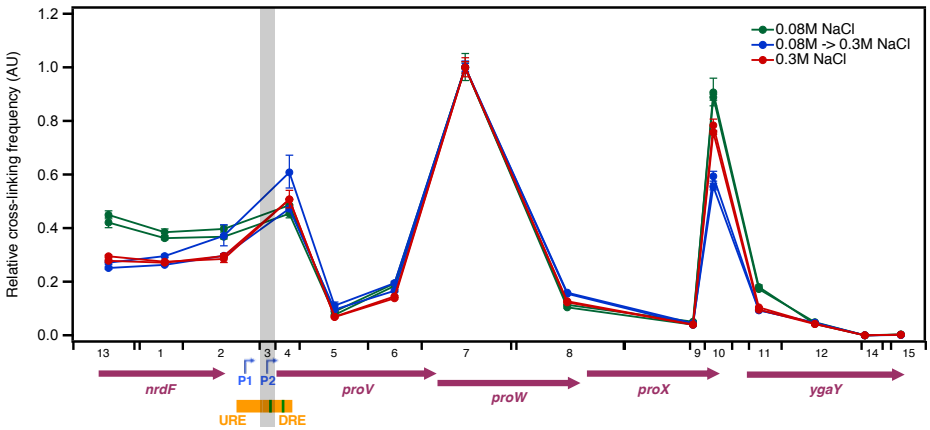

Figure 3.13: A 3C-qPCR study of the relative cross-linking frequency of proU3_NlaIII (highlighted in grey) with chromatin segments within and flanking the *proVWX* operon (marked along the horizontal axis) during exponential growth in LB medium with 0.08 M NaCl (green), following a hyperosmotic shock from 0.08 M to 0.3 M NaCl (blue), and during exponential growth at 0.3 M NaCl (red). Each curve represents the 3C profile of an independent biological replicate. The error bars represent the standard deviation of three quantitation values from the qPCR run. *proV*, *proW*, *proX*, *nrdF*, and *ygaY* (purple arrows) show individual genes. P1 and P2 (right-angled blue arrows) mark *proVWX* promoters. The upstream and downstream regulatory elements of *proVWX* (URE and DRE) are shown with orange bars. The green bars in the DRE designate high-affinity H-NS binding sites. **Internal cross-linking control:** proU3_NlaIII-proU7_NlaIII.

In NT331 cultures growing exponentially at 0.08 M NaCl, cultures subjected to a hyperosmotic shock, and cultures growing exponentially at 0.3 M NaCl, the proU3_NlaIII fragment exhibits three distinct interaction peaks. In order of

decreasing strength of the relative interaction frequency, proU3_NlaIII interacts with proU7_NlaIII which extends across the upstream half of the *proW* ORF, proU10_NlaIII which overlaps with the terminus of *proVWX*, and proU4_NlaIII that includes the downstream high-affinity H-NS binding site of the DRE (Figure 3.13; Tables S3.10-S3.12; Supplementary file 3.1).

The interaction between proU3_NlaIII and proU7_NlaIII (Figure 3.13; Tables S3.10-S3.12) sparks interest since it overlaps with the region that includes the *proW*1 amplicon (Supplementary file 3.1) that shows a dip in transcript levels in RT-qPCR studies (Figures 3.7-3.10, S3.5, and S3.8-S3.10; Tables S3.2-S3.9). The proU7_NlaIII fragment also lies just upstream of the *proW*2 RT-qPCR amplicon where the relative expression levels show a rise (Figures 3.7-3.10, S3.5, and S3.8-S3.10; Tables S3.2-S3.9). It is tempting to speculate that the proU3_NlaIII-proU7_NlaIII interaction functions as a transcription roadblock that contributes to the decreased expression at *proW*1 or even that it potentially plays a role in a coordinated regulation between P2 and the hypothetical internal promoter that may lie in this region. The proU3_NlaIII-proU7_NlaIII interaction is stable. Its stability is reflected in its reliability as an internal control. The *proVWX* interaction profiles of NT331 biological replicates at four separate osmolarity conditions tested in LB overlapped when the proU3_NlaIII-proU7_NlaIII interaction was used as an internal cross-linking control (Figure S3.11; Tables S3.10-S3.13).

NT331 *proVWX* 3C-qPCR profiles normalized to the proU3_NlaIII-proU7_NlaIII interaction show a distinctive feature at the proU10_NlaIII fragment (Figure 3.13; Tables S3.10-S3.12). At 0.08 M NaCl, when *proVWX* is repressed (Figures 3.7A, and S3.5A), the relative crosslinking frequency of proU3_NlaIII with proU10_NlaIII, a 195 bp region that includes the end of the *proX* ORF and the terminus of *proVWX* (Supplementary file 3.1), is ~0.9. This is ~4.5-fold higher than the proU3_NlaIII-proU11_NlaIII interaction and ~20-fold higher than that between proU3_NlaIII and proU9_NlaIII. This indicates that elements within fragment proU10_NlaIII form a bridge with the segment of the DRE that encompasses P2. This is in line with observations from live-cell FROS imaging that show that during exponential growth at 0.08 M NaCl, the ends of the *proVWX* operon lie in close proximity (Figure 3.11A). ChIP studies show that the DRE is bound by H-NS (Figure S3.6). Extrapolating the inferences from *in vitro* H-NS studies (20, 24), we propose a regulatory model on the basis of our ensemble 3C-qPCR and single-cell FROS microscopy observations that at low osmolarity conditions which are associated with a low intracellular concentration of K^+ (28),

H-NS adopts its bridging-capable conformation *in vivo*. The *proVWX* DRE forms an H-NS-mediated bridge with the terminus of the operon that functions as a transcription roadblock and represses *proVWX* (Figure 3.14).

A hyperosmotic shock to *E. coli* cells is associated with a rapid intracellular influx of K^+ (28). An osmotic condition that, *in vitro*, disrupts H-NS—DNA—H-NS bridges, thus, promoting the formation of transcriptionally-conducive H-NS—DNA filaments (20, 24). Following an increase in the NaCl concentration of the growth medium from 0.08 M to 0.3 M, the relative interaction frequency between proU3_NlaIII and proU10_NlaIII drops ~30% to ~0.6 (Figure 3.13; Tables S3.10 and S3.11). Indeed, live cell FROS imaging shows the divergence of the ends of *proVWX* following a hyperosmotic shock (Figure 3.11B). We expand our model to include the dismantling of the bridging interaction between the region of the DRE that carries the P2 promoter and the terminus of *proVWX* following a hyperosmotic shock to form an H-NS—DNA structure that does not impede *proVWX* expression (Figure 3.14).

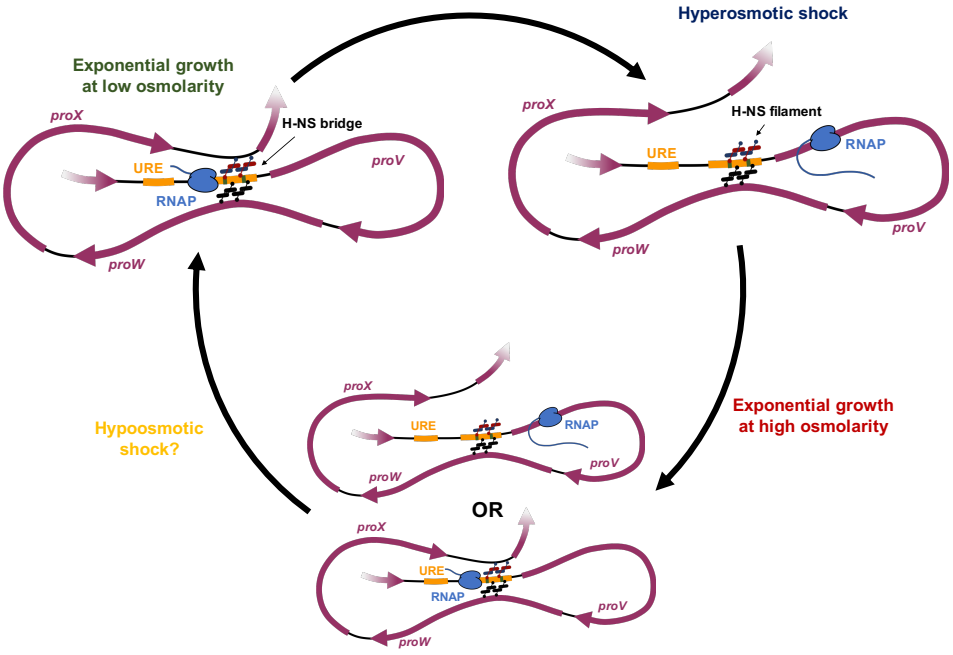

Figure 3.14: A model of the structural regulation of *proVWX* expression. Exponential growth at low osmolarity: During exponential growth at low osmolarity, a DNA—NAP—DNA bridge, likely mediated by H-NS, forms between the DRE and the terminus of *proVWX*. The bridge acts as a transcription roadblock that represses the operon. *In vitro* studies suggest that the formation of the H-NS-mediated bridge is promoted by the low cytoplasmic concentrations of K^+ that occur during growth in low osmolarity media. Decreased K^+ favors the bridging-capable conformation of H-NS (20). *In vitro*

experiments also indicate that the DNA—H-NS—DNA nucleoprotein structure functions as a transcription roadblock (24). **Hyperosmotic shock:** A hyperosmotic shock to *E. coli* drives a rapid cytoplasmic influx of K^+, that, under *in vitro* conditions, de-stabilises H-NS-mediated DNA bridges to form H-NS—DNA filaments that are conducive to transcription (20, 24). *In vivo*, a hyperosmotic shock dismantles the bridge between the DRE and the end of *proVWX* to form an H-NS—DNA filament across which RNA polymerase can transcribe. **Exponential growth at high osmolarity:** Adaptation to hyperosmotic stress is associated with the intracellular accumulation of osmoprotectants, and the decline of cytoplasmic K^+. The decrease in K^+ re-instates DNA bridging by H-NS that manifests as the re-establishment of a bridge between the DRE and the *proVWX* terminus. The bridge only forms in a fraction of cells where it silences the operon. In another population of *E. coli*, a decrease in the cytoplasmic concentration of osmoprotectants triggers the influx of K^+ that dismantles the bridge between the DRE and the terminus of *proVWX*, hence, activating the operon. **Hypoosmotic shock:** Preliminary experiments indicate that a hypoosmotic shock to *E. coli* rapidly establishes the bridge between the *proVWX* DRE and terminus to silence the operon.

Adaptation to hyperosmotic stress is associated with the intracellular accumulation of osmoprotectants, the decline of cytoplasmic K^+ (28), and, consequentially, the repression of *proVWX* (Figures 3.7C and S3.5C; Tables S3.2 and S3.3). During exponential growth at 0.3 M NaCl, the relative interaction frequency between proU3_NlaIII and proU10_NlaIII is increased compared to *E. coli* subjected to a hyperosmotic shock (Figure 3.13; Tables S3.11 and S3.12), but is still lower than exponential growth at 0.08 M NaCl (Figure 3.13; Tables S3.10 and S3.12). This observation from ensemble 3C-qPCR supports single-cell FROS microscopy studies that show that *proVWX* in *E. coli* cells in a medium with 0.3 M NaCl occurs either in its open, active conformation or in its closed, repressed state (Figure 3.11C). These results suggest that upon adaptation to high osmolarity, the decrease in intracellular K^+ favors the formation of H-NS—DNA—H-NS bridges. The formation of a bridge between proU3_NlaIII and proU10_NlaIII in a fraction of cells silences *proVWX*. In another population of *E. coli*, a decrease in the cytoplasmic concentration of osmoprotectants triggers the influx of K^+, the dismantling of the bridge between proU3_NlaIII and proU10_NlaIII, and hence, the expression of *proVWX* (Figure 3.14).

Fragment proU3_NlaIII also shows a high relative interaction frequency with fragment proU4_NlaIII that encompasses the downstream half of the DRE and contains the second high-affinity H-NS binding site (Figures 3.12-3.13; Supplementary file 3.1). Under the osmotic conditions investigated in this study, the frequency of the proU3_NlaIII-proU4_NlaIII interaction remains comparable (Figure 3.13), and may, therefore, be mediated by the physical proximity of the fragments rather than a regulatory purpose.

In NT331 cultures growing at 0.08 M NaCl, proU3_NlaIII shows a higher relative interaction frequency with proU13_NlaIII than in cultures growing at 0.3 M NaCl or cultures subjected to a hyperosmotic shock (Figure 3.13). Fragment proU13_NlaIII encompasses the end of *nrdE* and the beginning of *nrdF* (Figure 3.12, Supplementary file 3.1). Preliminary studies show that the proU3_NlaIII-proU13_NlaIII interaction in cultures subjected to a hypoosmotic shock from 0.3 M to 0.08 M NaCl is similar to cultures growing exponentially at 0.08 M NaCl (Figure S3.11). This implies the presence of a regulatory element within this region. Additional investigations will be required to identify the regulatory element and its role.

Single molecule Förster resonance energy transfer (smFRET) studies

3C-qPCR detected the non-dynamic, ensemble organization of *proVWX*. To study the single-molecule dynamics and the biophysical mechanism of the organization of *proVWX*, we visualized the structural dynamics of elements of *proVWX* immobilized on a glass surface using single-molecule Förster resonance energy transfer (smFRET) in combination with TIRF microscopy. The combinatorial approach affords a spatial resolution of 10-100Å, and a temporal resolution of 33 ms.

To verify the applicability of smFRET in visualizing structural dynamics of immobilized DNA molecules, a 250 bp-long DNA construct used in an earlier study by our laboratory to report on H-NS-mediated DNA bridging (20) was labelled with Cy3 and Cy5 as FRET donor and acceptor fluorophores, respectively, and with Biotin-TEG for immobilization onto a streptavidin-coated glass surface (Table S3.1). Henceforth, constructs with the above described features will be referred to as smFRET-compatible. FRET between the donor and acceptor fluorophores was not observed in the absence of H-NS (Figure 3.15A). In the presence of 200 nM H-NS, in a buffer supplemented with 10 mM Mg^{2+} to favor H-NS-mediated bridging (20), two structural configurations of the DNA substrate with FRET efficiencies of 0.16±0.07 and 0.50±0.12 were detected, corresponding to distances of 79Å and 60Å, respectively, between the fluorophores (Figures 3.15B-3.15D). These observations show intra-molecular bridging by H-NS, and highlight that the structural change associated with the formation of the bridges and the structural state adopted by an individual DNA molecule can be detected by smFRET.

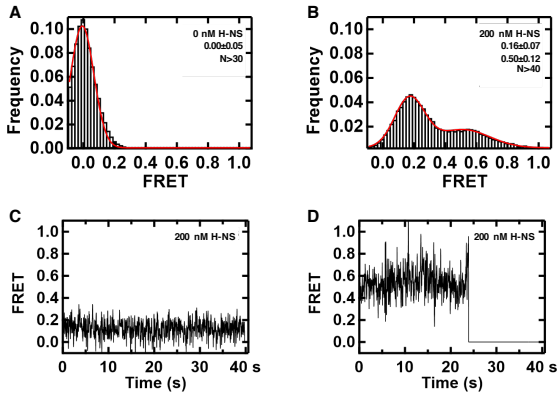

Figure 3.15: H-NS forms intramolecular bridges within a 250 bp-long, AT-rich DNA substrate. A: In the absence of H-NS, the FRET efficiency recorded for 250bp AT-rich DNA substrates is 0.00±0.05 (N>30). **B:** At 200 nM H-NS, the DNA substrates are folded into two structural configurations with FRET efficiencies of 0.16±0.07 and 0.50±0.12 (N>40). **C, D:** Representative FRET traces of single DNA molecules in the presence of 200 nM H-NS.

H-NS does not mediate the formation of a bridge between the proVWX URE and DRE

The *proVWX* URE and DRE function in concert to coordinate the expression of *proVWX* (42). Whether this requires a structural interaction between the two regulatory elements, such as the formation of a loop, is unclear. The 3C-qPCR studies presented earlier do not provide conclusive evidence that structural organization contributes to the coordinated role of the URE and DRE. Therefore, we investigated if the formation of bridge between the URE and DRE mediated by H-NS is possible.

A 460 bp smFRET-compatible DNA construct spanning the regulatory elements was used for this purpose. Given that the persistence length of DNA is 50 nm – approximately 150 bp – the 460 bp construct covers three persistence lengths and is, therefore, capable of forming an end-to-end loop. Despite extensive data acquisition in a Mg^{2+}-supplemented buffer (20) at H-NS concentrations ranging from 10-200 nM, only few reliable FRET traces representing H-NS-mediated bridge formation were identified. This points to the rarity of the event, indicating that either *proVWX* regulation by the URE and DRE may not involve the formation of a loop between the pair of elements, or that a NAP-mediated bridge cannot form within the 460 bp URE-DRE construct. To account for the latter, the smFRET experiments were repeated with Rok and MvaT – H-NS family proteins in *Bacillus sp*. and *Pseudomonas sp*., respectively (21, 117). Rok folds the DNA construct to form intramolecular bridges with FRET efficiencies of 0.19±0.09 and 0.42±0.12 (Figures 3.16A-3.16C). A mutated variant of MvaT ($MvaT_{F36D,M44D}$) that cannot

oligomerize, and, therefore, forms DNA—MvaT—DNA bridges but not DNA—MvaT filaments (21), also folds the 460 bp construct into structures with FRET efficiencies between ~0.2 and ~0.5 (Figures 3.16D-3.16F). Collectively, the results show that a NAP-mediated bridged complex within a DNA fragment comprising of the *proVWX* URE and DRE can be formed. However, the formation of the intramolecular bridge by H-NS is a rare occurrence and may, therefore, not carry a biological significance.

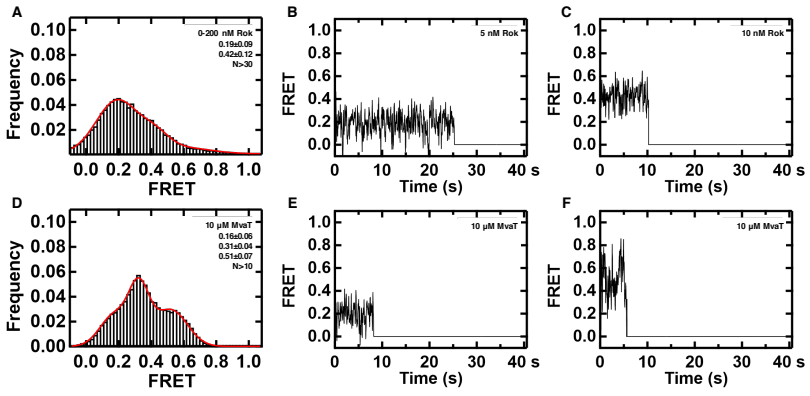

Figure 3.16: A bridged nucleoprotein complex between the *proVWX* URE and DRE can be mediated by Rok and MvaT$_{F36D,M44D}$. A: Rok folds the URE-DRE DNA construct to form intramolecular bridges with FRET efficiencies of 0.19±0.09 and 0.42±0.12 (N>30). **B, C:** Representative FRET traces of Rok-structured DNA constructs. **D:** MvaT$_{F36D,M44D}$ folds the DNA into structures with FRET efficiencies between ~0.2 and ~0.5. **E, F:** Representative traces of MvaT-structured DNA molecules.

The interaction between the proVWX P2 and proW

3C-qPCR of *proVWX* shows that the chromatin fragment proU3_NlaIII that carries the P2 promoter interacts with fragment proU7_NlaIII that spans the upstream half of *proW*. The resolution afforded by NlaIII as the restriction enzyme in the 3C study cannot pinpoint the precise location of the interaction. To elucidate this, a preliminary *in vitro* smFRET study was performed. Six smFRET-compatible DNA constructs – ProW1 to ProW6 – were designed. The Biotin-TEG- and Cy3-labelled ends of the constructs were positioned at -46 relative to P2, and the Cy5-labelled ends terminated at various positions within the proU7_NlaIII fragment, ~100 bp apart (Figure 3.17). FRET efficiencies for the constructs were determined at 0 nM and 200 nM H-NS in a buffer supplemented with 10 mM Mg^{2+}. H-NS was selected for the study since the protein is a bridging-capable NAP that shows a strong ChIP signal in the proU3_NlaIII fragment (67, 102).

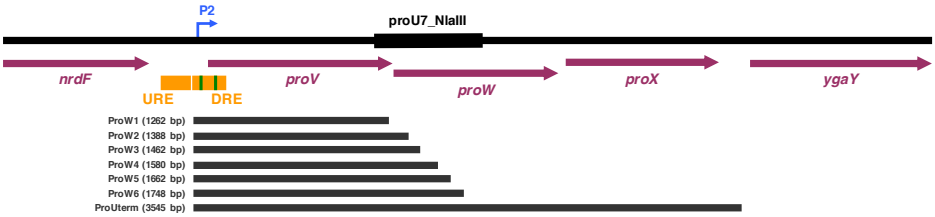

Figure 3.17: smFRET constructs (grey) designed to study loop formation between the *proVWX* P2 promoter (right-angle arrow, blue), and the proU7_NlaIII fragment (black bar) and terminus of the operon. Purple arrows represent ORFs. URE and DRE (orange) mark the positions of the upstream and downstream regulatory elements of *proVWX*. The green bars within the DRE illustrate the positions of high-affinity H-NS binding sites.

FRET was not observed for ProW1 and ProW2 in the absence or presence of H-NS, indicating that H-NS does not form a bridge between P2 and the ends of the ProW1 and ProW2 constructs under our experimental conditions (Figures 3.18A-3.18B). It is important to note that our experimental design is only sensitive to the formation of a bridge between the ends of an smFRET compatible substrate. Nucleoprotein structures that form internally within the substrate, or between a labelled end and an unlabelled section of the construct cannot be detected.

Constructs ProW3 and ProW4 both show a low efficiency FRET peak, in addition to a peak at 0 FRET at 0 nM H-NS (Figures 3.18C-3.18D, left panels). This suggests that the constructs spend a significant time fraction exploring a bent conformation even in the absence of protein. Indeed, when fragments ProW3 and ProW4 are evaluated with bend.it® (118), a server that predicts the curvature of a DNA molecule from its sequence using the BEND algorithm (119), 28.4% of the ProW3 sequence and 29.2% of ProW4 are predicted to have an intrinsic curvature of >5 degrees per helical turn when the bend angle is calculated over three turns considering an ideal B-DNA structure. An intrinsic curvature of >7.5 degrees per helical turn is predicted for ~9.5% of the two sequences (Predicted curvature window size: 31 bp, curvature parameter: derived from DNaseI digestion, length of helical turn: 10.5 bp). Nevertheless, the bends may not be sufficiently in phase to bring the ends of the DNA substrate in proximity for FRET. The low efficiency FRET state may also be accounted for by DNA duplex pairing (120). The phenomenon suggests that sequence of bases in a DNA duplex generate a backbone twist that doubles as a fingerprint of the molecule. The twist generates a 'coat' of alternating positive and negative charges (in the major groove, and at the phosphate backbone, respectively) around the duplex. The electrostatic 'coat' is only in register with that of a homologous sequence and drives a preferential pairing of the helices. In the presence of Mg^{2+}, a cation that specifically interacts

with DNA, the positive charge of the groove is strengthened and can overcome the repulsion between dsDNA molecules that is mediated by the negatively-charged phosphate backbones (120). Weak homology between sequences at the ends of the smFRET-compatible constructs used in our study may favour a bent conformation, hence a low FRET signal, even in the absence of H-NS. In follow-up studies, atomic force microscopy visualizations of the ProW3 and ProW4 constructs will provide clues regarding preferential conformations that may be adopted by the molecules (121, 122). With 200 nM H-NS, construct ProW3, but not ProW4, shows an additional peak at 0.41±0.15 FRET, corresponding to a distance of 54 Å (Figures 3.18C-3.18D, right panels). This indicates that the end of the ProW3 fragment may form an H-NS-mediated interaction with P2.

Similar to constructs ProW1 and ProW2, construct ProW5 does not show FRET in the absence of H-NS (Figure 3.18E, left panel). At 200 nM H-NS, however, a peak at 0.65±0.08 FRET becomes apparent (Figure 3.18E, right panel). The rarity of this event means that additional data acquisition will be required to validate its significance.

The smFRET observations for construct ProW6 are remarkable. At both, 0 nM and 200 nM H-NS, events with a FRET efficiency of ~0.8 corresponding to a distance of ~47Å are observed (Figure 3.18F). Furthermore, the probability of observing the high FRET state increases in the presence of H-NS. However, traces of this state do not show single-step photobleaching and can only be considered artefactual. To validate the high FRET states by single-step photobleaching, the event will be stimulated in follow-up studies by increasing laser power and measurement duration, and by reducing the concentrations of the oxygen scavenger and anti-blinking/anti-bleaching agent used in the experimental set-up (78). At 200 nM H-NS, events with a FRET efficiency of 0.48±0.06 (61Å) that were validated with single-step photobleaching were observed, indicating that the end of construct ProW6 forms an H-NS-mediated interaction with P2 (Figure 3.18F, right panel). This may account for the high frequency interaction observed between fragments proU3_NlaIII and proU7_NlaIII in 3C-qPCR studies. Interestingly, the additional 86 bp in the ProW6 construct compared to ProW5 lie between the *proW*1 and *proW*2 amplicons investigated with RT-qPCR. On the basis of our RT-qPCR results, we hypothesized that an internal promoter lies in this region.

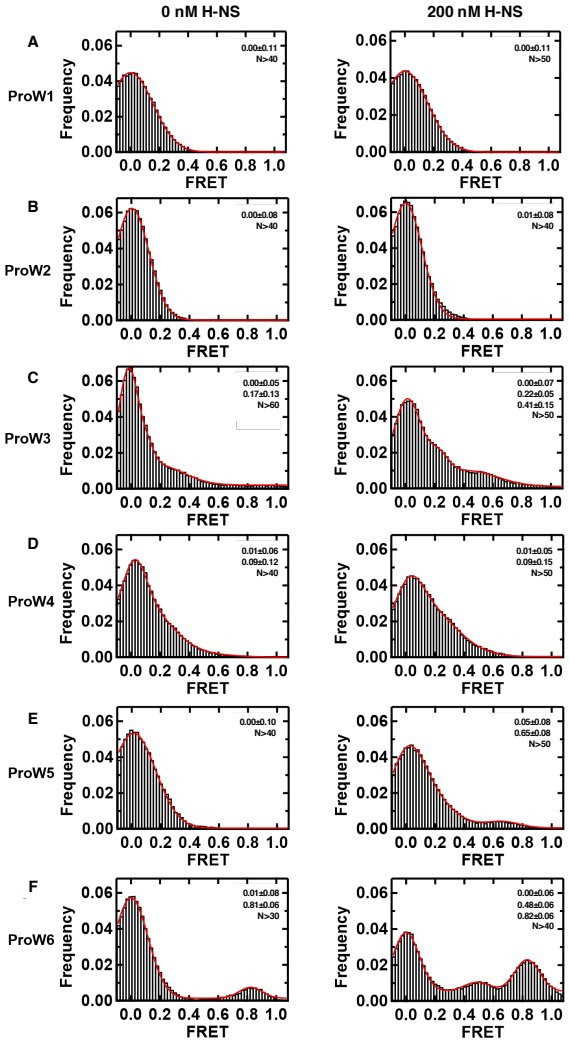

Figure 3.18: H-NS stabilises *proVWX* DRE-ProW3, and DRE-ProW6 loops. FRET distributions of ProW1-ProW6 (A-F) fragments with 0 nM (left) and 200 nM (right) H-NS.

The interaction between proVWX P2 and terminator.

3C-qPCR shows that the segment of the DRE that carries P2 forms an osmo-sensitive interaction with the terminus of *proVWX* that may play a role in the regulation of the operon. We tested the role of H-NS in mediating this interaction using an smFRET-compatible construct extending from -46 to +3499 relative to P2. At 0 nM H-NS no FRET was observed for the constructs with the exception of a single molecule with a FRET efficiency of 0.81±0.09 (Figure 3.19A). Similar to the ~0.8 FRET state detected for the ProW6 constructs, this molecule did not

photobleach and its observation is likely artefactual. At 200 nM H-NS, artefactual high FRET states at 0.95±0.05 were observed (Figure 3.19B). Nevertheless, two additional FRET states with efficiencies of 0.23±0.07 and 0.47±0.05 (N=9) were detected, supporting the occurrence of a bridge between the DRE and the terminus of *proVWX* (Figure 3.19B).

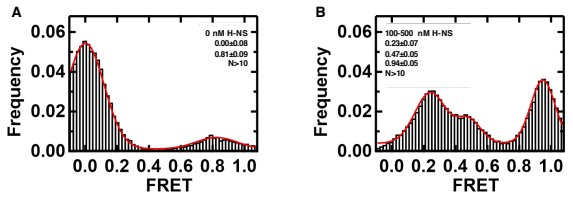

Figure 3.19: H-NS can form a bridge between the *proVWX* DRE and the terminus of the operon. **A:** FRET was not observed for the ProUterm (Figure 3.12) construct at 0 nM H-NS (N>10) with the exception of a single molecule exhibiting an (artefactual) FRET efficiency of 0.81±0.09. **B:** At 200 nM H-NS, FRET states with efficiencies of 0.23±0.07 and 0.47±0.05 (N=9) were detected, in addition to an artefactual FRET state at 0.95±0.05.

Conclusions and perspectives

Nucleoid associated proteins are environmentally sensitive architectural proteins of the bacterial chromosome that drive its compaction and organisation. NAPs also function as transcription factors and regulate the expression of genes in response to environmental stimuli (1–3). We have provided the first *in vivo* evidence that NAPs regulate gene expression by re-modelling local chromatin using the *Escherichia coli proVWX* operon as a model system.

Using a modified 3C-based library preparation technique that includes methanol fixation prior to formaldehyde fixation, and proximity ligation with the insoluble fraction of digested, cross-linked chromatin to improve signal-to-noise ratio, we show that the *E. coli* chromosome undergoes global rearrangements during growth at different osmotic conditions. Ensemble RT-qPCR experiments highlight that conditions which modify chromosome conformation also affect gene expression — *proVWX* in our study — and reveal that despite the occurrence of *proV*, *proW*, and *proX* within a single operon, individual genes show a degree of independent regulation. The role of NAPs in *proVWX* regulation was verified by manipulating H-NS binding profiles at the URE and DRE of the operon and in a Δ*stpA* strain, both of which showed altered gene expression profiles.

The role of StpA in the regulation of *proVWX* is intriguing. RT-qPCR studies show that the deletion of StpA is associated with an up to ~8-fold increase in relative

expression in *proVWX*, an increase in the processivity of RNA polymerase across *proV*, and the loss of insulation of *proVWX* from flanking operons. Collectively, this underlines that StpA has specific functions in transcription regulation that are distinct from those of H-NS and that the deletion of *stpA* from *E. coli* that still expresses H-NS comes at a physiological cost.

By using TIRF microscopy to observe FROS-labelled *proVWX* in single cells, and ensemble 3C-qPCR to model the local three-dimensional conformation of the operon, we show that conditions that repress *proVWX* are associated with the formation of a loop that is anchored between the *proVWX* P2 promoter region and the terminus of the operon. Destabilisation of the loop during hyperosmotic stress is associated with the activation of *proVWX*. The 3C-qPCR studies also reveal an interaction between P2 and the region spanning the end of *nrdE* and the beginning of *nrdF* that is evidently stronger at hypoosmotic stress than hyperosmotic stress. This suggests that the regulatory elements of individual operons may occur within other transcriptional units beyond their mapped regulatory regions, illustrating the importance of studying the regulation of transcriptional units at native chromosomal loci.

It is noteworthy that in *proVWX*, an H-NS-regulated operon, low K^+ concentrations that favour the bridging competent form of H-NS *in vitro* also facilitate the formation of a loop between the ends of the operon *in vivo*. Similarly, higher K^+ concentrations that destabilise the bridging competent structure of H-NS *in vitro* also destabilise the loop between the ends of *proVWX in vivo*. Furthermore, smFRET studies reported here indicate that H-NS can form a loop between the ends of *proVWX*. It is curious that while ChIP studies of the H-NS binding profile show the occurrence of a DNA—H-NS nucleoprotein structure at *proVWX* P2, a corresponding signal is not observed at the terminus of the operon.

The results presented in this chapter show that transcription of an H-NS-regulated operon correlates with its three-dimensional structure. H-NS and H-NS-like proteins are wide-spread amongst bacteria, boasting large regulons in these organisms (117, 123–126). This implies that the structural regulation of gene expression may be a typical feature of transcriptional control in bacteria.

References:

1. Dame,R.T. (2005) The role of nucleoid-associated proteins in the organization and compaction of bacterial chromatin. *Mol. Microbiol.*, 10.1111/j.1365-2958.2005.04598.x.
2. Dame,R.T., Kalmykowa,O.J. and Grainger,D.C. (2011) Chromosomal macrodomains and associated proteins: Implications for DNA organization and replication in gram negative bacteria. *PLoS Genet.*, 10.1371/journal.pgen.1002123.
3. Dame,R.T., Rashid,F.Z.M. and Grainger,D.C. (2020) Chromosome organization in bacteria: mechanistic insights into genome structure and function. *Nat. Rev. Genet.*, **21**, 227–242.
4. Dillon,S.C. and Dorman,C.J. (2010) Bacterial nucleoid-associated proteins, nucleoid structure and gene expression. *Nat. Rev. Microbiol.*, 10.1038/nrmicro2261.
5. Dorman,C.J. (2013) Genome architecture and global gene regulation in bacteria: making progress towards a unified model? *Nat. Rev. Microbiol.*, **11**, 349–55.
6. Rimsky,S. and Travers,A. (2011) Pervasive regulation of nucleoid structure and function by nucleoid-associated proteins. *Curr. Opin. Microbiol.*, 10.1016/j.mib.2011.01.003.
7. Luijsterburg,M.S., White,M.F., Van Driel,R. and Th. Dame,R. (2008) The major architects of chromatin: Architectural proteins in bacteria, archaea and eukaryotes. *Crit. Rev. Biochem. Mol. Biol.*, 10.1080/10409230802528488.
8. Dame,R.T. and Tark-Dame,M. (2016) Bacterial chromatin: Converging views at different scales. *Curr. Opin. Cell Biol.*, **40**, 60–65.
9. Noom,M.C., Navarre,W.W., Oshima,T., Wuite,G.J.L. and Dame,R.T. (2007) H-NS promotes looped domain formation in the bacterial chromosome. *Curr. Biol.*, 10.1016/j.cub.2007.09.005.
10. van der Valk,R.A., Vreede,J., Crémazy,F. and Dame,R.T. (2015) Genomic Looping: A Key Principle of Chromatin Organization. *J. Mol. Microbiol. Biotechnol.*, **24**, 344–359.
11. Atlung,T. and Ingmer,H. (1997) H-NS: A modulator of environmentally regulated gene expression. *Mol. Microbiol.*, 10.1046/j.1365-2958.1997.3151679.x.
12. Navarre,W.W., Porwollik,S., Wang,Y., McClelland,M., Rosen,H., Libby,S.J. and Fang,F.C. (2006) Selective silencing of foreign DNA with low GC content by the H-NS protein in Salmonella. *Science (80-.).*, 10.1126/science.1128794.
13. Falconl,M., Gualtierl,M.T., La Teana,A., Losso,M.A. and Pon,C.L. (1988) Proteins from the prokaryotic nucleoid: primary and quaternary structure of the 15-kD Escherichia coli DNA binding protein H-NS. *Mol. Microbiol.*, 10.1111/j.1365-2958.1988.tb00035.x.
14. Bloch,V., Yang,Y., Margeat,E., Chavanieu,A., Augé,M.T., Robert,B., Arold,S., Rimsky,S. and Kochoyan,M. (2003) The H-NS dimerization domain defines a new fold contributing to DNA recognition. *Nat. Struct. Biol.*, 10.1038/nsb904.
15. Esposito,D., Petrovic,A., Harris,R., Ono,S., Eccleston,J.F., Mbabaali,A., Haq,I., Higgins,C.F., Hinton,J.C.D., Driscoll,P.C., *et al.* (2002) H-NS oligomerization domain structure reveals the mechanism for high order self-association of the intact protein. *J. Mol. Biol.*, 10.1016/S0022-2836(02)01141-5.
16. Ueguchi,C., Suzuki,T., Yoshida,T., Tanaka,K.I. and Mizuno,T. (1996) Systematic mutational analysis revealing the functional domain organization of Escherichia coli nucleoid protein H-NS. *J. Mol. Biol.*, 10.1006/jmbi.1996.0566.
17. Shindo,H., Iwaki,T., Ieda,R., Kurumizaka,H., Ueguchi,C., Mizuno,T., Morikawa,S., Nakamura,H. and Kuboniwa,H. (1995) Solution structure of the DNA binding domain of a nucleoid-associated protein, H-NS, from Escherichia coli. *FEBS Lett.*, 10.1016/0014-5793(95)00079-O.
18. Arold,S.T., Leonard,P.G., Parkinson,G.N. and Ladbury,J.E. (2010) H-NS forms a superhelical protein scaffold for DNA condensation. *Proc. Natl. Acad. Sci. U. S. A.*, 10.1073/pnas.1006966107.
19. Leonard,P.G., Ono,S., Gor,J., Perkins,S.J. and Ladbury,J.E. (2009) Investigation of the self-association and hetero-association interactions of H-NS and StpA from Enterobacteria. *Mol. Microbiol.*, 10.1111/j.1365-2958.2009.06754.x.
20. van der Valk,R.A., Vreede,J., Qin,L., Moolenaar,G.F., Hofmann,A., Goosen,N. and Dame,R.T. (2017) Mechanism of environmentally driven conformational changes that modulate H-NS DNA-Bridging activity. *Elife*, 10.7554/eLife.27369.
21. Qin,L., Bdira,F. Ben, Sterckx,Y.G.J., Volkov,A.N., Vreede,J., Giachin,G., Van Schaik,P., Ubbink,M. and Dame,R.T. (2020) Structural basis for osmotic regulation of the DNA binding properties of H-NS proteins. *Nucleic Acids Res.*, 10.1093/nar/gkz1226.
22. Dame,R.T., Wyman,C. and Goosen,N. (2000) H-NS mediated compaction of DNA visualised by

atomic force microscopy. *Nucleic Acids Res.*, 10.1093/nar/28.18.3504.
23. Dame,R.T., Noom,M.C. and Wuite,G.J.L. (2006) Bacterial chromatin organization by H-NS protein unravelled using dual DNA manipulation. *Nature*, **444**, 387–390.
24. Kotlajich,M. V., Hron,D.R., Boudreau,B.A., Sun,Z., Lyubchenko,Y.L. and Landick,R. (2015) Bridged filaments of histone-like nucleoid structuring protein pause RNA polymerase and aid termination in bacteria. *Elife*, 10.7554/eLife.04970.
25. Sexton,T. and Cavalli,G. (2015) The role of chromosome domains in shaping the functional genome. *Cell*, **160**, 1049–1059.
26. Csonka,L.N. (1982) A third L-proline permease in Salmonella typhimurium which functions in media of elevated osmotic strength. *J. Bacteriol.*, **151**, 1433–1443.
27. Gowrishankar,J. (1985) Identification of osmoresponsive genes in Escherichia coli: Evidence for participation of potassium and proline transport systems in osmoregulation. *J. Bacteriol.*, 10.1128/jb.164.1.434-445.1985.
28. Sleator,R.D. and Hill,C. (2002) Bacterial osmoadaptation: the role of osmolytes in bacterial stress and virulence. *FEMS Microbiol. Rev.*, 10.1111/j.1574-6976.2002.tb00598.x.
29. Cairney,J., Booth,I.R. and Higgins,C.F. (1985) Osmoregulation of gene expression in Salmonella typhimurium: proU encodes an osmotically induced betaine transport system. *J. Bacteriol.*, 10.1128/jb.164.3.1224-1232.1985.
30. Barron,A., May,G., Bremer,E. and Villarejo,M. (1986) Regulation of envelope protein composition during adaptation to osmotic stress in Escherichia coli. *J. Bacteriol.*, 10.1128/jb.167.2.433-438.1986.
31. Sutherland,L., Cairney,J., Elmore,M.J., Booth,I.R. and Higgins,C.F. (1986) Osmotic regulation of transcription: Induction of the proU betaine transport gene is dependent on accumulation of intracellular potassium. *J. Bacteriol.*, 10.1128/jb.168.2.805-814.1986.
32. Rajkumari,K., Kusano,S., Ishihama,A., Mizuno,T. and Gowrishankar,J. (1996) Effects of H-NS and potassium glutamate on σ(S)- and σ70-directed transcription in vitro from osmotically regulated P1 and P2 promoters of proU in Escherichia coli. *J. Bacteriol.*, 10.1128/jb.178.14.4176-4181.1996.
33. Jovanovich,S.B., Record,M.T. and Burgess,R.R. (1989) In an Escherichia coli coupled transcription-translation system, expression of the osmoregulated gene proU is stimulated at elevated potassium concentrations and by an extract from cells grown at high osmolality. *J. Biol. Chem.*
34. Ramirez,R.M. and Villarejo,M. (1991) Osmotic signal transduction to proU is independent of DNA supercoiling in Escherichia coli. *J. Bacteriol.*, 10.1128/jb.173.2.879-885.1991.
35. Dinnbier,U., Limpinsel,E., Schmid,R. and Bakker,E.P. (1988) Transient accumulation of potassium glutamate and its replacement by trehalose during adaptation of growing cells of Escherichia coli K-12 to elevated sodium chloride concentrations. *Arch. Microbiol.*, 10.1007/BF00408306.
36. Gowrishankar,J. (1989) Nucleotide sequence of the osmoregulatory proU operon of Escherichia coli. *J. Bacteriol.*, 10.1128/jb.171.4.1923-1931.1989.
37. May,G., Faatz,E., Villarejo,M. and Bremer,E. (1986) Binding protein dependent transport of glycine betaine and its osmotic regulation in Escherichia coli K12. *MGG Mol. Gen. Genet.*, 10.1007/BF00430432.
38. Lucht,J.M. and Bremer,E. (1994) Adaptation of Escherichia coli to high osmolarity environments: Osmoregulation of the high-affinity glycine betaine transport system ProU. *FEMS Microbiol. Rev.*, 10.1111/j.1574-6976.1994.tb00067.x.
39. Gowrishankar,J. and Manna,D. (1996) How is osmotic regulation of transcription of the Escherichia coli proU operon achieved? A review and a model. *Genetica*, 10.1007/BF00055322.
40. Rajkumari,K. and Gowrishankar,J. (2001) In vivo expression from the RpoS-dependent P1 promoter of the osmotically regulated proU operon in Escherichia coli and Salmonella enterica serovar typhimurium: Activation by rho and hns mutations and by cold stress. *J. Bacteriol.*, 10.1128/JB.183.22.6543-6550.2001.
41. Gowrishankar,J. (1999) Ploughing a lonely furrow: The curious case of the P1 promoter in the osmotically regulated proU operon of Escherichia coli. *J. Indian Inst. Sci.*
42. Nagarajavel,V., Madhusudan,S., Dole,S., Rahmouni,A.R. and Schnetz,K. (2007) Repression by binding of H-NS within the transcription unit. *J. Biol. Chem.*, 10.1074/jbc.M702753200.

43. Dattananda,C.S., Rajkumari,K. and Gowrishankar,J. (1991) Multiple mechanisms contribute to osmotic inducibility of proU operon expression in Escherichia coli: Demonstration of two osmoresponsive promoters and of a negative regulatory element within the first structural gene. *J. Bacteriol.*, 10.1128/jb.173.23.7481-7490.1991.
44. Ueguchi,C. and Mizuno,T. (1993) The Escherichia coli nucleoid protein H-NS functions directly as a transcriptional repressor. *EMBO J.*, 10.1002/j.1460-2075.1993.tb05745.x.
45. Prince,W.S. and Villarejo,M.R. (1990) Osmotic control of proU transcription is mediated through direct action of potassium glutamate on the transcription complex. *J. Biol. Chem.*
46. Overdier,D.G. and Csonka,L.N. (1992) A transcriptional silencer downstream of the promoter in the osmotically controlled proU operon of Salmonella typhimurium. *Proc. Natl. Acad. Sci. U. S. A.*, 10.1073/pnas.89.7.3140.
47. Kavalchuk,K., Srinivasan,M. and Schnetz,K. (2012) RNase III initiates rapid degradation of proU mRNA upon hypo-osmotic stress in Escherichia coli. *RNA Biol.*, 10.4161/rna.9.1.18228.
48. Bouffartigues,E., Buckle,M., Badaut,C., Travers,A. and Rimsky,S. (2007) H-NS cooperative binding to high-affinity sites in a regulatory element results in transcriptional silencing. *Nat. Struct. Mol. Biol.*, 10.1038/nsmb1233.
49. Lucht,J.M., Dersch,P., Kempf,B. and Bremer,E. (1994) Interactions of the nucleoid-associated DNA-binding protein H-NS with the regulatory region of the osmotically controlled proU operon of Escherichia coli. *J. Biol. Chem.*
50. Tanaka,K. ichi, Ueguchi,C. and Mizuno,T. (1994) Importance of Stereospecific Positioning of the Upstream cis-Acting DNA Element Containing a Curved DNA Structure for the Functioning of the Escherichia coli proV Promoter. *Biosci. Biotechnol. Biochem.*, 10.1271/bbb.58.1097.
51. Dame,R.T., Wyman,C. and Goosen,N. (2001) Structural basis for preferential binding of H-NS to curved DNA. *Biochimie*, 10.1016/S0300-9084(00)01213-X.
52. Yamada,H., Muramatsu,S. and Mizuno,T. (1990) An Escherichia coli protein that preferentially binds to sharply curved DNA. *J. Biochem.*, 10.1093/oxfordjournals.jbchem.a123216.
53. Yamada,H., Yoshida,T., Tanaka,K. ichi, Sasakawa,C. and Mizuno,T. (1991) Molecular analysis of the Escherichia coli has gene encoding a DNA-binding protein, which preferentially recognizes curved DNA sequences. *MGG Mol. Gen. Genet.*, 10.1007/BF00290685.
54. Owen-Hughes,T.A., Pavitt,G.D., Santos,D.S., Sidebotham,J.M., Hulton,C.S.J., Hinton,J.C.D. and Higgins,C.F. (1992) The chromatin-associated protein H-NS interacts with curved DNA to influence DNA topology and gene expression. *Cell*, 10.1016/0092-8674(92)90354-F.
55. Tanaka,K. ichi, Muramatsu,S., Yamada,H. and Mizuno,T. (1991) Systematic characterization of curved DNA segments randomly cloned from Escherichia coli and their functional significance. *MGG Mol. Gen. Genet.*, 10.1007/BF00260648.
56. Dame,R.T., Wyman,C., Wurm,R., Wagner,R. and Goosen,N. (2002) Structural basis for H-NS-mediated trapping of RNA polymerase in the open initiation complex at the rrnB P1. *J. Biol. Chem.*, 10.1074/jbc.C100603200.
57. Shin,M., Song,M., Joon,H.R., Hong,Y., Kim,Y.J., Seok,Y.J., Ha,K.S., Jung,S.H. and Choy,H.E. (2005) DNA looping-mediated repression by histone-like protein H-NS: Specific requirement of Eσ70 as a cofactor for looping. *Genes Dev.*, 10.1101/gad.1316305.
58. Lucht,J.M. and Bremer,E. (1991) Characterization of mutations affecting the osmoregulated proU promoter of Escherichia coli and identification of 5' sequences required for high-level expression. *J. Bacteriol.*, 10.1128/jb.173.2.801-809.1991.
59. Manna,D. and Gowrishankar,J. (1994) Evidence for involvement of proteins HU and RpoS in transcription of the osmoresponsive proU operon in Escherichia coli. *J. Bacteriol.*, 10.1128/jb.176.17.5378-5384.1994.
60. Prieto,A.I., Kahramanoglou,C., Ali,R.M., Fraser,G.M., Seshasayee,A.S.N. and Luscombe,N.M. (2012) Genomic analysis of DNA binding and gene regulation by homologous nucleoid-associated proteins IHF and HU in Escherichia coli K12. *Nucleic Acids Res.*, **40**, 3524–3537.
61. Oberto,J., Nabti,S., Jooste,V., Mignot,H. and Rouviere-Yaniv,J. (2009) The HU regulon is composed of genes responding to anaerobiosis, acid stress, high osmolarity and SOS induction. *PLoS One*, 10.1371/journal.pone.0004367.
62. Khodr,A., Fairweather,V., Bouffartigues,E. and Rimsky,S. (2015) IHF is a trans-acting factor implicated in the regulation of the proU P2 promoter. *FEMS Microbiol. Lett.*, 10.1093/femsle/fnu049.
63. Shi,X. and Bennett,G.N. (1994) Plasmids bearing hfq and the hns-like gene stpA complement hns

mutants in modulating arginine decarboxylase gene expression in Escherichia coli. *J. Bacteriol.*, 10.1128/jb.176.21.6769-6775.1994.
64. Zhang,A. and Belfort,M. (1992) Nucleotide sequence of a newly-identified Escherichia coli gene, stpA, encoding an H-NS-like protein. *Nucleic Acids Res.*, 10.1093/nar/20.24.6735.
65. Zhang,A., Rimsky,S., Reaban,M.E., Buc,H. and Belfort,M. (1996) Escherichia coli protein analogs StpA and H-NS: Regulatory loops, similar and disparate effects on nucleic acid dynamics. *EMBO J.*, 10.1002/j.1460-2075.1996.tb00476.x.
66. Williams,R.M., Rimsky,S. and Buc,H. (1996) Probing the structure, function, and interactions of the Escherichia coli H-NS and StpA proteins by using dominant negative derivatives. *J. Bacteriol.*, 10.1128/jb.178.15.4335-4343.1996.
67. Uyar,E., Kurokawa,K., Yoshimura,M., Ishikawa,S., Ogasawara,N. and Oshima,T. (2009) Differential binding profiles of StpA in wild-type and hns mutant cells: A comparative analysis of cooperative partners by chromatin immunoprecipitation- microarray analysis. *J. Bacteriol.*, 10.1128/JB.01594-08.
68. Higgins,C.F., Dorman,C.J., Stirling,D.A., Waddell,L., Booth,I.R., May,G. and Bremer,E. (1988) A physiological role for DNA supercoiling in the osmotic regulation of gene expression in S. typhimurium and E. coli. *Cell*, 10.1016/0092-8674(88)90470-9.
69. Bhriain,N.N., Dorman,C.J. and Higgins,C.F. (1989) An overlap between osmotic and anaerobic stress responses: a potential role for DNA supercoiling in the coordinate regulation of gene expression. *Mol. Microbiol.*, 10.1111/j.1365-2958.1989.tb00243.x.
70. Karem,K. and Foster,J.W. (1993) The influence of DNA topology on the environmental regulation of a pH-regulated locus in Salmonella typhimurium. *Mol. Microbiol.*, 10.1111/j.1365-2958.1993.tb00905.x.
71. Fletcher,S.A. and Csonka,L.N. (1995) Fine-structure deletion analysis of the transcriptional silencer of the proU operon of Salmonella typhimurium. *J. Bacteriol.*, 10.1128/jb.177.15.4508-4513.1995.
72. Datsenko,K.A. and Wanner,B.L. (2000) One-step inactivation of chromosomal genes in Escherichia coli K-12 using PCR products. *Proc. Natl. Acad. Sci. U. S. A.*, 10.1073/pnas.120163297.
73. Kolmsee,T. and Hengge,R. (2011) Rare codons play a positive role in the expression of the stationary phase sigma factor RpoS (σS) in Escherichia coli. *RNA Biol.*, 10.4161/rna.8.5.16265.
74. Gibson,D.G., Young,L., Chuang,R.Y., Venter,J.C., Hutchison,C.A. and Smith,H.O. (2009) Enzymatic assembly of DNA molecules up to several hundred kilobases. *Nat. Methods*, **6**, 343–345.
75. Jiang,Y., Chen,B., Duan,C., Sun,B., Yang,J. and Yang,S. (2015) Multigene editing in the Escherichia coli genome via the CRISPR-Cas9 system. *Appl. Environ. Microbiol.*, 10.1128/AEM.04023-14.
76. Rashid,F.Z.M. (2021) Chapter 2: Hi-C in bacteria and archaea.
77. Hagege,H., Klous,P., Braem,C., Splinter,E., Dekker,J., Cathala,G., De Laat,W. and Forne,T. (2007) Quantitative analysis of chromosome conformation capture assays (3c-qpcr). *Nat. Protoc.*, 10.1038/nprot.2007.243.
78. Chaurasiya,K.R. and Dame,R.T. (2018) Single molecule FRET analysis of DNA binding proteins. In *Methods in Molecular Biology*.
79. Laurens,N., Driessen,R.P.C., Heller,I., Vorselen,D., Noom,M.C., Hol,F.J.H., White,M.F., Dame,R.T. and Wuite,G.J.L. (2012) Alba shapes the archaeal genome using a delicate balance of bridging and stiffening the DNA. *Nat. Commun.*, 10.1038/ncomms2330.
80. Crémazy,F.G., Rashid,F.Z.M., Haycocks,J.R., Lamberte,L.E., Grainger,D.C. and Dame,R.T. (2018) Determination of the 3D genome organization of bacteria using Hi-C. In *Methods in Molecular Biology*.
81. Cordonnier,C. and Bernardi,G. (1965) Localization of E. coli endonuclease I. *Biochem. Biophys. Res. Commun.*, 10.1016/0006-291X(65)90434-1.
82. Taylor,R.G., Walker,D.C. and Mclnnes,R.R. (1993) E.coli host strains significantly affect the quality of small scale plasmid DNA preparations used for sequencing. *Nucleic Acids Res.*, 10.1093/nar/21.7.1677.
83. Hanahan D. (1985) Techniques for transformation of Escherichia coli. *En DNA Cloning a Pract. Approach (ed. Glover, D.M.). Oxford. IRL Press.*

84. Lioy,V.S., Cournac,A., Marbouty,M., Duigou,S., Mozziconacci,J., Espéli,O., Boccard,F. and Koszul,R. (2018) Multiscale Structuring of the E. coli Chromosome by Nucleoid-Associated and Condensin Proteins. *Cell*, 10.1016/j.cell.2017.12.027.
85. Hsieh,T.H.S., Fudenberg,G., Goloborodko,A. and Rando,O.J. (2016) Micro-C XL: Assaying chromosome conformation from the nucleosome to the entire genome. *Nat. Methods*, **13**, 1009–1011.
86. Gavrilov,A.A., Gushchanskaya,E.S., Strelkova,O., Zhironkina,O., Kireev,I.I., Iarovaia,O. V. and Razin,S. V. (2013) Disclosure of a structural milieu for the proximity ligation reveals the elusive nature of an active chromatin hub. *Nucleic Acids Res.*, 10.1093/nar/gkt067.
87. Condensin- and Replication-Mediated Bacterial Chromosome Folding and Origin Condensation Revealed by Hi-C and Super-resolution Imaging. *Mol. Cell*.
88. Kiernan,J.A. (1981) Histological and histochemical methods: theory and practice Oxford, UK.
89. Jamur,M.C. and Oliver,C. (2010) Cell fixatives for immunostaining. *Methods Mol. Biol.*, 10.1007/978-1-59745-324-0_8.
90. Jamur,M.C. and Oliver,C. (2010) Permeabilization of cell membranes. *Methods Mol. Biol.*, 10.1007/978-1-59745-324-0_9.
91. Bustin,S.A., Benes,V., Garson,J.A., Hellemans,J., Huggett,J., Kubista,M., Mueller,R., Nolan,T., Pfaffl,M.W., Shipley,G.L., *et al.* (2009) The MIQE guidelines: Minimum information for publication of quantitative real-time PCR experiments. *Clin. Chem.*, 10.1373/clinchem.2008.112797.
92. Gomes,A.É.I., Stuchi,L.P., Siqueira,N.M.G., Henrique,J.B., Vicentini,R., Ribeiro,M.L., Darrieux,M. and Ferraz,L.F.C. (2018) Selection and validation of reference genes for gene expression studies in Klebsiella pneumoniae using Reverse Transcription Quantitative real-time PCR. *Sci. Rep.*, 10.1038/s41598-018-27420-2.
93. Savli,H., Karadenizli,A., Kolayli,F., Gundes,S., Ozbek,U. and Vahaboglu,H. (2003) Expression stability of six housekeeping genes: A proposal for resistance gene quantification studies of Pseudomonas aeruginosa by real-time quantitative RT-PCR. *J. Med. Microbiol.*, 10.1099/jmm.0.05132-0.
94. Bai,B., Ren,J., Bai,F. and Hao,L. (2020) Selection and validation of reference genes for gene expression studies in Pseudomonas brassicacearum GS20 using real-time quantitative reverse transcription PCR. *PLoS One*, 10.1371/journal.pone.0227927.
95. Galisa,P.S., da Silva,H.A.P., Macedo,A.V.M., Reis,V.M., Vidal,M.S., Baldani,J.I. and Simes-Araújo,J.L. (2012) Identification and validation of reference genes to study the gene expression in Gluconacetobacter diazotrophicus grown in different carbon sources using RT-qPCR. *J. Microbiol. Methods*, 10.1016/j.mimet.2012.07.005.
96. Zhou,K., Zhou,L., Lim,Q., Zou,R., Stephanopoulos,G. and Too,H.P. (2011) Novel reference genes for quantifying transcriptional responses of Escherichia coli to protein overexpression by quantitative PCR. *BMC Mol. Biol.*, 10.1186/1471-2199-12-18.
97. Peng,S., Stephan,R., Hummerjohann,J. and Tasara,T. (2014) Evaluation of three reference genes of Escherichia coli for mRNA expression level normalization in view of salt and organic acid stress exposure in food. *FEMS Microbiol. Lett.*, 10.1111/1574-6968.12447.
98. Peters,J.M., Mooney,R.A., Grass,J.A., Jessen,E.D., Tran,F. and Landick,R. (2012) Rho and NusG suppress pervasive antisense transcription in Escherichia coli. *Genes Dev.*, **26**, 2621–2633.
99. Myers,K.S., Yan,H., Ong,I.M., Chung,D., Liang,K., Tran,F., Keleş,S., Landick,R. and Kiley,P.J. (2013) Genome-scale Analysis of Escherichia coli FNR Reveals Complex Features of Transcription Factor Binding. *PLoS Genet.*, 10.1371/journal.pgen.1003565.
100. Shao,X., Zhang,W., Umar,M.I., Wong,H.Y., Seng,Z., Xie,Y., Zhang,Y., Yang,L., Kwok,C.K. and Deng,X. (2020) RNA G-quadruplex structures mediate gene regulation in bacteria. *MBio*, 10.1128/mBio.02926-19.
101. Huppert,J.L., Bugaut,A., Kumari,S. and Balasubramanian,S. (2008) G-quadruplexes: The beginning and end of UTRs. *Nucleic Acids Res.*, 10.1093/nar/gkn511.
102. Kahramanoglou,C., Seshasayee,A.S.N., Prieto,A.I., Ibberson,D., Schmidt,S., Zimmermann,J., Benes,V., Fraser,G.M. and Luscombe,N.M. (2011) Direct and indirect effects of H-NS and Fis on global gene expression control in Escherichia coli. *Nucleic Acids Res.*, 10.1093/nar/gkq934.
103. Tatusov,R.L., Mushegian,A.R., Bork,P., Brown,N.P., Hayes,W.S., Borodovsky,M., Rudd,K.E. and Koonin,E. V. (1996) Metabolism and evolution of Haemophilus influenzae deduced from a whole-genome comparison with Escherichia coli. *Curr. Biol.*, **6**, 279–291.

104. Tomii,K. and Kanehisa,M. (1998) A comparative analysis of ABC transporters in complete microbial genomes. *Genome Res.*, **8**, 1048–1059.
105. Higgins,C.F. (1992) ABC Transporters: From microorganisms to man. *Annu. Rev. Cell Biol.*, **8**, 67–113.
106. Tam,R. and Saier,M.H. (1993) Structural, functional, and evolutionary relationships among extracellular solute-binding receptors of bacteria. *Microbiol. Rev.*, **57**, 320–346.
107. Saurin,W. and Dassa,E. (1994) Sequence relationships between integral inner membrane proteins of binding protein-dependent transport systems: Evolution by recurrent gene duplications. *Protein Sci.*, **3**, 325–344.
108. Mellies,J., Brems,R. and Villarejo,M. (1994) The Escherichia coli proU promoter element and its contribution to osmotically signaled transcription activation. *J. Bacteriol.*, **176**, 3638–3645.
109. Wade,J.T. and Grainger,D.C. (2018) Waking the neighbours: disruption of H-NS repression by overlapping transcription. *Mol. Microbiol.*, 10.1111/mmi.13939.
110. Rangarajan,A.A. and Schnetz,K. (2018) Interference of transcription across H-NS binding sites and repression by H-NS. *Mol. Microbiol.*, 10.1111/mmi.13926.
111. Boudreau,B.A., Hron,D.R., Qin,L., Van Der Valk,R.A., Kotlajich,M. V., Dame,R.T. and Landick,R. (2018) StpA and Hha stimulate pausing by RNA polymerase by promoting DNA-DNA bridging of H-NS filaments. *Nucleic Acids Res.*, 10.1093/nar/gky265.
112. Adhya,S. and Gottesman,M. (1978) Control of transcription termination. *Annu. Rev. Biochem.*, **47**, 967–996.
113. Adhya,S., Gottesman,M. and De Crombrugghe,B. (1974) Termination and antitermination in transcription: control of gene expression. *Basic Life Sci.*, **3**, 213–221.
114. Robinett,C.C., Straight,A., Li,G., Willhelm,C., Sudlow,G., Murray,A. and Belmont,A.S. (1996) In vivo localization of DNA sequences and visualization of large-scale chromatin organization using lac operator/repressor recognition. *J. Cell Biol.*, 10.1083/jcb.135.6.1685.
115. Lau,I.F., Filipe,S.R., Søballe,B., Økstad,O.A., Barre,F.X. and Sherratt,D.J. (2003) Spatial and temporal organization of replicating Escherichia coli chromosomes. *Mol. Microbiol.*, **49**, 731–743.
116. van Berkum,N.L., Lieberman-Aiden,E., Williams,L., Imakaev,M., Gnirke,A., Mirny,L.A., Dekker,J. and Lander,E.S. (2010) Hi-C: a method to study the three-dimensional architecture of genomes. *J. Vis. Exp.*, 10.3791/1869.
117. Qin,L., Erkelens,A.M., Ben Bdira,F. and Dame,R.T. (2019) The architects of bacterial DNA bridges: A structurally and functionally conserved family of proteins. *Open Biol.*, 10.1098/rsob.190223.
118. Vlahoviček,K., Kaján,L. and Pongor,S. (2003) DNA analysis servers: Plot.it, bend.it, model.it and IS. *Nucleic Acids Res.*, 10.1093/nar/gkg559.
119. Goodsell,D.S. and Dickerson,R.E. (1994) Bending and curvature calculations in B-DNA. *Nucleic Acids Res.*, 10.1093/nar/22.24.5497.
120. Kornyshev,A.A. and Leikin,S. (2001) Sequence recognition in the pairing of DNA duplexes. *Phys. Rev. Lett.*, 10.1103/PhysRevLett.86.3666.
121. Zuccheri,G., Scipioni,A., Cavaliere,V., Gargiulo,G., De Santis,P. and Samori,B. (2001) Mapping the intrinsic curvature and flexibility along the DNA chain. *Proc. Natl. Acad. Sci. U. S. A.*, 10.1073/pnas.051631198.
122. Scipioni,A., Anselmi,C., Zuccheri,G., Samori,B. and De Santis,P. (2002) Sequence-dependent DNA curvature and flexibility from scanning force microscopy images. *Biophys. J.*, 10.1016/S0006-3495(02)75254-5.
123. Colangeli,R., Helb,D., Vilchèze,C., Hazbón,M.H., Lee,C.G., Safi,H., Sayers,B., Sardone,I., Jones,M.B., Fleischmann,R.D., *et al.* (2007) Transcriptional regulation of multi-drug tolerance and antibiotic-induced responses by the histone-like protein Lsr2 in M. tuberculosis. *PLoS Pathog.*, 10.1371/journal.ppat.0030087.
124. Castang,S., McManus,H.R., Turner,K.H. and Dove,S.L. (2008) H-NS family members function coordinately in an opportunistic pathogen. *Proc. Natl. Acad. Sci. U. S. A.*, 10.1073/pnas.0808215105.
125. Castang,S. and Dove,S.L. (2010) High-order oligomerization is required for the function of the H-NS family member MvaT in Pseudomonas aeruginosa. *Mol. Microbiol.*, 10.1111/j.1365-2958.2010.07378.x.
126. Gordon,B.R.G., Li,Y., Wang,L., Sintsova,A., Van Bakel,H., Tian,S., Navarre,W.W., Xia,B. and

Liu,J. (2010) Lsr2 is a nucleoid-associated protein that targets AT-rich sequences and virulence genes in Mycobacterium tuberculosis. *Proc. Natl. Acad. Sci. U. S. A.*, 10.1073/pnas.0913551107.

Supplementary information

Supplementary methods

Genomic DNA preparation

An isolated *Escherichia coli* colony was cultured to stationary phase in LB medium at 37ºC with shaking at 200 rpm. Cells in 1.5 mL of the culture were collected by centrifugation at 10000xg at room temperature and resuspended in 400 µL of TES buffer (50 mM Tris-HCl, 10 mM NaCl, 10 mM EDTA, pH 7.5). The cell suspension was incubated with 1.0% Sarkosyl, 100 µg/mL RNase A (Qiagen®), and 100 µg/mL Proteinase K (Qiagen®) at 65ºC until the solution cleared. 400 µL of 4M NH_4OAc was added to the lysate, and the solution was extracted twice with 25:24:1 Phenol:Chloroform:Isoamyl alcohol (Sigma-Aldrich®) and once with chloroform (Sigma-Aldrich®). Genomic DNA was precipitated with an equal volume of isopropanol (Sigma-Aldrich®) for 10 minutes at room temperature, and pelleted by centrifuged for 20 minutes at 25000xg at 4ºC. The pellet was dissolved in 400 µL of 0.1 M NaOAc, pH 6.0, and re-precipitated with 800 µL of cold 100% ethanol (Sigma-Aldrich®) for 15 minutes at room temperature. The precipitated DNA was collected by centrifugation at 25000xg for 15 minutes at 4ºC. The pellet was washed with cold 70% ethanol (Sigma-Aldrich®) and air dried. Genomic DNA was dissolved in 1X TE (Sigma-Aldrich®) (10 mM Tris, 0.1 mM EDTA, pH 8.0).

H-NS purification

Escherichia coli BL21 Δ*hns* pLysE pRD18 was cultured in LB medium (1.0% bactotryptone (BD), 0.5% yeast extract (Alfa Aesar), 170 mM NaCl, pH 7.5) at 37ºC to an OD_{600} of 0.4. Expression of H-NS from pRD18 was induced with a final concentration of 120 µg/mL IPTG for 3 hours. The cells were collected by centrifugation at 7000 xg for 15 minutes at 25ºC. Cell pellets were resuspended in 20 mL low-salt H-NS buffer (130 mM NaCl, 20 mM Tris, 10% glycerol, 8 mM β-mercaptoethanol, and 3 mM benzamidine, pH 7.2) containing 100 mM NH_4Cl with 1 µg/mL DNase, 100 µg/mL lysozyme, and 1 mM PMSF. The cells were lysed by sonication and the soluble fraction was loaded onto a P11 column. H-NS was eluted in low-salt H-NS buffer with NH_4Cl using a gradient of 100 mM to 1.0 M NH_4Cl in 100 mL at a rate of 1 mL/min. Fractions with high concentrations of H-NS were pooled and dialysed overnight at 4ºC into low-salt H-NS buffer. The dialysed sample was loaded onto a 1 mL HisTrap™ HP column (Amersham Biosciences) and eluted in H-NS buffer (20 mM Tris, 10% glycerol, 8 mM β-mercaptoethanol, and 3 mM benzamidine, pH 7.2) using a gradient of 130 mM to

1M NaCl in 20 mL at a rate of 1 mL/min. The fractions with high H-NS concentrations were pooled and dialysed at 4ºC overnight into low-salt H-NS buffer. The H-NS was loaded onto a 1 mL Resource-Q column and eluted into a highly concentrated and pure peak with a block elution in H-NS buffer from 200 mM to 500 mM NaCl. The purified H-NS was dialysed at 4ºC overnight into H-NS buffer with 300 mM KCl. H-NS was separated into 50.0 µL aliquots, flash-frozen in liquid nitrogen, and stored at -80ºC until use.

Electrophoretic mobility shift assay

Purified H-NS was serially diluted in low-salt binding buffer (130 mM NaCl, 20 mM Tris, 10% glycerol, 8 mM β-mercaptoethanol, and 3 mM benzamidine, pH 7.2). The dilutions were mixed with an equivalent volume of 400 nM DRE^{mut} or DRE^{wt} (Supplementary file 3.1) in nuclease-free water (Ambion) and incubated for 20 minutes at 25 ºC followed by 10 minutes at 4 ºC. The samples were resolved on a polyacrylamide gel (Mini-Protean® TGX™ precast gels, 4-15%, Bio-Rad) at 30 V at 4 ºC. Experiments were performed in triplicate. The polyacrylamide gels were stained for 45 minutes in a solution of 10X GelRed (Biotium) and thereafter imaged with GelDoc™ XR+ (Bio-Rad) using Bio-Rad's ImageLab software.

Supplementary figures

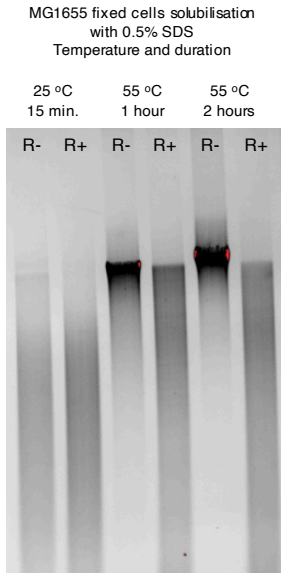

Figure S3.1: Cell solubilisation conditions that reliably decrease degradation of MG1655 chromatin in low [EDTA] buffers also promote de-crosslinking of formaldehyde-mediated crosslinks. Raising the temperature and increasing the duration of 0.5% SDS treatment during lysis and solubilisation of fixed cells increases the stability of the extracted chromatin in low [EDTA] buffer.

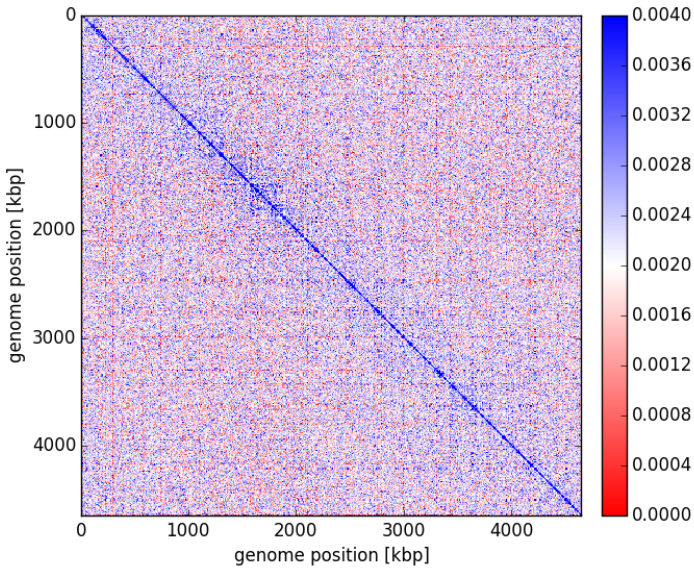

Figure S3.2: Fixation of *E. coli* cells with higher concentrations of formaldehyde does not significantly improve the signal-to-noise ratio in chromosome contact maps. Chromosome contact

maps generated from 3C-based libraries prepared with *E. coli* cells fixed using 7% formaldehyde do not show a significant improvement in the signal-to-noise ratio compared to maps generated from *E. coli* cells fixed with 3% formaldehyde (Figure 3.2A). **Organism:** *Escherichia coli* MG1655 Δ*endA* (NT331); **3C-based study:** 3C-Seq; **Growth conditions:** LB medium, 37 ºC, exponential phase; **Fixation conditions:** 7% formaldehyde, 1 hour; **Restriction enzyme:** HpaII (NEB); **Fractionation:** Not performed.

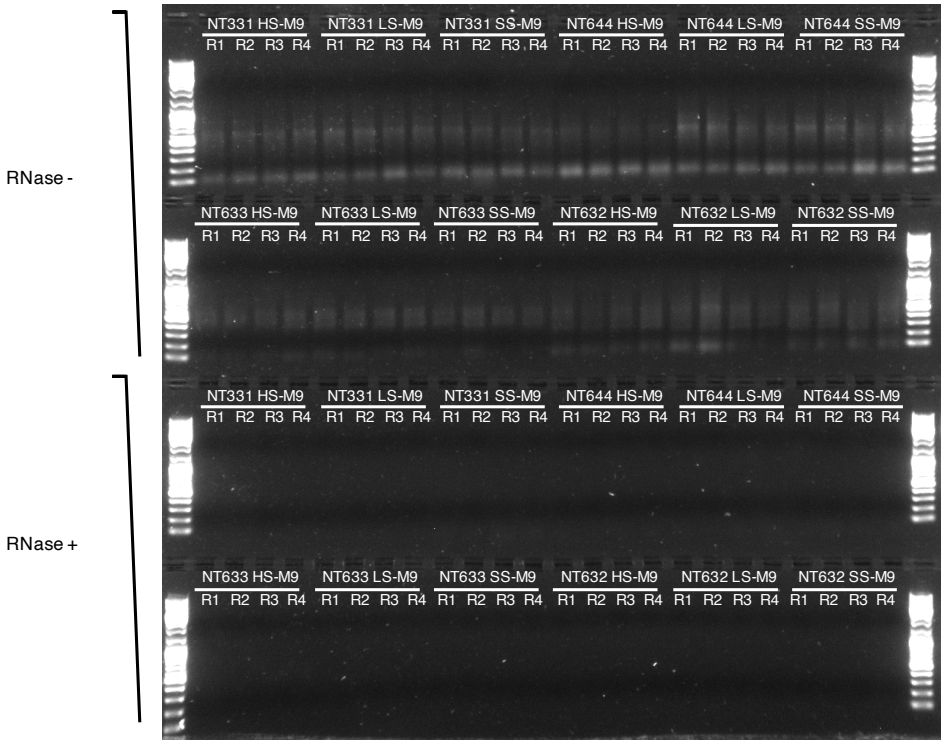

Figure S3.3: DNA contamination assessment of RNA preparations. ~100 ng of RNA with (RNase+) or without (RNase-) RNase treatment were visualised on a 1.2% agarose gel pre-stained with 1X GelRed (Sigma-Aldrich). The absence of a nucleic acid signal in the RNase+ wells indicates undetectable DNA contamination.

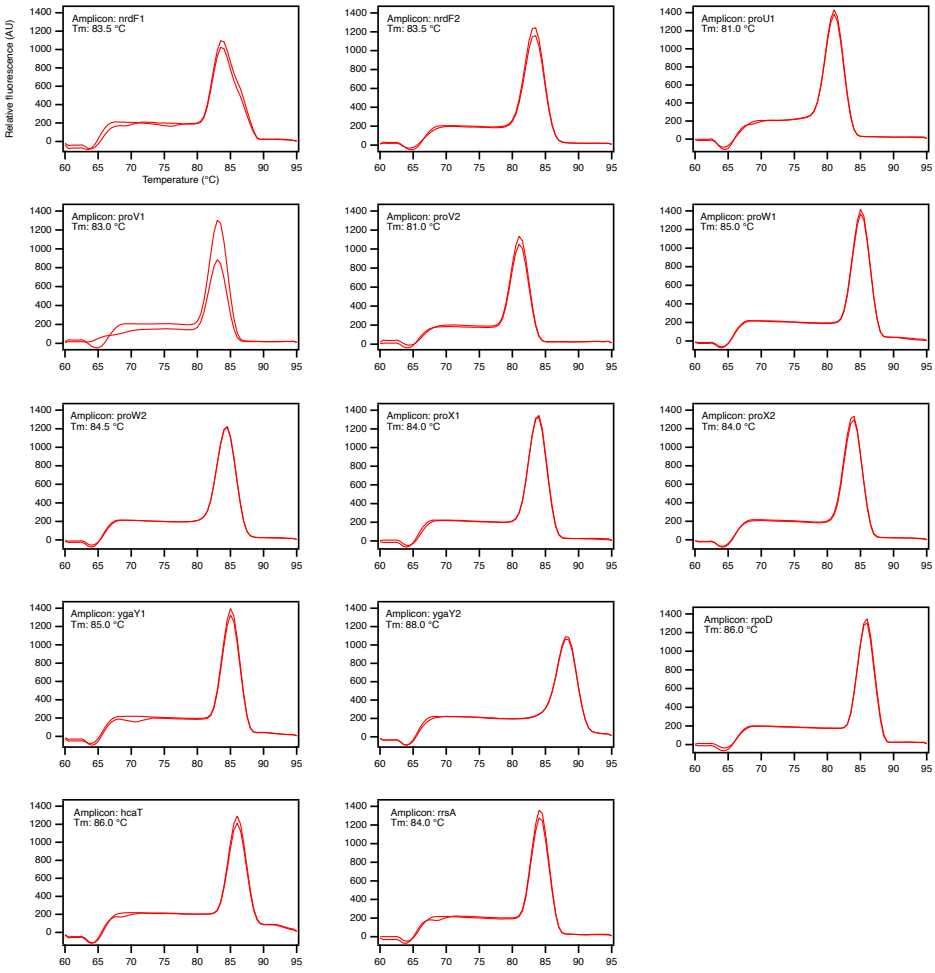

Figure S3.4: RT-qPCR amplicon melting curves. The specificity of amplification in RT-qPCR reactions was gauged from the melting curve of the fragment amplified in each well. The melting curve and the melting temperature (Tm) of the amplicons reported on in this chapter are shown here. The sequences of the fragments used for this experiment were verified with Sanger sequencing (Supplementary file 3.2).

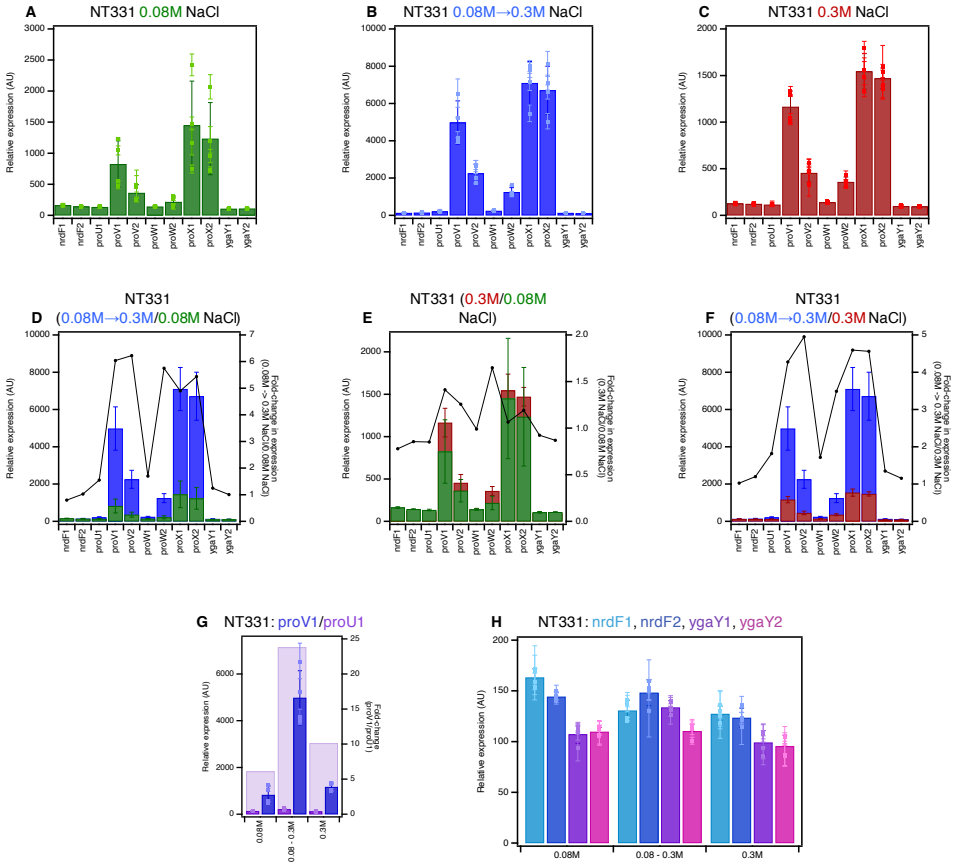

Figure S3.5: The transcriptional profile of *proVWX* and its flanking regions in NT331 during **(A)** exponential growth in M9 medium with 0.08 M NaCl, **(B)** hyperosmotic shock in M9 medium from 0.08 M to 0.3 M NaCl, and **(C)** exponential growth in M9 medium with 0.3 M NaCl. **The fold change in expression level of *proVWX* and its flanking regions** between **(D)** a hyperosmotic shock and exponential growth at 0.08 M NaCl, **(E)** exponential growth at 0.3 M NaCl and 0.08 M NaCl, and **(F)** a hyperosmotic shock and exponential growth at 0.3 M NaCl. **(G) The fold difference in expression at the *proV*1 amplicon compared to the *proU*1 amplicon** during exponential growth at 0.08 M NaCl, following a hyperosmotic shock, and during exponential growth at 0.3 M NaCl. **(H) The relative expression at amplicons flanking *proVWX*** during exponential growth at 0.08 M NaCl, following a hyperosmotic shock, and during exponential growth at 0.3 M NaCl. **Internal control: *hcaT***.

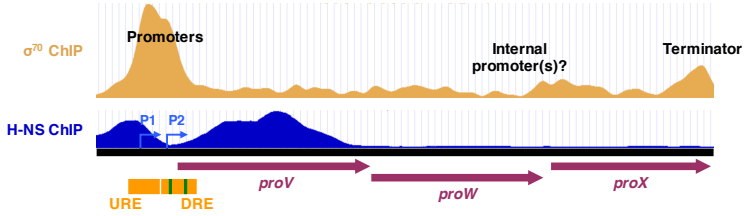

Figure S3.6: The chromatin immunoprecipitation (ChIP) profiles of RNA Polymerase σ^{70} (yellow) (99) **and H-NS (blue)** (102) **at *proVWX*.** The purple arrows represent the *proV*, *proW*, and *proX* ORFs. The orange bars mark the *proVWX* upstream and downstream regulatory elements (URE and DRE). The green bars within the DRE designate high-affinity H-NS binding sites. The P1 and P2 *proVWX* promoters and their transcriptional directionalities are shown with blue right-angle arrows.

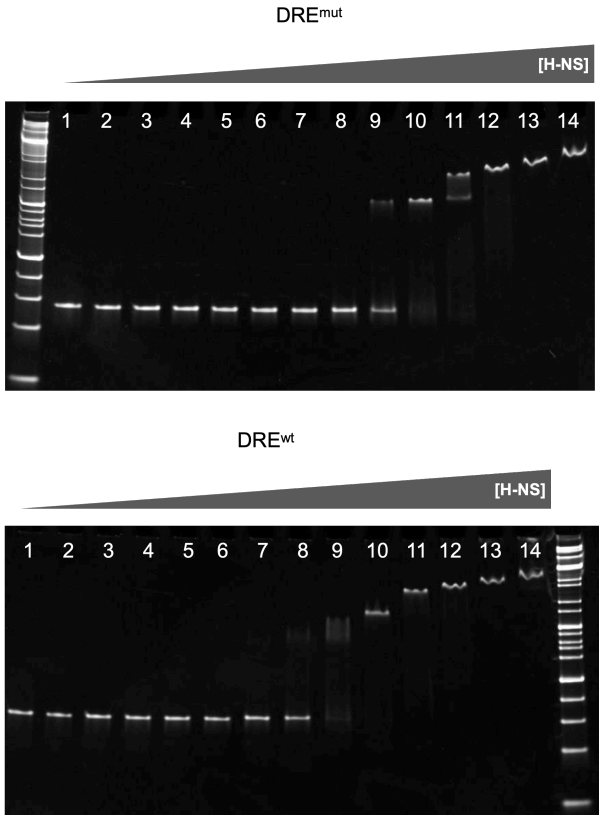

Lane	[H-NS] (nM)
1	31.7
2	52.8
3	88.0
4	146.6
5	244.4
6	407.3
7	678.8
8	1131
9	1885
10	3142
11	5238
12	8730
13	14550
14	24250

Figure S3.7: The mutated DRE (top) has a lower affinity for H-NS than the wild-type DRE (bottom)

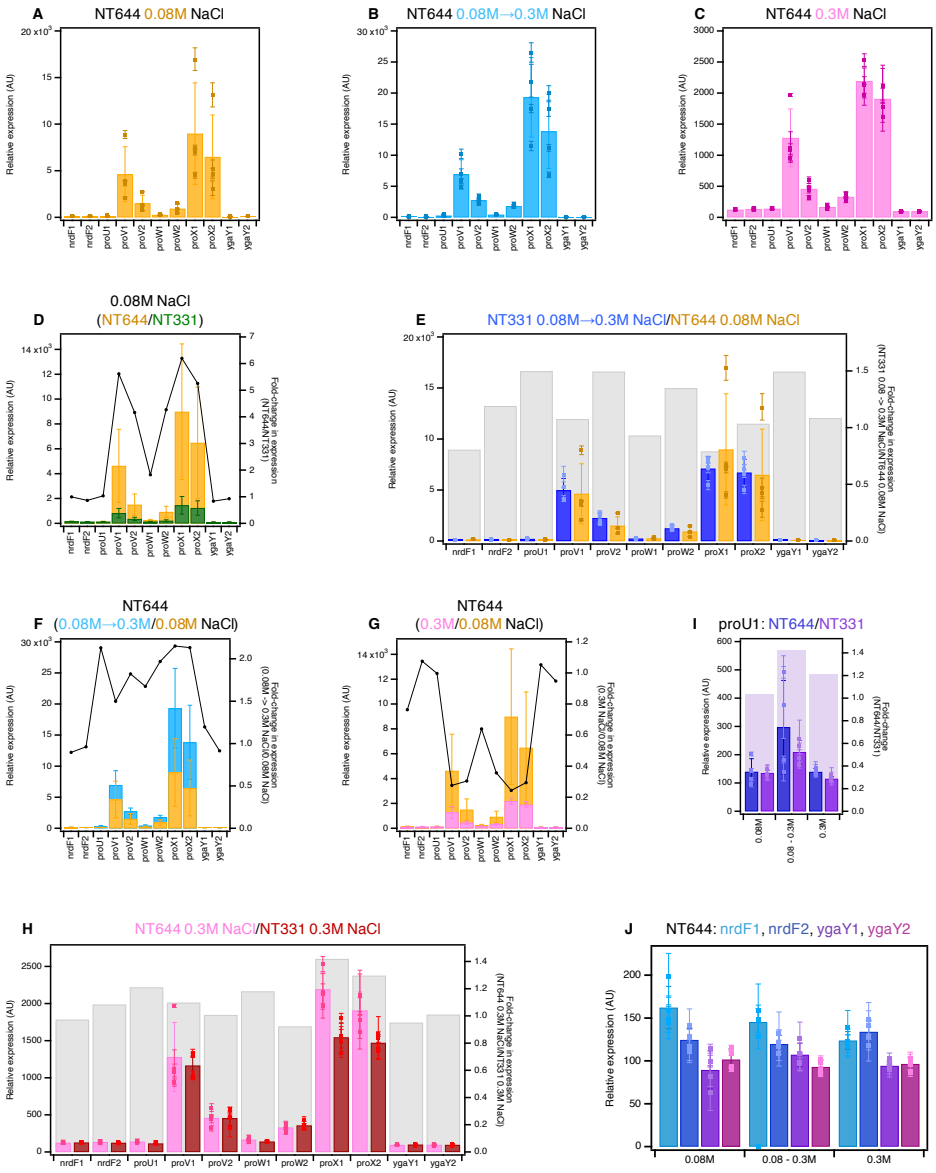

Figure S3.8: The transcriptional profile of *proVWX* and its flanking regions in NT644 during **(A)** exponential growth in M9 medium with 0.08 M NaCl, **(B)** hyperosmotic shock in M9 medium from 0.08 M to 0.3 M NaCl, and **(C)** exponential growth in M9 medium with 0.3 M NaCl. **The fold change in expression level of *proVWX* and its flanking regions** between **(D)** NT644 and NT331 during exponential growth at 0.08 M NaCl, **(E)** NT331 following a hyperosmotic shock and NT644 growing exponentially at 0.08 M NaCl, **(F)** a hyperosmotic shock and exponential growth at 0.08 M NaCl for NT644, **(G)** exponential growth at 0.3 M NaCl and 0.08 M NaCl for NT644, and **(H)** NT644 and NT331 growing exponentially at 0.3 M NaCl. **(I) The fold change in expression at the *proU*1 amplicon** between NT644 and NT331 during exponential growth at 0.08 M NaCl, following a hyperosmotic shock, and during exponential growth at 0.3 M NaCl. **(J) The relative expression level in NT644 at amplicons flanking *proVWX*** during exponential growth at 0.08 M NaCl, following a hyperosmotic shock, and during exponential growth at 0.3 M NaCl. **Internal control: *hcaT***

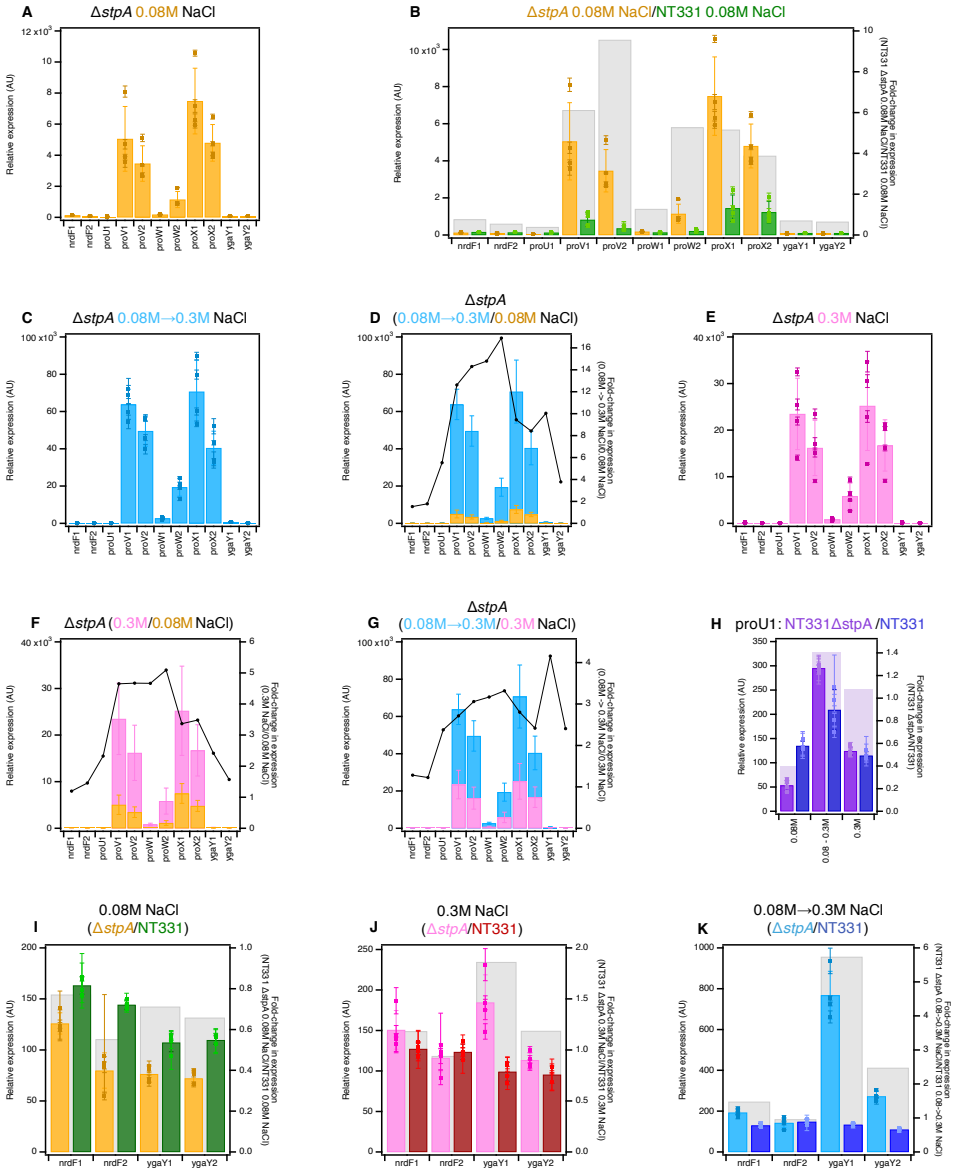

Figure S3.9: The transcriptional profile of the *proVWX* operon and its flanking regions in NT331 Δ*stpA* (A) during exponential growth at 0.08 M NaCl and **(B)** the fold-change in the expression levels of the amplicons compared to NT331, **(C)** upon a hyperosmotic shock from 0.08 M to 0.3 M NaCl, and **(D)** the fold-change in expression levels of the amplicons in comparison to exponential growth at 0.08 M NaCl, and **(E)** during exponential growth at 0.3 M NaCl, and the fold-change in expression levels of the amplicons with respect to **(F)** exponential growth at 0.08 M NaCl, and **(G)** a hyperosmotic shock. **(H) The fold-difference in expression level of amplicon *proU*1** between NT331 ΔstpA and NT331. **The fold-change in expression levels of the *nrdF* and *ygaY* amplicons between NT331 Δ*stpA* and NT331 (I)** during exponential growth at 0.08 M NaCl, **(J)** exponential growth at 0.3 M NaCl, and **(K)** following a hyper-osmotic shock. **Internal control: *hcaT***.

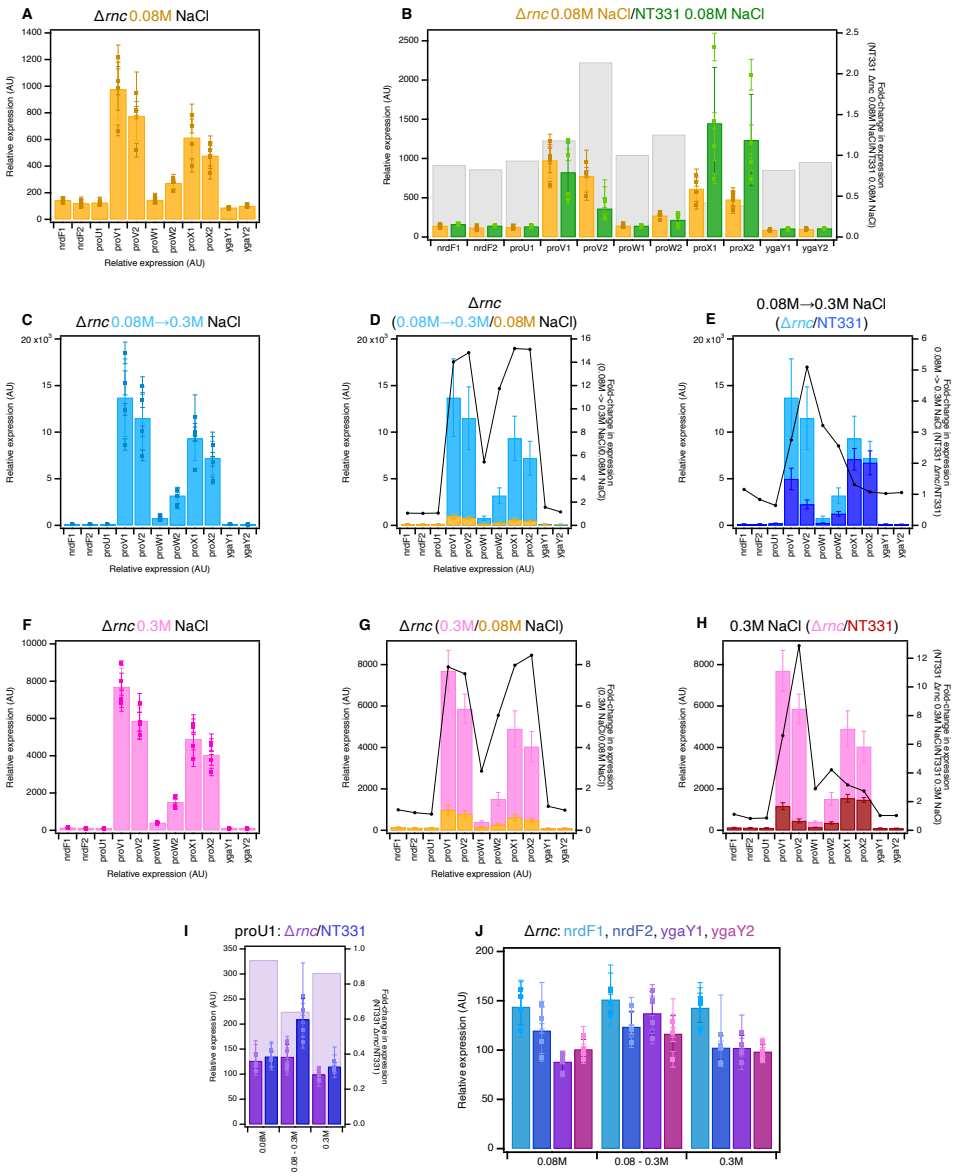

Figure S3.10: The transcriptional profile of *proVWX* and its flanking regions in NT331 Δ*rnc* during **(A)** exponential growth at 0.08 M NaCl, and **(B)** the fold-change in expression of the amplicons compared to NT331 growing exponentially at 0.08 M NaCl, upon **(C)** a hyperosmotic shock from 0.08 M NaCl to 0.3 M NaCl, and the fold-change in expression of the amplicons in comparison to **(D)** NT331 Δ*rnc* growing exponentially at 0.08 M NaCl, and **(E)** NT331 following a hyperosmotic shock. **The transcription profile of *proVWX* and its flanking regions in NT331 Δ*rnc*** during **(F)** exponential growth at 0.3 M NaCl, and the fold-change in expression of the amplicons relative to **(G)** NT331 Δ*rnc* growing exponentially at 0.08 M NaCl, and **(H)** NT331 growing exponentially at 0.3 M NaCl. **(I) The fold-difference in the relative expression of the *proU*1** amplicon between NT331 Δ*rnc* and NT331. **(J) The relative expression level in NT331 Δ*rnc* at amplicons flanking *proVWX*** during exponential

growth at 0.08 M NaCl, following a hyperosmotic shock, and during exponential growth at 0.3 M NaCl. **Internal control: *hcaT***.

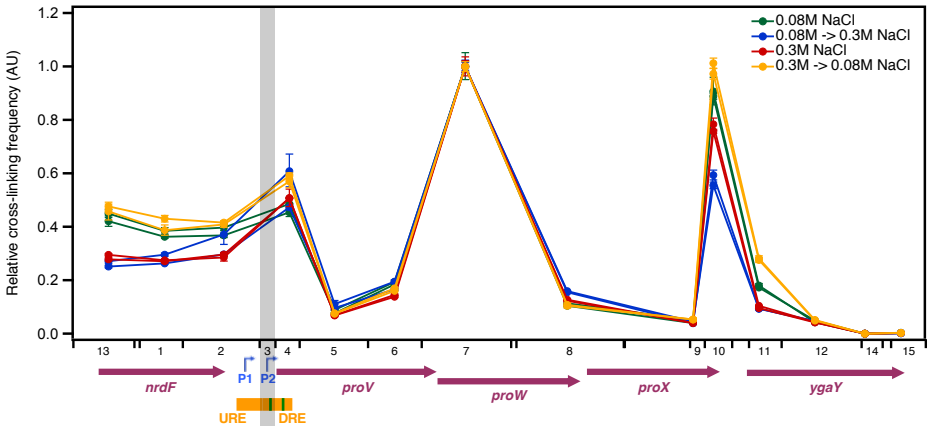

Figure S3.11: A 3C-qPCR study of the relative cross-linking frequency of proU3_NlaIII (highlighted in grey) with chromatin segments within and flanking *proVWX* (marked along the horizontal axis) during exponential growth in LB medium with 0.08 M NaCl (green), following a hyperosmotic shock from 0.08 M to 0.3 M NaCl (blue), during exponential growth at 0.3 M NaCl (red), and following a hypoosmotic shock from 0.3 M to 0.08 M NaCl (yellow). Each curve represents the 3C profile of an independent biological replicate. The error bars represent the standard deviation of three quantitation values from the qPCR run. *proV*, *proW*, *proX*, *nrdF*, and *ygaY* (purple arrows) show individual genes. P1 and P2 (right-angled blue arrows) mark proVWX promoters. The upstream and downstream regulatory elements of *proVWX* (URE and DRE) are shown with orange bars. The green bars in the DRE designate high-affinity H-NS binding sites. **Internal cross-linking control:** proU3_NlaIII-proU7_NlaIII.

Supplementary tables

Table S3.1: List of primers for smFRET studies.

Primer name	Sequence
HNS_bridge_fwd	BtnTEG-ATACATCCy3dTGTAACTTGAACGGCGTAAAAGAGG
HNS_bridge_rev	Cy5-TGAATTCTTCGATATGAGTCCTTAGTAACTTACCC
URE-DRE_rev	BtnTEG-TTTTTCy3dTCCAGACTGGCGTCTTTTACG
URE-DRE_fwd	Cy5-TAATTCCCGCCAAATAGCTT
DRE_fwd	BtnTEG-GCCATCAGGGGTTGCCTCAGATTCTCAGTATGTTAGGGTAGAAAAAAGCy3dTGACTATTTCC
ProW1_rev	Cy5-CTTTCGAAATGATGCCGACATACTGTTGGTCC
ProW2_rev	Cy5-AGTCGTCGGTGTACCCCAGGCGTCTGCGGATTG
ProW3_rev	Cy5-AGAATATTAAAATGCTCGACGTTTGGCGCAGGCGTA
ProW4_rev	Cy5-GATATAATCAACCGGAACGCGCACGCCCTGGAAGAC
ProW5_rev	Cy5-AAATCTGCCAGGCGATGAGAGCGAAAACGATAATCG
ProW6_rev	Cy5-CAGAGTCACCATTGCCTGCGACCAGGCACCGATTGC
ProUterm_rev	Cy5-GGGATGAAAGATAGATTGTTGAAATGTGCGATGTGG
IHF_60bp_fwd	Cy5-TTGGCATTATAAAAAAGCATTGCTTATCAATTTGTTGCAACGAACAGGTCACGTAATCGT
IHF_60bp_rev	Cy3-ACGATTACGTGACCTGTTCGTTGCAACAAATTGATAAGCAATGCTTTTTTATAATGCCAATTT-BtnTEG
IHF_35bp_A_fwd	Cy5-GATCTCAGGACGTAATACCAGTCCAGTACGACTTT
IHF_35bp_A_rev	Cy3-AAAGTCGTACTGGACTGGTATTACGTCCTGAGATCTTT-BtnTEG
IHF_35bp_B_fwd	Cy5-GGCCAAAAAAGCATTGCTTATCAATTTGTTGCACC
IHF_35bp_B_rev	Cy3-GGTGCAACAAATTGATAAGCAATGCTTTTTTGGCCTTT-BtnTEG
IHF_35bp_C_fwd	Cy5-TCAGGGGTTGCCTCAGATTCTCAGTATGTTAGGGT
IHF_35bp_C_rev	Cy3-ACCCTAACATACTGAGAATCTGAGGCAACCCCTGATTT-BtnTEG

Table S3.2: Relative expression values of amplicons within, and flanking the *proVWX* operon in NT331. Internal control: *rpoD*

Amplicon	NT331 0.08 M NaCl	NT331 Hyperosmotic shock	NT331 0.3 M NaCl
nrdF1	81.76±8.58	80.31±6.67	85.26±11.58
nrdF2	72.65±11.31	90.84±2.98	82.50±9.49
proU1	67.60±7.90	128.77±27.04	76.72±7.43
proV1	402.16±150.56	3047.84±637.44	773.91±89.45
proV2	177.21±50.60	1376.57±238.83	304.88±73.74
proW1	71.52±11.27	148.65±13.91	94.40±12.63
proW2	106.71±31.29	766.58±137.55	237.86±27.42
proX1	699.64±279.30	4365.00±726.11	1025.76±84.89
proX2	598.77±226.02	4125.85±795.50	979.43±65.30
ygaY1	53.92±8.70	82.41±8.39	65.80±4.53
ygaY2	54.98±5.93	67.00±7.56	63.53±6.03

Table S3.3: Relative expression values of amplicons within, and flanking the *proVWX* operon in NT331. Internal control: *hcaT*

Amplicon	NT331 0.08 M NaCl	NT331 Hyperosmotic shock	NT331 0.3 M NaCl
nrdF1	163.32±8.61	130.70±10.10	127.36±7.29
nrdF2	144.37±4.35	148.28±12.99	123.56±9.44
proU1	135.01±9.47	209.23±41.67	115.02±7.97
proV1	825.06±374.20	4982.62±1159.38	1165.23±168.78

proV2	362.27±132.65	2255.64±482.54	455.49±98.55
proW1	142.41±11.69	242.24±25.71	141.03±7.61
proW2	217.29±79.75	1250.22±241.01	358.28±53.15
proX1	1449.73±710.92	7101.04±1153.99	1545.50±192.71
proX2	1234.74±581.37	6713.35±1288.12	1471.58±109.99
ygaY1	107.28±9.05	133.79±6.59	99.17±11.73
ygaY2	109.74±4.21	110.35±6.71	95.51±10.66

Table S3.4: Relative expression values of amplicons within, and flanking the *proVWX* operon in NT644. Internal control: *rpoD*

Amplicon	NT644 0.08 M NaCl	NT644 Hyperosmotic shock	NT644 0.3 M NaCl
nrdF1	88.27±5.12	91.17±17.10	72.81±4.94
nrdF2	68.34±8.97	71.09±5.69	78.61±5.15
proU1	74.79±15.20	169.18±76.33	81.69±3.77
proV1	2428.61±1177.42	4032.33±868.78	734.54±175.17
proV2	796.10±341.97	1618.03±183.18	264.97±35.89
proW1	141.29±21.40	254.71±41.71	97.67±14.01
proW2	496.96±194.66	1081.64±127.27	193.62±19.97
proX1	4717.25±2145.92	11245.74±2835.34	1287.77±115.42
proX2	3378.13±1791.64	7965.02±2759.61	1128.00±210.66
ygaY1	48.54±9.77	63.73±8.35	55.60±5.71
ygaY2	55.56±4.41	55.20±3.46	56.70±3.78

Table S3.5: Relative expression values of amplicons within, and flanking the *proVWX* operon in NT644. Internal control: *hcaT*

Amplicon	NT644 0.08 M NaCl	NT644 Hyperosmotic shock	NT644 0.3 M NaCl
nrdF1	162.28±24.75	145.43±15.62	123.93±10.31
nrdF2	124.49±13.55	119.73±10.06	133.98±13.44
proU1	139.59±46.30	297.39±165.21	139.22±12.29
proV1	4632.45±2942.73	6948.43±2328.41	1279.27±465.74
proV2	1508.89±862.37	2748.93±522.37	458.92±116.22
proW1	260.22±58.78	436.10±120.87	166.54±27.97
proW2	927.22±448.16	1826.21±278.49	330.78±47.92
proX1	8984.84±5455.14	19333.58±6401.31	2193.00±238.20
proX2	6489.04±4488.92	13841.45±5963.81	1907.92±247.87
ygaY1	89.55±22.12	107.22±13.53	94.29±5.71
ygaY2	101.75±12.28	93.06±7.94	96.49±7.63

Table S3.6: Relative expression values of amplicons within, and flanking the *proVWX* operon in NT331 Δ*stpA* (NT633). Internal control: *rpoD*

Amplicon	NT633 0.08 M NaCl	NT633 Hyperosmotic shock	NT633 0.3 M NaCl
nrdF1	46.25±2.53	79.10±7.59	54.52±11.33
nrdF2	29.79±8.16	58.43±11.39	43.00±13.54
proU1	19.98±5.58	120.60±5.80	45.17±8.90
proV1	1808.97±533.26	26048.07±3254.38	8119.52±931.61
proV2	1248.25±267.61	20226.51±3164.81	5557.57±880.61
proW1	67.33±7.67	1100.01±205.74	296.37±28.02
proW2	410.52±136.89	7934.30±1992.17	1963.72±512.42
proX1	2708.60±468.16	28803.66±6405.98	8606.95±1628.96
proX2	1739.62±233.27	16464.36±3391.55	5773.60±938.28
ygaY1	28.40±5.41	313.55±46.54	65.85±7.87

ygaY2	26.85±5.16	111.52±9.33	41.30±8.68

Table S3.7: Relative expression values of amplicons within, and flanking the *proVWX* operon in NT331 Δ*stpA* (NT633). Internal control: *hcaT*

Amplicon	NT633 0.08 M NaCl	NT633 Hyperosmotic shock	NT633 0.3 M NaCl
nrdF1	125.97±10.43	193.56±14.99	150.77±23.88
nrdF2	79.80±17.35	142.70±24.42	116.26±17.29
proU1	53.39±10.33	295.26±6.41	124.22±8.26
proV1	5052.77±2083.77	63812.32±8172.40	23504.72±7658.21
proV2	3465.18±1140.43	49570.11±8135.08	16194.99±5930.20
proW1	182.25±3.84	2697.16±538.20	850.69±237.53
proW2	1147.82±517.95	19404.52±4834.93	5847.17±2784.05
proX1	7488.12±2115.74	70727.28±16904.09	25217.37±9585.28
proX2	4800.36±1181.15	40439.05±9029.73	16724.05±5495.00
ygaY1	76.42±7.41	768.07±117.33	184.66±34.12
ygaY2	72.25±6.94	273.21±23.27	113.45±9.30

Table S3.8: Relative expression values of amplicons within, and flanking the *proVWX* operon in NT331 Δ*rnc* (NT632). Internal control: *rpoD*

Amplicon	NT632 0.08 M NaCl	NT632 Hyperosmotic shock	NT632 0.3 M NaCl
nrdF1	83.09±6.94	90.11±13.79	82.23±7.34
nrdF2	69.94±18.13	73.93±16.09	59.03±7.40
proU1	73.48±12.17	80.54±21.69	57.72±10.85
proV1	559.26±96.36	8023.76±2095.41	4434.21±530.35
proV2	444.98±85.59	6715.55±1571.80	3394.43±544.03
proW1	83.09±14.12	453.45±83.01	239.58±53.78
proW2	157.33±19.22	1876.76±403.74	872.33±175.58
proX1	356.34±107.62	5511.92±1414.30	2818.13±460.38
proX2	277.14±63.50	4227.19±823.92	2319.72±359.24
ygaY1	51.17±6.31	80.78±7.12	59.70±13.03
ygaY2	58.37±4.84	68.84±9.64	57.59±11.98

Table S3.9: Relative expression values of amplicons within, and flanking the *proVWX* operon in NT331 Δ*rnc* (NT632). Internal control: *hcaT*

Amplicon	NT632 0.08 M NaCl	NT632 Hyperosmotic shock	NT632 0.3 M NaCl
nrdF1	143.94±18.40	151.32±12.66	142.88±14.94
nrdF2	119.79±24.13	123.63±15.83	102.38±12.24
proU1	126.33±15.92	134.26±24.93	99.27±9.15
proV1	975.93±228.81	13700.86±4167.98	7699.76±991.49
proV2	775.22±183.41	11494.71±3369.42	5862.75±710.33
proW1	143.06±22.42	779.19±221.60	409.41±48.64
proW2	272.42±40.24	3200.35±827.86	1512.10±312.42
proX1	614.23±166.78	9329.09±2384.86	4897.48±877.88
proX2	477.58±95.71	7217.89±1818.43	4037.97±734.01
ygaY1	88.16±8.82	137.41±22.07	102.15±12.71
ygaY2	100.83±10.11	116.59±18.27	98.49±7.54

Table S3.10: Relative cross-linking frequency of proU3_NlaIII with fragments within, and flanking the *proVWX* operon in NT331 during exponential growth at 0.08 M NaCl. Cross-linking control: proU3_NlaIII-proU7_NlaIII

	Replicate 1	Replicate 2

Cross-link fragment	Interaction frequency	Positive error	Negative error	Interaction frequency	Positive error	Negative error
proU13_NlaIII	0.47635	0.02006	0.01915	0.44966	0.01503	0.01455
proU1_NlaIII	0.43016	0.00613	0.00603	0.38473	0.01239	0.01200
proU2_NlaIII	0.41590	0.00820	0.00802	0.39729	0.01191	0.01156
proU4_NlaIII	0.59093	0.01647	0.01590	0.48582	0.00206	0.00206
proU5_NlaIII	0.07650	0.00201	0.00204	0.08878	0.00019	0.00018
proU6_NlaIII	0.16982	0.00540	0.00525	0.19367	0.00667	0.00645
proU7_NlaIII	1	0.05170	0.04916	1	0.02068	0.02026
proU8_NlaIII	0.10778	0.00391	0.00377	0.11385	0.00107	0.00106
proU9_NlaIII	0.05314	0.00072	0.00071	0.05070	0.00272	0.00258
proU10_NlaIII	1.01213	0.05303	0.05010	0.88884	0.01121	0.01107
proU11_NlaIII	0.28176	0.00764	0.00733	0.17288	0.00093	0.00092
proU12_NlaIII	0.05133	0.00222	0.00212	0.04904	0.00192	0.00185
proU14_NlaIII	0.00012	0.000005	0.000005	0.00012	0.000007	0.000007
proU15_NlaIII	0.00307	0.00013	0.00012	0.00243	0.00015	0.00014

Table S3.11: Relative cross-linking frequency of proU3_NlaIII with fragments within, and flanking the *proVWX* operon in NT331 following a hyperosmotic shock from 0.08 M to 0.3 M NaCl. Cross-linking control: proU3_NlaIII-proU7_NlaIII

Cross-link fragment	Replicate 1			Replicate 2		
	Interaction frequency	Positive error	Negative error	Interaction frequency	Positive error	Negative error
proU13_NlaIII	0.25154	0.00515	0.00505	0.27086	0.00779	0.00758
proU1_NlaIII	0.26281	0.00279	0.00276	0.29538	0.00621	0.00608
proU2_NlaIII	0.29662	0.00692	0.00676	0.37169	0.04124	0.03712
proU4_NlaIII	0.47300	0.00721	0.00710	0.60827	0.06438	0.05822
proU5_NlaIII	0.09636	0.00262	0.00255	0.11098	0.01334	0.01191
proU6_NlaIII	0.16592	0.00424	0.00413	0.19467	0.00717	0.00692
proU7_NlaIII	1	0.02407	0.02351	1	0.01493	0.01471
proU8_NlaIII	0.15494	0.00273	0.00268	0.15920	0.00116	0.00115
proU9_NlaIII	0.03905	0.00151	0.00145	0.04484	0.00167	0.00161
proU10_NlaIII	0.59386	0.01880	0.01823	0.55523	0.01225	0.01199
proU11_NlaIII	0.09405	0.00475	0.00452	0.09333	0.00179	0.00175
proU12_NlaIII	0.04729	0.00104	0.00102	0.04630	0.00504	0.00454
proU14_NlaIII	0.00008	0.000004	0.000004	0.00008	0.000006	0.000006
proU15_NlaIII	0.00200	0.00116	0.00073	0.00140	0.00016	0.00014

Table S3.12: Relative cross-linking frequency of proU3_NlaIII with fragments within, and flanking the *proVWX* operon in NT331 during exponential growth at 0.3 M NaCl. Cross-linking control: proU3_NlaIII-proU7_NlaIII

Cross-link fragment	Replicate 1			Replicate 2		
	Interaction frequency	Positive error	Negative error	Interaction frequency	Positive error	Negative error
proU13_NlaIII	0.29507	0.00471	0.004632	0.27786	0.00622	0.00609
proU1_NlaIII	0.27475	0.00504	0.00495	0.27088	0.00657	0.00642
proU2_NlaIII	0.28512	0.01430	0.01362	0.29622	0.00739	0.00721
proU4_NlaIII	0.50758	0.03359	0.03150	0.50704	0.00138	0.00137
proU5_NlaIII	0.06922	0.00202	0.00196	0.06809	0.00520	0.00483
proU6_NlaIII	0.14520	0.00312	0.00305	0.13839	0.00289	0.00283
proU7_NlaIII	1	0.03612	0.03486	1	0.02139	0.02095
proU8_NlaIII	0.12685	0.00294	0.00287	0.12323	0.00208	0.00205
proU9_NlaIII	0.04040	0.00152	0.00147	0.03948	0.00108	0.00105
proU10_NlaIII	0.78385	0.02326	0.02259	0.75720	0.00780	0.00772
proU11_NlaIII	0.10415	0.00185	0.00181	0.09542	0.00104	0.00103

proU12_NlaIII	0.04305	0.00094	0.00092	0.04197	0.00293	0.00274
proU14_NlaIII	0.00008	0.000006	0.000005	0.00007	0.000003	0.000003
proU15_NlaIII	0.00225	0.00033	0.00028	0.00217	0.00001	0.00001

Table S3.13: Relative cross-linking frequency of proU3_NlaIII with fragments within, and flanking the *proVWX* operon in NT331 following a hypoosmotic shock from 0.3 M to 0.08 M NaCl. Cross-linking control: proU3_NlaIII-proU7_NlaIII

Cross-link fragment	**Replicate 1**			**Replicate 2**		
	Interaction frequency	Positive error	Negative error	Interaction frequency	Positive error	Negative error
proU13_NlaIII	0.47635	0.00854	0.00839	0.45766	0.03432	0.03193
proU1_NlaIII	0.43016	0.01236	0.01202	0.38738	0.01975	0.01880
proU2_NlaIII	0.41590	0.00708	0.00697	0.40856	0.01089	0.01060
proU4_NlaIII	0.59094	0.01113	0.01093	0.57023	0.02499	0.02394
proU5_NlaIII	0.07650	0.00031	0.00030	0.07484	0.00075	0.00074
proU6_NlaIII	0.16982	0.00218	0.00215	0.16048	0.00292	0.00287
proU7_NlaIII	1	0.01818	0.01785	1	0.00620	0.00616
proU8_NlaIII	0.10779	0.00681	0.00641	0.10431	0.00942	0.00864
proU9_NlaIII	0.05315	0.00162	0.00157	0.05294	0.00619	0.00554
proU10_NlaIII	1.01214	0.01928	0.01892	0.97268	0.02005	0.01965
proU11_NlaIII	0.28176	0.00971	0.00938	0.27600	0.00942	0.00911
proU12_NlaIII	0.05133	0.00075	0.00074	0.04911	0.00134	0.00130
proU14_NlaIII	0.00012	0.00001	0.00001	0.00011	0.000003	0.000003
proU15_NlaIII	0.00307	0.00005	0.00005	0.00320	0.00008	0.00008